Neutralization Recognition and Structural Features of Reovirus Attachment Protein σ1

Dissertation

der Mathematisch-Naturwissenschaftlichen Fakultät

der Eberhard Karls Universität Tübingen

zur Erlangung des Grades eines

Doktors der Naturwissenschaften

(Dr. rer. nat.)

vorgelegt von

Dipl.-Chem. Melanie Dietrich

aus Tübingen

Tübingen

2016

Gedruckt mit Genehmigung der Mathematisch-Naturwissenschaftlichen Fakultät der Eberhard Karls Universität Tübingen.

Tag der mündlichen Qualifikation:	21.10.2016
Dekan:	Prof. Dr. Wolfgang Rosenstiel
1. Berichterstatter:	Prof. Dr. Thilo Stehle
2. Berichterstatter:	Prof. Terence S. Dermody, M.D.

Abstract

Virus attachment to the host cell surface and subsequent cell entry are key steps in viral infection. Neutralizing antibodies therefore often target virus proteins that mediate binding to cell receptors.

Mammalian orthoreoviruses (reoviruses) are useful models for studies of viral pathogenesis and host immunity, and they are promising oncolytic agents and vectors for vaccines. The reovirus attachment protein σ1 engages junctional adhesion molecule-A (JAM-A) and sialylated carbohydrate receptors. During the acid-dependent proteolysis from virions to infectious subvirion particles (ISVPs), which accompanies cell entry, the σ1 protein is thought to undergo a structural rearrangement.

In this thesis, the attachment protein σ1 of type 1 (T1) and type 3 (T3) reovirus were structurally analyzed in complex with antigen-binding fragments (Fabs) of the serotype-specific neutralizing antibodies 5C6 and 9BG5, respectively. The crystal structures allowed us to determine the complete antibody epitopes and to explain how reovirus variants can escape neutralization. Surface-plasmon resonance was used to investigate the interplay between JAM-A and antibody binding and to determine affinities of JAM-A and the Fabs for σ1. Together with the analysis of hemagglutination inhibition and cell-binding assays, we were able to propose a mechanism for how the antibodies neutralize reovirus infection. We observed strikingly different hemagglutination inhibition properties of 9BG5 for virions and ISVPs, a finding that provides additional evidence for a structural rearrangement of σ1 during virion-to-ISVP conversion.

In order to gain insights into the region of σ1 that anchors the protein into the virus capsid and to investigate the regions of predicted enhanced flexibility, crystal structures of the T1 and T3 σ1 tail domains were solved at high resolution. Both proteins possess a heptad repeat pattern of hydrophobic amino acids and form stable trimeric α-helical coiled coils. A discontinuity of the heptad repeat is conserved in the serotypes, and with our structural investigation we were able to define how the heptad repeat break is compensated by the proteins. The structural analysis of a T3 σ1 construct composed of the tail and the body domain revealed an unexpectedly seamless transition between the two domains. This finding is in contrast to the predicted higher flexibility of σ1 within this region and requires a reconsideration of the current model. Sequence analysis indicates that the observed interactions that stabilize the tail-body junction of T3 σ1 are conserved within the other serotypes. Our investigation of the tail and the tail-body junction of σ1

enabled us to formulate a full-length model of the elongated σ1 protein at high-resolution and provide a platform for future studies to define the flexibility of this protein.

Zusammenfassung

Die virale Zelladhesion, sowie der darauffolgende Eintritt in die Wirtszelle sind Schlüsselschritte einer Virusinfektion, weshalb daran beteiligte virale Proteine häufig Ziel neutralisierender Antikörper sind.

Humane Orthoreoviren (Reoviren) dienen als Modelsysteme zur Erforschung viraler Pathogenität, sowie der Wirts-Immunität und sind zudem vielversprechende onkolytische Agenzien und Vektoren für Impfstoffe. Das Reovirus-Adhesionsprotein σ1 bindet „junctional adhesion molecule-A“ (JAM-A), sowie sialinsäurehaltige Co-Rezeptoren. Während des Reovirus-Zelleintritts findet ein säureabhängiger, proteolytischer Abbau zu „infektiösen subviralen Partikeln“ (ISVPs) statt. Es wird angenommen, dass das σ1 Protein dabei eine Strukturänderung durchläuft.

Diese Arbeit befasst sich mit der strukturellen Analyse von Komplexen zwischen dem σ1 Protein von Serotyp 1 (T1) bzw. 3 (T3) mit antigen-bindenden Fragmenten (Fabs) der serotypspezifischen Antikörper 5C6 bzw. 9BG5. Durch die Strukturaufklärung konnten die Epitope bestimmt, und erklärt werden wie Reovirus-Varianten der Antikörperneutralisation entgehen können. Mittels Oberflächenplasmon-Resonanz Spektroskopie wurde das Bindevermögen von JAM-A gemeinsam mit den Antikörpern untersucht, sowie die Affinitäten von JAM-A und Fabs zu σ1 bestimmt. Zusammen mit der Analyse von Hämagglutinationshemmtests und Zelladhesionsuntersuchungen konnte ein Mechanismus der Antikörper vermittelten Infektionsneutralisierung aufgestellt werden. 9BG5 wies deutliche Unterschiede in der Hämagglutinationshemmung zwischen Viren und ISVPs auf, was ein weiteres Indiz für die Strukturänderung von σ1 während des Übergangs von Viren zu ISVPs darstellt.

Um Einblicke in die σ1-Region zu erhalten, welche das Protein im Viruskapsid verankert und um vorhergesagte Regionen mit erhöhter Flexibilität zu untersuchen, wurden Kristallstrukturen mit hoher Auflösung der filamentösen „tail“-Domäne von T1 σ1 und T3 σ1 gelöst. Beide Proteine enthalten ein Wiederholungsmuster von hydrophoben Aminosäuren und bilden stabile α-helikale Bündel. Eine Diskontinuität im Wiederholungsmuster ist bei allen Serotypen konserviert. Anhand der Strukturen konnte gezeigt werden wie das σ1 Protein diese kompensiert.

Die strukturelle Analyse eines T3 σ1 Konstrukts, welches die „tail“- sowie die „body“-Domäne beinhaltet, zeigt einen unerwartet nahtlosen Übergang der beiden Domänen, was im Gegensatz zur vorhergesagten, höheren Flexibilität dieser Proteinregion steht und eine Überdenkung des momentanen Models fordert. Sequenzanalysen deuten

darauf hin, dass die beobachteten Interaktionen, die den Übergang der „tail“ und der „body“-Domäne von T3 σ1 stabilisieren bei den anderen Serotypen ebenfalls konserviert sind. Die Untersuchung der „tail“ und der „tail-body“ Konstrukte bieten eine Plattform zukünftiger Studien zur Flexibilitätsuntersuchung des σ1 Proteins und ermöglichten das Erstellen eines Modells über die gesamte Proteinlänge.

Contributions of Others

Hemagglutination inhibition and cell-binding assays that are mentioned in the abstract and the discussion section have been performed and are marked as such by Kristen M. Ogden.

The surface plasmon resonance experiment that is shown in figure 4.25B was designed and performed together with Kerstin Reiss.

Table of Contents

Abbreviations

The commonly used abbreviations for chemical and physical units, amino acids and DNA bases are used.

AHTC	Anhydrotetracycline
Amp	Ampicillin
APS	Ammonium persulfate
CAPS	N-cyclohexyl-3-aminopropanesulfonic acid
cc	Coiled coil
CD	Circular dichroism
CDR	Complementarity determining region
DNA	Deoxyribonucleic acid
dNTP	2'-deoxynucleotide triphosphate
dsRNA	Double-stranded ribonucleic acid
DTT	Dithiothreitol
DLS	Dynamic light scattering
E. coli	*Escherichia coli*
EDC	1-ethyl-3-(3-dimethylaminopropyl) carbodiimide
EDTA	Ethylenediaminetetraacetic acid
EM	Electron microscopy
Fab	Fragment antigen binding
FRET	Fluorescence resonance energy transfer
GdmCl	Guanidine hydrochloride
HA	Hemagglutination
HEPES	4-(2-hydroxyethyl)-1-piperazineethanesulfonic acid
IgG	Immunoglobulin G
IgSF	Immunoglobulin superfamily
IPTG	Isopropyl β-D-1-thiogalactopyranoside
ISVP	Infectious subvirion particle
JAM-A	Junctional adhesion molecule-A
Kan	Kanamycin
LB	Lysogeny Broth
mAb	Monoclonal antibody
MALDI	Matrix-assisted laser desorption ionization
MES	2-(N-morpholino) ethanesulfonic acid
MOPS	3-(N-morpholino) propanesulfonic acid
MPD	2-methyl-2,4-pentanediol
mRNA	Messenger ribonucleic acid
NCS	Non-crystallographic symmetry
NgR1	Nogo receptor
NHS	N-hydroxysuccinimide
OD_{600}	Optical density at 600 nm
ORF	Open reading frame
P20	Polyoxyethylene sorbitan
PAGE	Polyacrylamide gel electrophoresis

PCR	Polymerase chain reaction
PDB	Protein data bank
PEG	Polyethylene glycol
PMSF	Phenylmethylsulphonyl fluoride
r.m.s.d.	Root mean square deviation
RU	Response unit
SAD	Single anomalous dispersion
SEC	Size exclusion chromatography
SDS	Sodium dodecyl sulphate
SLS	Swiss Light Source
SPR	Surface plasmon resonance
T1L	Type 1 Lang
T2J	Type 2 Jones
T3D	Type 3 Dearing
TAE	tris-acetate EDTA
TEMED	N,N,N’,N’-tetramethylethylenediamine
TMNO	Trimethylamine N-oxide
Tris	Tris(hydroxymethyl)aminomethane
UTR	Untranslated region
UV	Ultraviolet
v/v	Volume per volume
w/v	Weight per volume

1 Introduction

1.1 Reoviridae

The *Reoviridae* (respiratory enteric orphan viruses) form a family of non-enveloped, icosahedral viruses with a segmented double-stranded RNA (dsRNA) genome. Members of the group possess 9-12 dsRNA segments within a single or multi-layered capsid that measures 60-85 nm in diameter [1,2]. The family name refers to early virus isolates from healthy humans with no enteric and respiratory symptoms of disease [3].

Currently, 15 different genera are classified and subdivided into turreted and non-turreted *Reoviridae* viruses. Prominent representatives of the non-turreted subspecies are *Rotavirus* and *Orbivirus*. Rotaviruses cause severe gastroenteritis in infants and young children (< 5 years of age) and are a major cause of diarrhea-related hospitalization and child mortality in low-income countries [4,5]. Bluetongue virus and African horse sickness virus belong to the *Orbivirus* genus and are economically important pathogens of livestock [6].

Within the turreted subfamily, the *Orthoreovirus* genus includes viruses that infect mammals, birds and reptiles. Mammalian orthoreoviruses (herein referred to as reoviruses) are geographically widespread and infect virtually all mammals. Three major reovirus serotypes have been described, which can be differentiated through neutralization and hemagglutination inhibition tests [3,7]. Each serotype is represented by a prototype strain isolated from a human host: type 1 Lang (T1L), type 2 Jones (T2J), and type 3 Dearing (T3D).

Reovirus infection is mainly asymptotic in humans and can lead to mild respiratory and gastrointestinal disease symptoms in infants. In contrast, newborn mice are highly sensitive to reovirus infection, display serotype-specific disease patterns, and serve as model systems to study reovirus-host interactions and pathogenesis [8-10]. Reoviruses are prototypic members of the *Reoviridae* and, as they induce cell death and apoptosis preferentially in tumor cells, they are currently being tested as oncolytic agents in clinical trials [11].

1.1.1 Mammalian Orthoreovirus Structure and Components

Reoviruses encapsidate 10 dsRNA segments within a double-layered icosahedral protein shell. The ten genome segments are grouped and named according to their electrophoretic mobility into large (L1-L3), medium (M1-M3), and small (S1-S4)

segments. With exception of the bicistronic S1 gene, each gene segment is monocistronic and, thus, a total of eleven proteins (eight structural and three non-structural proteins) are encoded by the genome. The viral proteins are designated with the Greek letters λ, μ, and σ, in reference to their size class. The structural proteins are additionally numbered according to their relative electrophoretic mobility. As the size of the gene segments does not strictly correlate with the protein size there are some differences in the gene and protein nomenclature (Figure 1.1).

A

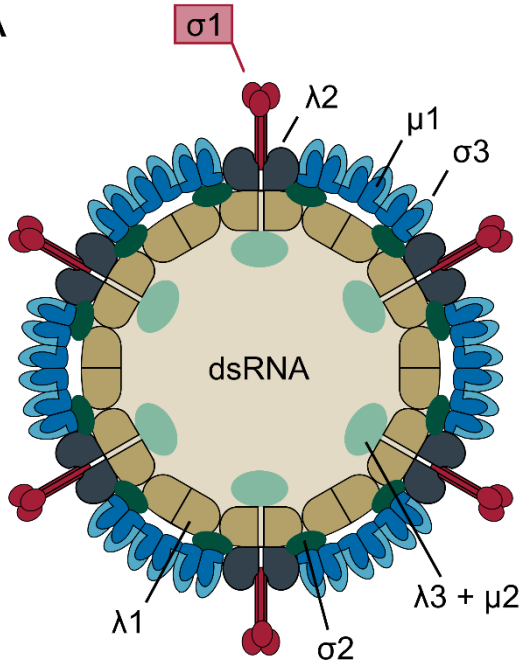

B

dsRNA segment	Encoded protein	Location (capsid)	Copy number
L1	λ3	Inner	12
L2	λ2	Inner	60
		Outer	
L3	λ1	Inner	120
M1	μ2	Inner	12-24
M2	μ1	Outer	600
M3	μNS	-	-
S1	σ1	Outer	36
	σ1s	-	-
S2	σ2	Inner	150
S3	σNS	-	-
S4	σ3	Outer	600

Figure 1.1 Reovirus capsid organization. (A) Schematic representation of the reovirus particle. The viral capsid proteins are labeled. **(B)** The genome segments and their corresponding protein products are listed. Eight structural and three non-structural proteins (μNS, σNS, and σ1s) are encoded by the reovirus genome. The protein components of the inner and outer capsid with the copy number per particle are indicated. Adapted from ViralZone (www.expasy.org/viralzone, Swiss Institute of Bioinformatics).

The inner core of the virus capsid exhibits icosahedral T=1 symmetry formed by 60 dimers of λ1. The intersubunit contacts of λ1, reveal a high degree of non-equivalency [12]. Four additional viral proteins (σ2, λ2, λ3, and μ2) also contribute to core formation. The 150 σ2 monomers bridge the λ1 subunits and stabilize the core from the outside. At each five-fold axis, a pentameric λ2 protein, which is the RNA-capping enzyme, forms a large turret that also protrudes from the outer capsid. The monomeric RNA-dependent RNA polymerase λ3 is located at the inner surface of each five-fold vertex and faces a small channel leading through the λ1 shell [13]. Approximately 12-24 copies of μ2, which

has an influence on the transcriptase and nucleoside triphosphatase activity of the core, are present [14].

The outer capsid is arranged with icosahedral quasi T=13 (*laevo)* symmetry and is primarily composed of 200 heterohexamers of μ1 and σ3. The μ1 protein is the membrane-penetration molecule and is protected from the environment by σ3, which forms finger-like projections on the virus surface. Most of the μ1 protein is autocatalytically cleaved and present as two fragments, μ1N and μ1C. At each five-fold axis, the trimeric reovirus attachment protein σ1 anchors into a λ2 pentamer. The σ1 protein is a filamentous molecule that uses proteinaceous and carbohydrate receptors to engage host cell surfaces [15-18]. σ1 of all reovirus serotypes binds to junctional adhesion molecule A (JAM-A), an integral component of intercellular tight junctions. σ1 also binds cell-surface carbohydrates, but the serotypes differ in the location of the binding site and carbohydrate specificity [17,19].

1.1.2 Entry Pathway and Replication Cycle

Reovirus attachment to target cells is thought to occur via a two-step adhesion strengthening mechanism. Low-affinity binding to carbohydrate receptors enables the virus to diffuse laterally on the cell surface and allows access and high-affinity binding to JAM-A [20].

Reovirus is internalized via receptor-mediated endocytosis, which involves β1-integrin binding probably to integrin-recognition sequences (RGD or KGE) in the λ2 protein [21,22]. The endocytic vesicles are then transported along microtubules and accumulate in late endosomes, where the viral outer-capsid undergoes stepwise, acid-dependent proteolysis (Figure 1.2) [23-25]. Reovirus uncoating is catalyzed by cathepsin proteases B, L, and S and leads to an initial disassembly intermediate termed infectious subvirion particle (ISVP) [26,27]. ISVPs are characterized by the removal of σ3, cleavage of μ1C into particle-associated fragments δ and φ, and a conformational change in the σ1 protein, from a compact to an elongated structure [28,29]. ISVPs also can be generated by proteases (chymotrypsin and trypsin) in the intestinal lumen after peroral inoculation, and they can be internalized either by endocytosis or by direct penetration of the plasma membrane [30-35].

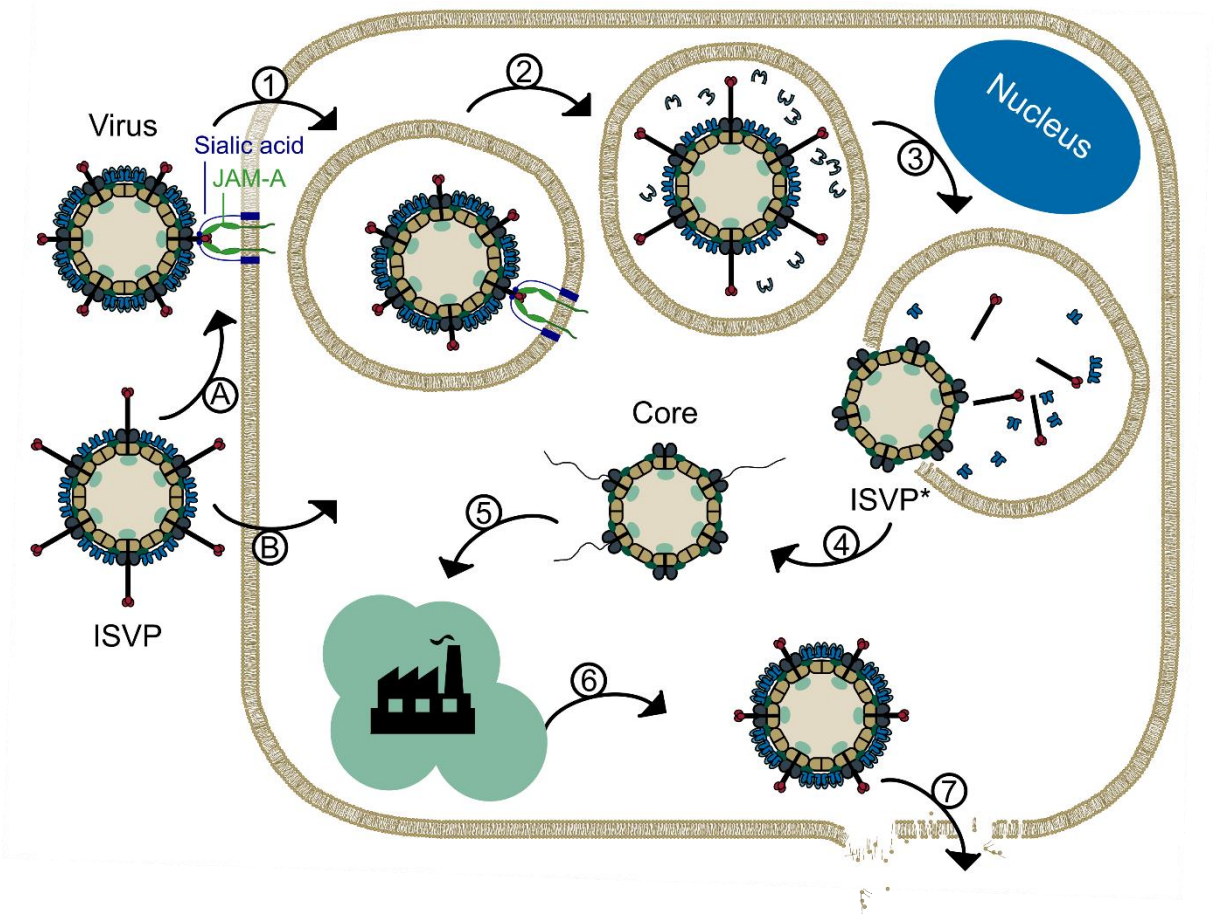

Figure 1.2 Reovirus cell entry and replication cycle. Reovirus engages carbohydrate receptors and junctional adhesion molecule A (JAM-A) using an adhesion strengthening mechanism. The virions enter the cell by receptor-mediated endocytosis **(1)**. Within late endosomes the virions are first converted to infectious subvirial particles (ISVP) **(2)**. ISVPs can also be generated by proteases in the intestinal lumen and internalize either by endocytosis **(A)** or by direct penetration of the cell membrane **(B)**. ISVPs in the endosomal compartment are processed into ISVP*s by rearranging µ1 fragments to expose hydrophobic residues and by the release of σ1 and µ1N **(3)**. The µ1 fragments mediate penetration of the endosomal membrane that leads to the release of transcriptionally active core particles into the cytoplasm **(4)**. Viral mRNA is synthesized, exported into the cytoplasm and translated by ribosomes into viral proteins. Large inclusions (viral factories) develop, where progeny reoviruses assemble **(5)**. Mature virions are formed **(6)** and released upon cell lysis **(7)**.

Endosomal ISVPs are further processed into ISVP*s, the second disassembly intermediate. In ISVP*s, the µ1-fragments undergo conformational rearrangements exposing hydrophobic residues, and µ1N and the σ1 protein are released from the particle [36,37]. Penetration of the endosomal membrane is mediated by the µ1 cleavage fragments. This leads to the release of transcriptionally active core particles into the cytoplasm (Figure 1.2) [38].

The core uses ribonucleoside triphosphates and S-adenosyl-L-methionine from the host cell to transcribe mRNAs from the (-)RNA of the reovirus genome segments. The newly synthesized (+)RNAs lack 3’ polyadenylation, are 5’ capped, and are delivered into the

cytoplasm through the central cavity of the λ2 turrets. These viral RNAs are translated by ribosomes, and upon encapsidation into core particles they also serve as templates for the synthesis of new dsRNA [39].

Reovirus replication and assembly takes place in cytoplasmic viral inclusions. Their formation is mainly regulated by the nonstructural proteins μNS and σNS and the structural protein μ2. In these inclusions, viral proteins, RNA, nascent and complete particles, and components of the cell cytoskeleton are concentrated [2]. Mature reovirus virions are formed by the assembly of the outer capsid around the nascent core particles and are released, presumably following reovirus-induced cell death and disruption of the host cell membrane [40,41].

1.1.3 Reoviruses as Cancer Therapeutics

Reoviruses are promising anti-cancer agents as they preferentially target and replicate within tumor cells and cause oncolysis. Their effect on certain transformed cell lines was first described in 1977 [42,43]. Currently, there are more than 30 completed and ongoing clinical trials (including phase I-III studies) focusing on reovirus T3D (Reolysin®, Oncolytics Biotech) as a cancer therapeutic.

Reovirus is well tolerated with low virulence and shows significant anti-cancer efficacy for many human tumor types in patients. Reovirus takes advantage of abnormal Ras activation in cancer cells, but the role of the Ras pathway for reovirus selective oncolysis is poorly understood and requires further investigation [44-46]. Other factors, such as the over-expression of reovirus carbohydrate receptors on cancer cells, also may contribute to enhanced reovirus infection [47,48]. Reovirus can presumably induce tumor cell death through multiple mechanisms, including apoptosis, autophagy, and necrosis [49-51].

To improve reovirus potency as an anticancer therapeutic, a better understanding of the mechanisms underlying its oncolytic activity is crucial. Further attempts seek to manipulate host immune responses to selectively reduce reovirus immune-clearance and to enhance viral anti-tumor immunity. The efficacy of reovirus oncolysis may also be improved by the development of new vectors using the reovirus reverse genetic system [52].

1.2 Reovirus Attachment Protein σ1

The three reovirus serotypes differ in neutralization and hemagglutination properties and invade the central nervous system of newborn mice by different routes and cause

serotype-specific patterns of disease. From the murine intestine, T1L spreads hematogenously, infects ependymal cells, and causes non-lethal hydrocephalus. In contrast, T3D spreads via hematogenous and neural routes, infects neurons, and causes lethal encephalitis [8,9,53,54]. Oral inoculation of T2J leads to nonlethal encephalitis, but as T2J is difficult to cultivate, the pathogenesis of this reovirus strain is poorly understood [55,56]. Studies using reassortant reoviruses indicate that the serotype-dependent differences are linked to the S1 gene segment [57,58].

The S1 gene possess two open reading frames; the first encodes the attachment protein σ1, and the second the small nonstructural protein σ1s. In comparison to the other gene segments, which are highly similar among the reovirus serotypes, the S1 genes are more divergent [59].

The σ1 proteins of T1L and T2J are more closely related to each other (with 49% sequence identity) than to T3D σ1 (26% and 27% identity, respectively) [60]. Just about 10% of the amino acids are conserved in the σ1 proteins of all three serotypes. Therefore, it is not surprising that the outer-capsid protein σ1 is a major determinant of serotype-specific differences in spread and tropism, and it is also a main target of the serotype-specific neutralizing antibody response.

1.2.1 Domain Organization and Structure

The trimeric attachment protein σ1 is a filamentous molecule of about 480 Å in length [29,61]. Amino acid sequence analyses predicted that σ1 consists of distinct domains, termed tail, body, and head, an organization that is conserved between the different serotypes (Figure 1.3) [60].

EM reconstructions of reovirus virions and ISVPs indicate that σ1 assumes a more compact conformation on virions, while it extends as an elongated structure from ISVPs. This observation suggests that σ1 undergoes an extensive structural rearrangement during virion-to-ISVP conversion [28,29]. EM images of σ1 isolated from virions show higher flexibility at a region near the N-terminus, at the midpoint of the molecule coinciding with the junction of the tail and body domains, and a region near the head domain [61]. The length and flexibility of the σ1 protein are important for its function [62].

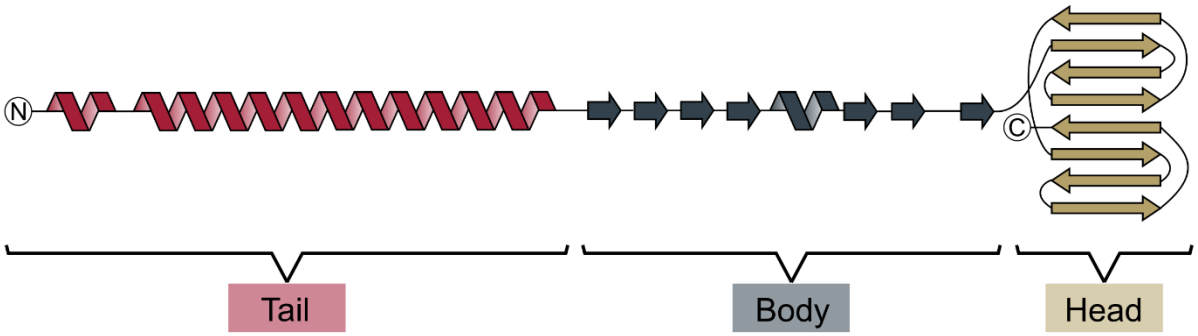

Figure 1.3 Conserved domain organization of the σ1 protein. Model of the secondary structure. Three structurally and functionally distinct domains of σ1 termed tail, body, and head are indicated. The first 20-25 residues of the N-terminus anchors the protein into the virus particle and harbors a short heptad repeat pattern of hydrophobic amino acids that predict an α-helical coiled coil. The small coiled coil is separated by a few residues from a predicted longer coiled coil that comprises most of the remaining tail. Structural information is available for the body and the head domain [17,19,63]. The body domain consists mostly of β-spiral repeats, interrupted by a small coiled coil segment. The C-terminal part of the molecule forms a globular head domain.

Tail Domain

The first 20-25 N-terminal amino acids of σ1 anchors the protein into the pentameric turrets of λ2 at the icosahedral vertices. The three-fold symmetry of σ1 does not match the five-fold symmetry of λ2. Such symmetry mismatches are rare and are found at the head-tail junctions of bacteriophages, in polyomavirus VP1/VP2 interactions and adenovirus fiber-penton complexes [64-66]. Symmetry mismatches are linked to interactions of limited strength or specificity [67]. Furthermore, proteins involved in symmetry mismatches often undergo structural changes. The possible weak connection between σ1 and λ2 might play a role during reovirus disassembly. σ1 is assumed to rearrange its structure during virion-to-ISVP conversion, and it is released from the particle during transition from ISVPs to cores. This later step also involves a structural rearrangement in λ2 and enables nascent mRNA to exit the particle at the five-fold symmetry axis, where σ1 was anchored [28].

A small region of the N-terminus and most of the remaining tail domain of σ1 exhibit a heptad repeat pattern of hydrophobic amino acids that predict the formation of an α-helical coiled coil [60,61]. Usually, this structural motif $(abcdefg)_n$ possesses hydrophobic amino acids at positions *a* and *d*, whereas the other positions are occupied by more polar residues (Figure 1.4). Within a helical bundle a hydrophobic core is formed. The core-flanking residues (*g* and *e*) often carry charged amino acids that contribute to the stability of the structure via interhelical salt bridges [68].

Coiled coils are very common structural motifs and usually consist of two, three, or four helices. The oligomeric state of coiled coils is determined by core packing interactions, as in different multimers the geometry of side chains at positions *a* and *d* systematically differs. Two-stranded coiled coils prefer β-branched residues (e.g., Ile, Val) at position *a* and unbranched or γ-branched ones (e.g., Leu) at position *d*. The reverse case is favored by four-stranded helical bundles. Trimeric coiled coils have a more uniform side chain geometry at these positions [68].

Protein sequences that follow the heptad repeat pattern wind into left-handed helical bundles. Due to this supercoiling, the number of residues per turns is reduced to 3.5 in comparison to undistorted α-helices. This allows the realization of periodically equivalent positions along the bundle. Discontinuities in the heptad repeat pattern, such as insertions of one (skip), three (stammer), or four (stutter) amino acids, are frequently encountered in coiled coil structures. Such discontinuities can be tolerated within a continuous coiled coil but account for a local distortion of the geometry [69].

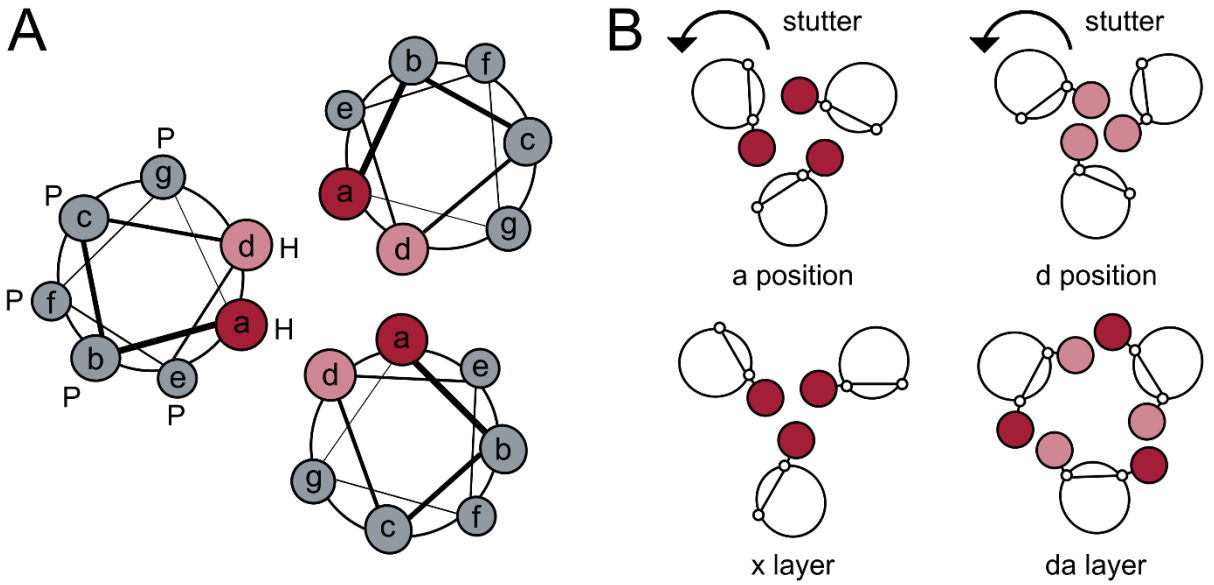

Figure 1.4 Helical wheel representation of a three-stranded α-helical coiled coil. (A) The heptad repeat pattern $(abcdefg)_n$ harbors hydrophobic amino acids (*H*) at positions *a* and *d* that point towards the inside of the helical bundle. The remaining positions are usually occupied by polar residues (*P*). The *e* and *g* positions often carry charged amino acids that can form electrostatic interactions with the adjacent α-helices. **(B)** A stutter is a four-residue insertion in the heptad repeat, a discontinuity that leads to a local distortion of the coiled coil geometry. The insertion raises the local sequence periodicity and causes an unwinding of the coiled coil that alters the relative position of the residues. This is schematically shown as a rotation of the helices. Typical *a* and *d* positions of undistorted coiled coils are shown in the upper row. Stutters shift position *a* residues (dark red) toward the core center leading to a so-called *x* layer. Position *d* residues (light red) are shifted out of the core and the following residues move towards position *a,* leading to a *da* layer. Depending on whether the insertion

occurs close to a core position or between the core positions, one or two consecutive layers are distorted. Adapted from [68].

In the repeating pattern of the σ1 tail two discontinuities are predicted; a stutter and a skip [60]. Following the stutter, the location of which is conserved in all three serotypes, T1L has a 14-residue and T2J a 7-residue insertion relative to T3D σ1. Therefore, it is assumed that the long α-helical coiled coil of T1L σ1 consists of 22.5, T2J σ1 of 21.5, and T3D σ1 of 21 heptads. In all cases, the skip is predicted at the C-terminal end of the coiled coil at the boundary between the tail and body domains [60].

Body Domain

The body domain consists mostly of triple β-spiral repeats, a fold thus far observed only in a small number of viral fiber proteins, including the adenovirus fiber, the avian reovirus sigma C protein, and the bacteriophage PRD1 [70-72]. The β-spiral repeat motif is characterized by a consensus sequence (a-o) with conserved apolar residues (at positions c, e, g, k, m) and either a proline or glycine at position j. Each repeat is composed of two short anti-parallel β-strands, which are connected by a four-residue β-turn with a proline or glycine at the third position. The following repeat is connected with a surface-exposed loop.

For T3D σ1, structural information for the complete body and head domain is available [19]. The T3D σ1 body consists of seven triple β-spiral repeats (β1-β7) and a short α-helical coiled coil segment that is incorporated between β-spiral repeats β4 and β5 (Figure 1.5). T3D σ1 is sensitive to protease cleavage within the body domain. Trypsin cleaves after R245, while chymotrypsin cleaves after L261 and F239 [73]. T3 field isolates that exhibit a single polymorphism, T249I, which is located at a *d* position of the short coiled coil of the body domain, are resistant to trypsin cleavage [74]. This indicates that an intact heptad repeat is required to resist cleavage at a nearby site. The glycan-binding site of T3D σ1 is also located in the body domain, between β-spiral repeats β2 and β3 [19].

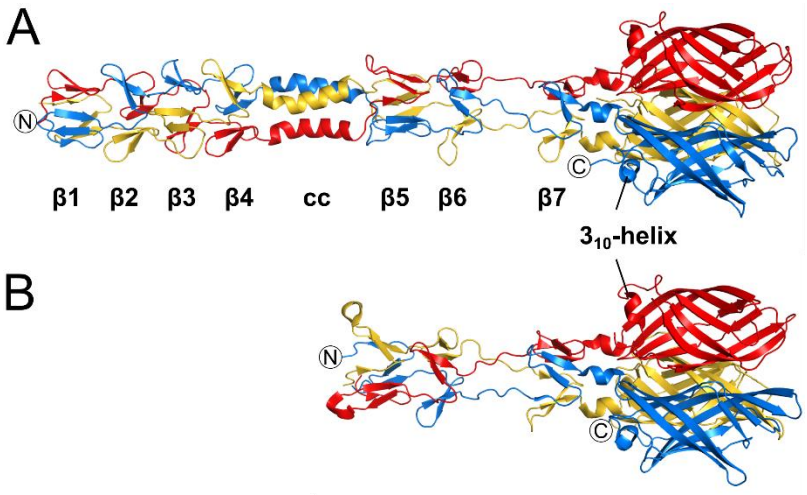

Figure 1.5 Crystal structures of T1L σ1 and T3D σ1. (A, B) Ribbon drawing of crystal structures that provide the most complete picture of T1L σ1 and T3D σ1 available up to date. The trimeric molecules are colored in blue, red and yellow. **(A)** T3D σ1 body and head domains (residues 170-455, PDB ID: 3S6X). The body consists of seven triple β-spiral repeats (β1-β7) and a small coiled coil (cc) inserted between β4 and β5. The globular head folds into a β-barrel formed by two Greek-key motifs. **(B)** T1L σ1 structure of the last three β-spiral repeats and the globular head domain (residues 265-470, PDB ID: 4GU3).

The sequences of T1L and T2J σ1 also possess a small heptad repeat pattern (of two full turns) within the body domain. Like T3D σ1, there are an arginine and a glutamate at predicted *g* and *e* positions that could stabilize the potential coiled coils with electrostatic interactions [60]. However, since a proline residue is observed in the consensus sequence in both cases, it is uncertain if these proteins also exhibit a small α-helical coiled coil at the equivalent position of T3D σ1 [19].

Currently, there is no structural information available for T2J σ1. For T1L σ1, the most complete X-ray structure (at 3.5 Å) comprises the head and the three most C-terminal β-spiral repeats (Figure 1.5) [17]. In both T1L and T3D σ1, the transition from the body to the head domain contains a flexible region that allows movement between the two domains. The observed linker region fits well with the region of higher flexibility near the head domain that has been predicted from electron micrographs [63].

Head Domain

The C-terminal one third of the σ1 molecule folds into two Greek-key motifs (β-strands A-D and β-strands E-H) that assemble into a β-barrel forming the globular head domain [63]. Apart from the D-E-loop, which contains a 3_{10}-helix, the other β-strand connecting loops are short. The head harbors an unusual aspartic acid cluster that is located at the

lower, N-terminal part of the head and stabilizes the trimer. This arrangement may be involved in a conformational change upon exposure of the molecule to low pH [75].
The σ1 head domain binds to the serotype-independent receptor JAM-A, and in the case of T1L σ1, it can additionally bind to glycan receptors. Two serotype-specific neutralizing antibodies, 5C6 and 9BG5, which target the σ1 protein of T1 and T3, respectively, also engage the head domain.

1.2.2 Receptor Interactions

The σ1 protein specifically interacts with host cell receptors and is therefore a major determinant of virus cell selection, spread, and tropism.

Interactions with JAM-A

All reovirus serotypes use JAM-A as a cellular receptor [15]. The JAM-A molecule belongs to the immunoglobulin superfamily (IgSF) and is localized at tight junctions of endothelial and epithelial cells and is also expressed on leukocytes and platelets. JAM-A plays a role in the regulation of epithelial cell polarity, leukocyte transmigration, and in the stabilization of the blood-brain barrier [76].
The JAM-A molecule is composed of two extracellular Ig-like domains termed D1 and D2, a single transmembrane region, and a short cytoplasmic tail. JAM-A forms homodimers via mostly ionic interactions between the membrane-distal, N-terminal D1 domains [77,78].
The 3.4 Å resolution structure of the T3D σ1 head domain in complex with human JAM-A D1 provided detailed insights into σ1 receptor recognition [79]. The lower part of the σ1 head binds to JAM-A at the site that is also involved in JAM-A homodimer formation. The receptor binding site on σ1 comprises the 3_{10}-helix in the D-E-loop and at the head-body transition the most C-terminal β-spiral repeat and a short α-helix. Each σ1 monomer of the trimeric head is ligated by one JAM-A molecule (Figure 1.6). As the affinity of JAM-A for σ1 is higher than the affinity of JAM-A for itself, binding of JAM-A by σ1 leads to the separation of the JAM-A homodimer [80].

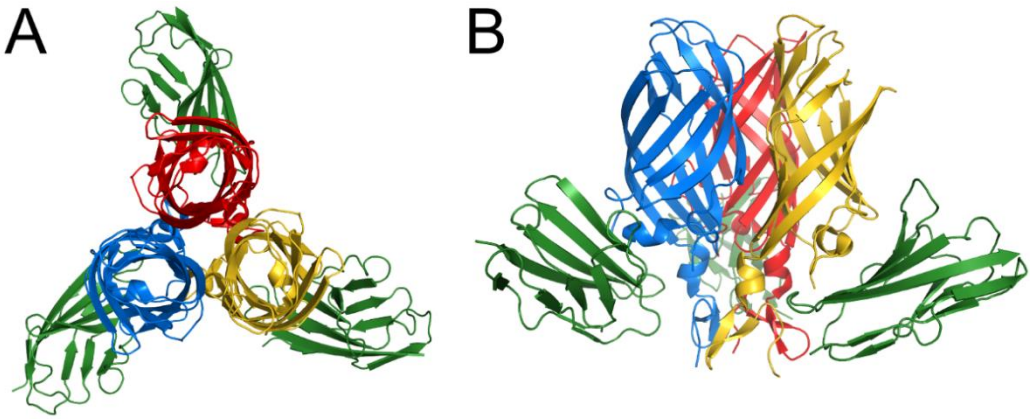

Figure 1.6 Crystal structure of T3D σ1 in complex with human JAM-A D1. Cartoon representation of the complex (PDB ID: 3EOY). The σ1 head is colored in blue, red and yellow, and JAM-A D1 is colored in green. **(A)** View along the threefold axis. **(B)** View perpendicular to the threefold axis. Modified from [79].

JAM-A engagement by σ1 is required for reovirus hematogenous dissemination from the site of primary replication [81]. Residues involved in JAM-A binding are conserved among the reovirus serotypes. Thus, the σ1 molecules of T1L, T3D, and probably T2J engage JAM-A in a similar manner and make the recognition of JAM-A unlikely to be responsible for differences in pathogenesis [82]. When JAM-A-deficient mice are inoculated intracranially, with T1L and T3D, the distinct patterns of tropism in the CNS are maintained. Therefore, the serotype-specific differences, which segregate with the S1 gene, can be best attributed to σ1 engagement of cell-surface receptors other than JAM-A.

The Nogo receptor (NgR1) serves as a receptor for reovirus infection of neurons [16]. Virions but not ISVPs are able to engage NgR1. This finding indicates that either σ3, which is lost during virion-to-ISVP conversion, or a specific virus-associated σ1 conformation mediates NgR1 binding. Both T1 and T3 strains can infect non-neuronal cells that express NgR1 [16]. Studies using reassortant viruses show that those viruses that differ only in the σ1 proteins have similar binding affinities for NgR1, while T1L displays a greater affinity for NgR1 compared to T3D (Dermody, unpublished). Thus, σ3 is more likely the reovirus ligand for NgR1. These findings suggest a model in which σ1 facilitates binding to target cells in the CNS by engagement of cell-surface glycans, and σ3 then mediates entry into neurons by binding to NgR1.

Interactions with Carbohydrate Receptors

Sialic acid-containing glycans are present on cell surfaces of all vertebrates and some invertebrates and are involved in numerous functions, including self-recognition, cell-cell adhesion, extrinsic and intrinsic signaling. They moreover serve as receptors for a variety of viruses [83].

Sialic acid is commonly found as a terminal monosaccharide connected by α(2,3)- or α(2,6)- linkage to various carbohydrates or by an α(2,8)-linkage to another sialic acid [84]. The underlying glycan chains can vary widely in composition and length and can be linked to proteins or lipids, creating a large number of diverse sialylated glycan structures. Virus-sialic acid interactions are typically of low affinity and are amplified by the multivalency of binding sites present on the virus surface [20,85].

The reovirus serotypes engage sialic acid using different parts of the σ1 molecule and have different hemagglutination profiles [17,19,86,87]. T1L specifically binds to both terminal carbohydrate portions of the ganglioside GM2 using a small cleft in the σ1 head domain [17]. In contrast, T3D binds a range of differently linked sialylated glycans near the N-terminal part of the σ1 body domain (Figure 1.7).

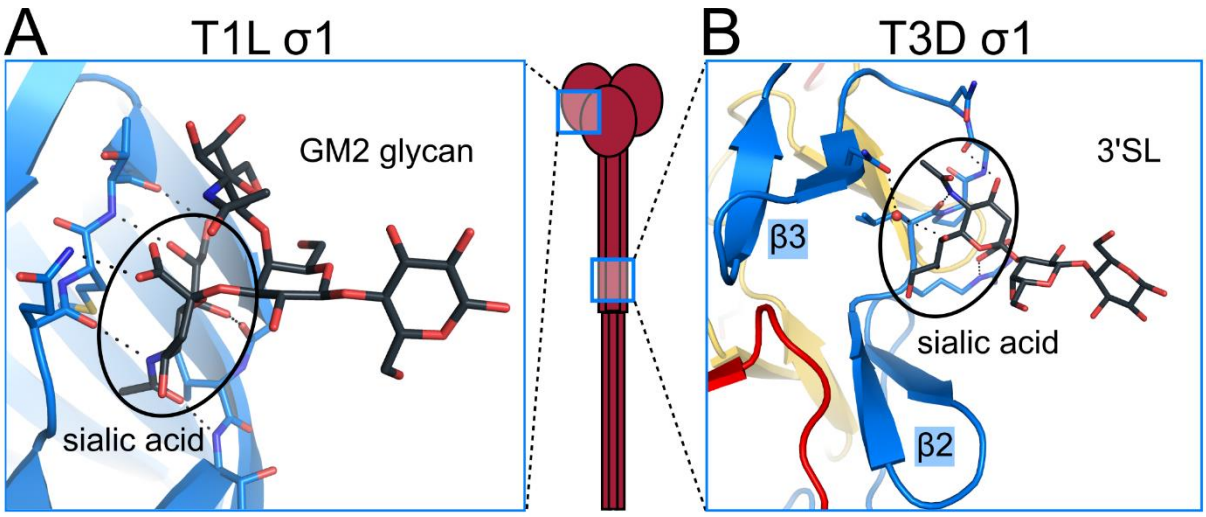

Figure 1.7 Glycan binding sites of T1L σ1 and T3D σ1. Ribbon drawing of the σ1 trimer colored in blue, red, and yellow. Carbohydrates are shown in black. A schematic σ1 molecule is shown in the middle and indicates the location of the carbohydrate binding sites on T1L σ1 and T3D σ1, respectively. **(A)** T1L σ1 binds to the glycan moiety of the ganglioside GM2 in the head domain. (PDB ID: 4GU3). Both terminal carbohydrates of the GM2 glycan contact σ1. Most interactions are formed between sialic acid (black circle) and backbone atoms of the protein. **(B)** The glycan binding site of T3D σ1 is located in the body domain in a loop region connecting β-spiral repeat β2 and β3. The terminal sialic acid of α(2,3)-sialyllactose (3'SL) mostly contributes to interactions with σ1.

Crystal structures of T3D σ1 in complex with α(2,3)-sialylactose, α(2,6)-sialyllactose, and α(2,8)-disialyllactose elucidated the carbohydrate binding site at a loop connecting β-spiral repeats β2 and β3 [19]. In each complex structure, the terminal sialic acid contributes mostly to contacts with σ1. In newborn mice, the neurovirulence of wildtype T3D is greater in comparison to a mutant virus that lacks the capacity to bind sialic acid, indicating that carbohydrate receptor binding has an influence on reovirus pathogenesis [88].

Target of Neutralizing Antibodies

The reovirus-induced neutralizing antibody response is mainly directed against the σ1 protein [89]. Monoclonal antibodies (mAbs) that target σ1 have been used to identify distinct functional domains of the σ1 protein [90].

The mouse IgG2a mAbs 5C6 and 9BG5 target σ1 of T1 and T3 reovirus, respectively, and their neutralization capacity has been demonstrated by classical plaque-reduction neutralization experiments [90-93]. Cross-reactivity of both mAbs with the non-cognate σ1 protein occurs [94-96]. Both mAbs are highly effective *in vivo* at protecting neonatal mice from reovirus-induced disease [91,94]. 5C6 and 9BG5 inhibit virus-induced hemagglutination (HA), although HA inhibition by 9BG5 is not always observed [90,91,96,97]. Sequence-analysis of reovirus escape mutants identified specific residues in the σ1 head domain that are required for efficient neutralization by 5C6 and 9BG5 [92,98], but the precise binding epitopes and mechanisms of neutralization by these antibodies are unknown.

2 Objectives

The structural investigation of the reovirus attachment protein σ1 and its interaction with neutralizing mAbs is the focus of the present thesis. The reovirus σ1 protein binds host cell-receptors, is a major target of the neutralizing antibody response, and is assumed to undergo a conformational change during the reovirus cell entry process.

Interactions between σ1 and cell-receptors (glycans and JAM-A) are well understood, while less is known about how neutralizing mAbs engage σ1 and inhibit reovirus infection. To date, only limited information exists about the conformational change of σ1. It is assumed that flexible regions predicted within the molecule are involved in the structural rearrangement. At the beginning of this study, structural detail at high resolution was available for parts of the σ1 molecule (for the body and the head domain of T3 σ1, for small regions of the tail, parts of the body and the head domain of T1 σ1), but not for the tail of T3 σ1 or the connection of the tail and the body domain. The major objectives of this thesis were to:

- identify the complete epitope of the serotype-specific mAbs 5C6 and 9BG5
- define the interactions of these mAb with σ1 on a structural basis to obtain insights about the mechanism of neutralization
- identify how reovirus variants escape mAb 5C6 and 9BG5 neutralization
- determine affinities and kinetics for the binding of σ1 with 5C6 and 9BG5 Fabs
- determine affinities of σ1 for the serotype-independent receptor JAM-A
- solve the structure of the σ1 tail domain
- obtain information about flexible regions within the fibrous part of the σ1 molecule to gain insight into the proposed structural change

3 Materials and Methods

3.1 Chemicals

All chemicals used in this work were of analytical reagent grade and obtained from: Roth (Karlsruhe, Germany), Sigma-Aldrich (Deisendorf, Germany), Merk (Darmstadt, Germany), GE Healthcare (Uppsala, Sweden) and Hampton research (Aliso Viejo, USA).

3.2 Bacterial Strains

The *Escherichia coli* (*E. coli*) strain XL 10 gold (Stratagene, USA) was used for amplifying plasmid-DNA. Proteins were produced in *E. coli* BL21 (DE3) or Rosetta 2 (DE3) strains (Novagen, Darmstadt, Germany).

***E. coli* strain**	**Genotypes**
XL 10 gold	Tet^RΔ(*mcr*A)183Δ(*mcr*CB-*hsd*SMR-*mrr*)173 *end*A1 *sup*E44 *thi*-1 *rec*A1 *gyr*A96 *rel*A1 lac Hte [F´ proAB *lacI*^{q}ZΔM15 Tn10 (Tet^R) (Kan^R) Amy]
BL21 (DE3)	F^- *ompT hsdS*$_B$(r_B^- m_B^-) *gal dcm* (DE3)
Rosetta 2 (DE3)	F^- *ompT hsdS*$_B$(r_B^- m_B^-) *gal dcm* (DE3) pRARE2 (Cam^R)

3.3 Plasmids

Plasmid	**Resistence**	**Specifications**	**Origin**
pET15b	Amp	T7 promotor, N-terminal His_6-tag, thrombin cleavage site, MCS	Novagen, Germany
pET16b	Amp	T7 promotor, N-terminal His_6-tag, Factor Xa cleavage site, MCS	Novagen, Germany
pET28b	Kan	T7 promotor, N-terminal His_6-tag, thrombin cleavage site, MCS, C-terminal His_6-tag	Novagen, Germany
pE-SUMOpro	Amp	T7 promotor, N-terminal His_6-Smt3-tag, UlpI cleavage site	LifeSensors, USA
pBacPAK	Amp	T7 promotor	Addgene, UK
pIBA-GCN4tri	Amp	tet promotor, N-and C-terminal GCN4tri, C-terminal His_6-tag	Dirk Linke, MPI Tübingen

3.4 Primers

Primers were bought from biomers.net (Ulm, Germany) or for sequencing from Eurofins Genomics (Ebersberg, Germany).

Primer	Sequence
Cloning primer	
T1L σ1(2-470)for	CAGGTCTCCAGGTGATGCATCTCTCATTACAGAGATACG (*BsaI*)
T1L σ1(29-470)for	CGCGCGCATATGGAGGAAATCAAGAAACAAGTCC (*NdeI*)
	CGCGCGCATATGGAGGAAATCAAGAAACAAGTCC (*NcoI*)
	CAGGTCTCCAGGTGAGGAAATCAAGAAACAAGTCCAG (*BsaI*)
T1L σ1 (2/29-470)rev	GCGGGATCCTACCTCACATTGCATGGATACATGATCGTC (*BamHI*)
	GCTCTAGATTACCTCACATTGCATGGATACATGATCGTCC (*XbaI*)
T1L σ1(29-159)for	CGACCCATGGCAGAGGAAATCAAGAAACAAGTCCAG (*NcoI*)
T1L σ1(29-159)rev	GGTTACAAGGTTAGATGGTCTAATCAATTAGGATCCCGC (*BamHI*)
T3D σ1(28-455)for	CATTAGCTAGCCTTGAATCAAGGGTCTCGGCGCTCGAG (*NheI*)
T3D σ1(30-455)for	ATAATCTCGAGTCAAGGGTCTCGGCGCTCGAGAAGAC (*XhoI*)
	CATAGCTAGCAGGGTCTCGGCGCTCGAGAAGAC (*NheI*)
T3D σ1(28/30-455)rev	GATGGATCCTACGTGAAACTACGCGGGTACGAAACG (*BamHI*)
	GATGCTCGAGCTACGTGAAACTACGCGGGTACGAAAC (*XhoI*)
T3D σ1(1-xxx)for	CATAGCTAGCATGGATCCTCGCCTACGTGAAGAAG (*NheI*)
xxx = 234/ 251/ 291	
T3D σ1(25-xxx)for	CATAGCTAGCTCAAAAGGGCTTGAATCAAGGGTCTCG (*NheI*)
xxx = 234/ 251/ 291	
T3D σ1(1/25-234)rev	GGCCGAAGCTTCTAGAGAGTCAAGTTATTATTAACTATCTGG (*HindIII*)
T3D σ1(1/25-254)rev	GCTGAAGCTTCTATTGCTCAGTTGCGCCTATCCTTG (*HindIII*)
T3D σ1(1/25-291)rev	GCTGAAGCTTCTACGATCTAACAGTTAGCTGTCCACTAG (*HindIII*)
Mutagenesis primer	
T1L σ1(2-117/stop)for	CAGTCTGGATACGTAAACGTCTAATCTC
T1L σ1(2-117/stop)rev	GAGATTAGACGTTTACGTATCCAGACTG
T1L σ1(2-178/stop)for	GGAGACGTCTTAGGTGACGACGG
T1L σ1(2-178/stop)rev	CCGTCGTCACCTAAGACGTCTCC
T1L σ1(29-249/stop)for	GGAGAGATTACATTGGTGAGTTAAATCAATGAATTGCC
T1L σ1(29-249/stop)rev	GGCAATTCATTGATTTAACTCACCAATGTAATCTCTCC
T1L σ1(29-264/stop)for	CACTGGAATCAGCGTAAATCGATTCAGTTTTACC
T1L σ1(29-264/stop)rev	GGTAAAACTGAATCGATTTACGCTGATTCCAGTG
T1L σ1(29-303/stop)for	CTGTCGTTACGGTGACGTTTGACTCTTCCGACATACAGG
T1L σ1(29-303/stop)rev	CCTGTATGTCGGAAGAGTCAAACGTCACCGTAACGACAG
T3D σ1(N182A)for	CTCTCAATCCGTAATGCCCGTATGACCATGG
T3D σ1(N182A)rev	CCATGGTCATACGGGCATTACGGATTGAGAG
T3D σ1(R161A)for	GGATTTCGAATCTGCGATATCCACATTAGAGC
T3D σ1(R161A)rev	GCTCTAATGTGGATATCGCAGATTCGAAATCC
T3D σ1(Q155V)for	CGAGTAACATCCATAGTAGCGGATTTCGAATC
T3D σ1(Q155V)rev	GATTCGAAATCCGCTACTATGGATGTTACTCG
T3D σ1_ΔVTSIfor	GACGTTACGAGTAGCGGATTTCGAATCTAGGATATCCACATTAGAG
T3D σ1_ΔVTSIrev	CCGCTACTCGTAACGTCAGAGTTGATAGCTCGGTGGTCAATG
T3D σ1(154+QST)for	CGAGTAACATCCATA**CAGAGTACA**GTAGCGGATTTCGAATCTAG
T3D σ1(154+QST)rev	**CTG**TATGGATGTTACTCGTAACGTCAGAGTTGATAGCTCG
T3D σ1(1-168/stop)for	CACATTAGAGCGCACGTAGGTCACTAGCGCG
T3D σ1(1-168/stop)rev	CGCGCTAGTGACCTACGTGCGCTCTAATGTG
Sequencing primer	

T7 for	TAATACGACTCACTATAGGG
T7 term	CTAGTTATTGCTCAGCGGT

3.5 Commercial Crystallization Screens

Screen	Company
Crystal Screens I, II	Hampton research, Aliso Viejo, USA
Wizard I, II, III, IV	Emerald BioSystems, Bainbridge Island, USA
JCSG	Molecular Dimensions, Suffolk, UK
PEG ION	Hampton research, Aliso Viejo, USA
Additive screen	Hampton research, Aliso Viejo, USA

3.6 Molecular Biology

3.6.1 Glycerol Stocks

E. coli culture glycerol stocks were prepared by mixing 900 µl of a bacterial overnight culture with 300 µl sterile glycerol solution (50% v/v). The solutions were flash frozen with liquid nitrogen and stored at -80°C.

3.6.2 Purification of Plasmid DNA

Plasmid DNA from *E. coli* cultures was isolated using a miniprep kit (Promega, Mannheim, Germany) according to the manufacturer's protocol. The DNA concentration was determined via absorbance at a wavelength of 260 nm (NanoDrop ND-1000, Thermo Scientific, Waltham, USA).

3.6.3 Polymerase Chain Reaction (PCR)

Polymerase chain reactions (PCR) were performed to amplify DNA. In each case, 50 µl total reaction volume was prepared with 100 ng of template DNA, 200 µM dNTPs, 200 nM primers and 5 U ReproFast DNA-polymerase (Genaxxon bioscience, Ulm, Germany). The annealing temperature (T_A) of the reaction was selected to be 10-15°C below the primer melting temperature and the time for the elongation step (at 72°C) was calculated based on the length of the desired insert (1 min per 1 kb).

PCR Program:			
1.	1x	94°C	2-7 min
2.	30x	94°C	1 min
		T_A°C	45 s
		72°C	30-90 s
3.	1x	4°C	1-8 h

3.6.4 Site-directed Mutagenesis

The GENEART® site-directed mutagenesis kit (Life Technologies, USA) was used to introduce base substitutions, insertions of 9, or deletions of 12 nucleotides into DNA plasmids following the manufacturers' protocol. The annealing temperature (T_A) of the reaction was selected to be 10-15°C below the primer melting temperature and the time for the elongation step (at 68°C) was calculated based on the length of the plasmid (30 s per 1 kb).

3.6.5 Agarose Gel Electrophoresis

Agarose gel electrophoresis was used to analyze and purify the PCR reaction products. 0.3 g agarose was dissolved in 30 ml TAE buffer by heating. Prior to gelation 3 µl GelRed (Biotium Inc, Fremont, USA) were added. Marker (O´GeneRuler 1kb DNA ladder, Qiagen, Hilden, Germany) and PCR samples mixed with 6x loading dye were applied. The electrophoresis was performed for 1 h at 100-120 V, and the gel was analyzed using UV light. DNA was extracted from the gel by using the QIAquick gel extraction kit (Qiagen, Hilden, Germany) and following the manufacturer's protocol, or by centrifugation through a 0.22 µm filter (Costar® Spin-X centrifuge tube filter).

50x TAE Buffer
2 M Tris
50 mM EDTA pH 8
57% (w/v) acetic acid

3.6.6 Restriction Digestion and Ligation

Plasmids and PCR products were digested with the respective restriction enzymes (NEB, Frankfurt, Germany) following the manufacturer´s protocol. The enzymes were heat-inactivated at 65°C for 20-30 min and the digested plasmids were purified by agarose gel

electrophoresis. The DNA insert was ligated with 100 ng plasmid DNA and a molar insert-to-plasmid ratio of 1:1, 3:1 or 5:1.
10 µl ligation solution using 0.5 µl T4 ligase (3 U/µl, Promega, Mannheim, Germany) and the corresponding 5x buffer was prepared and incubated either overnight at 20°C or with a temperature gradient of 1°C per 1 h ranging from 25-11°C.

3.6.7 Transformation of Competent Bacteria Cells

For transformation, 100 ng plasmid DNA or 5 µl ligated plasmid solution was added to 50 µl competent bacteria cells, and incubated for 20 min on ice. The cells were exposed to a heat-shock at 42°C for 30-45 s followed by incubation on ice for 2 min. After adding 400 µl LB-media, the cells were allowed to grow for 1 h at 37°C and 750 rpm. From the suspension 100 µl were plated on LB-agar supplemented with the according antibiotics and incubated overnight at 37°C.

Lysogeny Broth (LB) Media
1% (w/v) tryptone
0.5% (w/v) yeast extract
1% (w/v) NaCl

LB-Agar Media
1% (w/v) tryptone
0.5% (w/v) yeast extract
1% (w/v) NaCl
6% (w/v) agar

3.7 Microbiology Methods

3.7.1 Cultivation of *E. coli*

For overnight cultures, 10-15 ml LB-media supplemented with the according antibiotics were either inoculated with bacteria from glycerol stocks, a single bacteria colony from an agar plate, or with 400 µl transformation solution.
For test expressions 50-100 ml and for protein purification, 1-4 l LB-media supplemented with the according antibiotics were inoculated with overnight bacterial culture (~ 1:500). The bacteria were then grown at 37°C and induced at an OD_{600} of 0.4-0.6 with 0.2-1.0 mM IPTG or, in case of $(GCN4)_3$-T1L σ1, with 0.2 µg/ml anhydrotetracycline (AHTC). The bacteria grew overnight at 20-25°C and 110 rpm, while $(GCN4)_3$-T1L σ1 was produced at 37°C and the cells were harvested 5 h after induction. During test expressions, samples were collected at various time points, and similar amounts of cells were analyzed with SDS-PAGE.

3.7.2 Cell Harvesting

Cells were harvested by centrifugation at 7000 rpm (rotor: SLC-4000, Sorvall) for 10 min at 4°C. Cell pellets were either directly used for protein purification, or flash frozen in liquid nitrogen and stored at -80°C.

3.8 Protein-Biochemistry

3.8.1 Discontinuous SDS-Polyacrylamide Gel Electrophoresis (SDS-PAGE)

SDS-PAGE was used to separate protein mixtures according to their molecular weight in an electrical field and to analyze the protein purity. SDS-PAGE gels with 12 or 15% separation and 4% stacking gels were prepared. Samples were mixed with 4x SDS-sample buffer and heated to 90°C for 2-5 min. The electrophoresis was performed for 1 h at 45 mA. Gels were stained with Coomassie staining solution for 10-15 min on an orbital shaker.

4 x SDS gels	4% Stacking gel	12% Separation gel	15% Separation gel
H_2O (ml)	6.1	5	3.5
1.5 M Tris pH 6.8 (ml)	2.5		
1.5 M Tris pH 8.8 (ml)		3.75	3.75
10 % (w/v) SDS (µl)	100	150	150
30% Acrylamide-bisacrylamide (ml)	1.3	6	7.5
TEMED (µl)	10	7.5	7.5
10% (w/v) APS (µl)	100	150	150

4x SDS Sample Buffer
20 ml 1 M Tris pH 6.8
10 ml 10% SDS
1.63 ml 0.5 M EDTA pH 8.0
4 ml β-mercaptoethanol
20 mg bromophenol blue

Coomassie Staining Solution
0.25 g Coomassie Brilliant Blue G250
100 ml ethanol
900 ml H_2O
2.5 ml conc. HCl

3.8.2 Cell Lysis

Per 1 g cells, 4-6 ml lysis buffer was used for resuspension. The solution was supplemented with 1 mM PMSF and the cells were lysed by sonication. Lysis tests with 1 ml volume were conducted with an amplitude of 30% and an overall pulse time of 0.5-1 min (cycles of 0.5 s pulse on and 5 s off). The solution was centrifuged at 12 000 rpm (Eppendorf centrifuge) for 30 min at 4°C.

Lysis of 20-30 ml cell solutions was done with an amplitude of 40% and an overall pulse time of 2-4 min (cycles of 0.5 s pulse on and 0.5 s off), and the lysed cells were centrifuged at 17 000 rpm (rotor: SS-34, Sorvall) for 1 h at 4°C. The supernatant was sterile filtered through a 0.22 µm filter.

Protein	Lysis Buffer
His_6-SUMO-T1L σ1	50 mM Tris pH 7.8
	3 mM EDTA
T1L σ1(29-470)	40 mM Tris pH 8.5
T1L σ1(cc-body)	50 mM Tris pH 8.0
	300 mM NaCl
	10 mM imidazole
$(GCN4)_3$-T1L σ1	20 mM Tris pH 7.4
	40 mM NaCl
	5 mM $MgCl_2$
T1L σ1(29-159)	40 mM HEPES pH 7.4
	150 mM NaCl
T3D σ1(cc and cc-body)	50 mM Tris pH 8.0
	300 mM NaCl
	10 mM imidazole

Lysis Test	Buffer Condition
1	100 mM Tris pH 7.6, 10% glycerol
2	100 mM Tris pH 7.6, 50 mM LiCl
3	100 mM HEPES pH 7.0, 100 mM KCl
4	100 mM Tris pH 8.2, 50 mM NaCl, 10% isopropanol
5	100 mM HEPES pH 7.0, 1 M $MgSO_4$
6	100 mM Tris pH 8.2, 50 mM NaCl, 100 mM urea
7	100 mM KH_2PO_4, 2.5 mM $ZnCl_2$ pH 4.3
8	100 mM KH_2PO_4, 50 mM $(NH_4)_2SO_4$ pH 6, 1% Triton X-100
9	100 mM HEPES pH 7.0, 100 mM sodium glutamate, 5 mM DTT
10	100 mM Triethanolamin, 50 mM LiCl, 5 mM EDTA pH 8.5

11	100 mM sodium acetate, 1M $MgSO_4$ pH 5.5
12	100 mM sodium acetate, 100 mM KCl, 0.1% n-Octyl-β-glucoside pH 5.5
13	50 mM HEPES pH 8.5, 1 M L-arginine
14	50 mM HEPES pH 8.5, 0.3 M L-arginine
15	50 mM HEPES pH 6.5, 1 M L-arginine
16-18	50 mM MES pH 5.5-6.5, (steps of 0.5), 300 mM NaCl
19-24	50 mM HEPES pH 7-8.5 (steps of 0.5), 300 mM NaCl
25	50 mM Bicine pH 9, 150 mM NaCl

3.8.3 Refolding of Inclusion Bodies

The membrane-containing layer of the cell lysate pellet was removed, and the remaining pellet was resuspended in wash buffer. The solution was centrifuged at 17'500 rpm (rotor: SS-34, Sorvall) for 30 min and the pelleted inclusion bodies were resuspended in Tris buffer. This step was repeated three times. The resulting pellet was dissolved in denaturing buffer, and the solution was stirred overnight at ~ 25°C. Insoluble particles were separated by centrifugation at 15'000 rpm for 20 min (rotor: SS-34, Sorvall). The protein in the supernatant was refolded by dialysis against refolding buffer. After 24 h and two buffer changes, the protein solution was sterile filtered (0.22 µm) and concentrated to ~ 7 mg/ml. The protein was transferred into buffer A by using a PD-10 desalting column (GE Healthcare) following the manufacturer's protocol.

Protein	Buffer	Composition
$(GCN4)_3$-T1L σ1	Wash buffer	50 mM Tris pH 7.8
		10% Triton X-100
	Tris buffer	50 mM Tris pH 7.8
		50 mM NaCl
	Denaturing buffer	20 mM Tris pH 7.8
		6 M GdmCl
		500 mM NaCl
		10% glycerol
	Refolding buffer	20 mM MOPS pH 7.2
		400 mM NaCl
		10% glycerol
	Buffer A	20 mM HEPES pH 7.4
		25 mM NaCl

3.8.4 Ni-Affinity Chromatography

Ni-affinity chromatography was used as a first purification step for His_6-tagged proteins. Single-use spin columns (spin trap columns, GE Healthcare) were utilized for a first expression screening of new constructs. From lysis tests 1-3 ml of supernatant were applied to the equilibrated spin columns by several centrifugation steps. After washing with lysis buffer, the proteins were eluted by several centrifugation steps using buffers with increasing imidazole concentrations (15-500 mM).

Protein	Buffer A	Buffer B
T1L σ1(cc-body)	50 mM Tris pH 8.6	50 mM Tris pH 8.6
T3D σ1(cc and cc-body)	300 mM NaCl	300 mM NaCl
	10 mM imidazole	500 mM imidazole

For large-scale purification, one or two connected 1 ml-columns (HisTrap FF Crude, GE Healthcare) were equilibrated with ~ 10 column volumes of buffer A at a flow rate of 1 ml/min. The filtered supernatant was loaded onto the column with a flow rate of 0.3-0.5 ml/min. The column was washed with 50-100 ml buffer A.

T3D σ1(cc and cc-body) constructs were digested on-column with thrombin after a washing step with 75 mM imidazole. Then, 100-150 U thrombin was dissolved in 1-2 ml buffer A and the solution was applied to the column using a syringe. The protein was incubated with thrombin at 20°C overnight, and cleaved T3D σ1 was eluted with 40 ml buffer A.

Tagged proteins were eluted from the column using linear or stepwise gradients of buffer B. Fractions were collected and analyzed by SDS-PAGE. The column was regenerated with 0.5-1 M imidazole and stored in buffer A or water.

3.8.5 Trypsin Digest in Solution

To remove the His_6-tag from T1L σ1(cc-body) constructs after Ni-affinity chromatography, the protein was mixed with a 1 mg/ml trypsin solution and incubated for 2-4 h at 20°C. The necessary amount of trypsin was estimated based on SDS-PAGE bands that correspond to T1L σ1. Approximately, 10-15 µg trypsin was used for a protein solution obtained out of 1 l LB-media. A 10-fold amount of trypsin inhibitor was added to stop the digestion before size exclusion chromatography was performed.

3.8.6 Anion Exchange Chromatography

Centrifuged and sterile filtered cell lysate was, if necessary diluted in buffer A to obtain a salt concentration < 50 mM, and applied to the equilibrated anion exchange chromatography column with a flow rate of 1-2 ml/min. In case of $(GCN4)_3$-T1L σ1, the protein solution obtained after refolding was applied to the equilibrated column with a flow rate of 0.5 ml/min.

The flow through was collected, and after washing the column with 10 column volumes buffer A bound protein was eluted stepwise or with a linear gradient of 20-30 column volumes to 50-100% buffer B. Protein-containing fractions were analyzed by SDS-PAGE.

Construct	Buffer A	Buffer B	Column
T1L σ1(29-470)	40 mM HEPES pH 8.5	40 mM HEPES pH 8.5 500 mM NaCl	DEAE FF 16/10
$(GCN4)_3$-T1L σ1	20 mM HEPES pH 7.4 25 mM NaCl	20 mM HEPES pH 7.4 500 mM NaCl	MonoQ 5/50
T1L σ1(29-159)	20 mM HEPES pH 7.4	20 mM HEPES pH 7.4 500 mM NaCl	DEAE FF 16/10

3.8.7 Ammonium Sulfate Precipitation

A saturated ammonium sulfate solution was supplemented with 100 mM Tris base to obtain a pH of 8.5. This solution was slowly added to a protein solution that was stirred on ice using a burette. When the protein solution started to precipitate, the addition of ammonium sulfate was stopped and the solution was kept on ice to complete the precipitation. The suspension was centrifuged for 30 min at 10'000 rpm (rotor: SS-34, Sorvall) to obtain the precipitated protein. With the supernatant, the procedure was repeated. Precipitated protein was recovered after each centrifugation step, dissolved in 25 mM HEPES pH 8.5, and analyzed by SDS-PAGE.

3.8.8 Cation Exchange Chromatography

Sterile filtered protein solution was applied to the equilibrated cation exchange chromatography column with a flow rate of 1-2 ml/min. The flow through was collected and, after washing the column with 50 ml buffer A, bound protein was eluted with a linear gradient to 100% buffer B. Protein-containing fractions were analyzed by SDS-PAGE.

The column was washed with a 1 M NaCl solution followed by re-equilibration in buffer A. For long-term storage, the column was placed on water followed by 20% ethanol.

Construct	Buffer A	Buffer B	Column
T1L σ1(29-470)	40 mM HEPES pH 8.5	40 mM HEPES pH 8.5 500 mM NaCl	HiLoad S Sepharose 16/10

3.8.9 Formation of σ1-Fab Complexes

The T1L σ1 head (308-470) and the T3D σ1 head (294-455) were expressed and purified following established protocols [17,75]. Fab fragments of the σ1-specific IgG2a antibodies 5C6 and 9BG5 were obtained from the Vanderbilt Antibody and Protein Resource (Nashville, USA).

Complexes were formed by mixing T1L σ1 with 5C6 Fabs or T3D σ1 with 9BG5 Fabs in a molecular ratio of 1 to 4 in each case. The mixtures were incubated at 4°C for 45 min. The stable complexes were separated from excess Fabs by using size-exclusion chromatography.

3.8.10 Size Exclusion Chromatography

Size exclusion chromatography (SEC) was used as final protein purification step. The chromatography column was equilibrated with SEC buffer at 1 ml/min. Dependent on the column dimensions, concentrated and sterile filtered (0.22 µm) protein samples of 0.5-2 ml volume were applied to the column with a flow rate of 1 ml/min. The absorbance at 280 nm was detected to visualize proteins that absorb at this wavelength. Proteins of interest with no or few Trp, Tyr, Phe and Cys residues were detected measuring the peptide bond absorbance at a wavelength of 215 or 230 nm.

Fractions were analyzed by SDS-PAGE and the ones containing the desired protein were pooled and concentrated. Purified protein was either kept at 4°C or flash frozen and stored at -80°C.

Protein	SEC buffer	Column
T1L σ1(29-470)	40 mM HEPES pH 8.5 100 mM NaCl	Sephacryl S-300 16/60
T1L σ1(cc-body)	40 mM Tris pH 8.6 (7.6) 150 mM NaCl	Superdex 200 16/60
$(GCN4)_3$-T1L σ1	40 mM HEPES pH 7.4 100 mM NaCl	Superdex 75 10/300
T1L σ1(29-159)	40 mM HEPES pH 7.4 150 mM NaCl	Superdex 200 16/60
T3D σ1(cc and cc-body) except 25-291	40 mM Tris pH 8.6 150 mM NaCl	Superdex 200 16/60
T3D σ1(25-291)	40 mM HEPES pH 7.4 150 mM NaCl	Superdex 200 16/60
σ1-Fab complexes	20 mM HEPES pH 7.4 150 mM NaCl	Superdex 200 10/300

* SEC buffer is sterile filtered (0.22µm) and degassed, 4°C.

3.8.11 Protein Concentration Determination

The protein concentration was determined by measuring the absorbance of the protein solution at 280 nm using the law of Lambert-Beer with the theoretical extinction coefficient of the protein at this wavelength.

The concentration of proteins that contain few or no Trp, Tyr and Cys residues was not determined. Their concentration for crystallization was adjusted by performing a precipitation test (3.8.12).

3.8.12 Precipitation Test

To select an appropriate protein concentration for crystallization trials, a precipitation test with dilution series of five ammonium sulfate (1.5-3 M) as well as five PEG4000 (10-30%) concentrations was performed at 20°C.

0.5-1 µl sterile filtered (0.22 µm) protein solution was pipetted onto a glass cover slide and an equal volume of the highest precipitant concentration was added. The drop was observed using a light microscope. The protein solution was further concentrated if the protein did not start to precipitate within ~ 3 min. When light to medium granular precipitate was directly observed, the lowest precipitation concentration was tested next.

The protein concentration was set when the protein precipitated (as light granular precipitate) in an appropriate amount of time (3-5 min) within the highest two to three precipitant concentrations but not in the lower ones.

3.8.13 Insertion of Iodide Ions into the σ1 Coiled Coil Core by Refolding

A concentrated protein solution (~50 µl) was diluted in unfolding buffer to a urea concentration of ~ 5 M. For refolding, the protein was transferred into Slide-A-Lyzer MINI Dialysis Devices (Pierce Protein Biology Products) and incubated in 500 ml refolding buffer. The buffer was exchanged twice and gently stirred at 4°C for 8 h. The protein was concentrated to the volume used in the beginning of the procedure.

Construct	Unfolding buffer	Refolding buffer
T1L σ1(29-159)	20 mM HEPES pH 7.5 100 mM NaI 6 M urea	20 mM HEPES pH 7.5 200 mM NaI

3.9 Surface Plasmon Resonance (SPR)

3.9.1 Affinity Determination

SPR experiments were conducted using a Biacore 2000 instrument (GE Healthcare) at 25°C. T1L σ1 (56 kDa) or T3D σ1 (53 kDa) were covalently immobilized on the surface of a CM5 sensor chip by amine coupling chemistry (NHS/EDC kit, GE Healthcare) with a density of 25 to 60 response units (RU). Deactivated flow cells served as references.
Concentration series of the Fab fragments (47 kDa) or human JAM-A D1D2 (23 kDa, amino acids 27-233), which served as analytes, were prepared by twofold dilutions in running buffer (10 mM HEPES pH 7.4, 150 mM NaCl, 0.05% P20). For affinity studies of JAM-A with σ1, JAM-A was injected onto the biosensor surface for 300 s with a dissociation time of 500 s at a flow rate of 50 µl/min.
For kinetic analysis of the binding of T1L σ1 to 5C6 Fabs, each Fab-concentration was randomly injected in duplicate or triplicate for 500 s with a dissociation time of 1300 s and a flow rate of 30 µl/min. For T3D σ1-binding experiments with 9BG5 Fabs, each Fab-concentration was randomly injected in duplicate for 210 s with a dissociation time of 450-600 s and a flow rate of 50 µl/min. To remove the Fab fragments from the σ1-coated surface after each cycle, 5 µl of regeneration solution (3.3 mM glycine, pH 1.7) was

injected. Due to the fast dissociation of JAM-A from T1L and T3D σ1, no regeneration step was necessary for these measurements.

Three or four independent experiments were performed in each case. Data from six different 5C6 concentrations ranging from 8 to 280 nM, and data from seven different 9BG5 concentrations ranging from 0.6 to 37.5 nM were double referenced and fitted to a 1:1 Langmuir binding model (BIAevaluation).

Ten different JAM-A concentrations, ranging from 0.02 to 10 µM for binding studies with T1L σ1, and ranging from 0.04 to 20 µM for binding studies with T3D σ1, were double-referenced and used for affinity determination with the BIAevaluation software (GE Healthcare) and Origin Pro (OriginLab, Northampton, USA).

3.9.2 JAM-A Binding to a σ1-mAb Complex

To investigate binding of JAM-A to a saturated σ1-mAb complex, a Biacore 2000 system was used at 25°C. T3D or T1L σ1 head was covalently coupled (NHS/EDC kit, GE Healthcare) to a CM5 sensor chip with an immobilization level of 25 RU and 60 RU, respectively.

In case of T3D σ1, 9BG5 antibodies (301 nM) were applied for 180 s at a flow rate of 20 µl/min. To ensure saturation of the T3D σ1-surface with the antibody, 9BG5 Fabs (8 µM) were coinjected for 120 s. Dissociation of 335 s was followed by an additional injection of 9BG5 antibodies (301 nM) for 180 s to achieve surface saturation. Afterwards, the soluble ectodomain of JAM-A (8 µM) was coinjected for 120 s. Dissociation was followed by regeneration with 3.3 mM glycine, pH 1.7. Subsequently, the response of 9BG5 Fabs (8 µM) or JAM-A (8 µM) to the regenerated T3D σ1-surface was tested by injection for 120 s.

In case of T1L σ1, first the response of 5C6 Fabs (4.4 µM) to σ1 alone was tested by an injection for 120 s at a flow rate of 20 µl/min. A dissociation step of 222 s was followed by regeneration with 3.3 mM glycine, pH 1.7. The response of the JAM-A ectodomain (14 µM) to σ1 alone was tested by injection for 120 s. Due to the fast off-rate no regeneration was required. 5C6 mAbs (4 µM) were injected for 600 s first and additionally for 300 s, to achieve surface saturation. Immediately afterwards 5C6 Fabs were injected (4.4 µM, 120 s) to determine whether all accessible binding sites of σ1 were bound by the mAb. The JAM-A ectodomain (14 µM) was injected for 120 s. Dissociation was followed by regeneration with 3.3 mM glycine, pH 1.7. Subsequently,

the response of 5C6 Fabs (4.4 µM) or JAM-A (14 µM) to the regenerated T1L σ1-surface was tested by injection for 120 s.

3.10 Crystallographic Methods

3.10.1 Protein Crystallization and Cryoprotection

Protein crystals are highly ordered three-dimensional arrays formed by non-covalent interactions between adjacent molecules. X-ray diffraction of a protein crystal can be used to determine the three-dimensional structure of the macromolecule.

The commonly used sitting or hanging drop vapor diffusion crystallization methods aim to crystallize proteins from a supersaturated aqueous solution by slowly increasing precipitant and protein concentrations. Precipitants are usually salts, alcohols, or water-soluble polymers such as polyethylene glycols (PEGs).

A drop of purified protein diluted with a crystallization condition is set on a plateau (sitting drop) or on a glass cover slide, which is then placed upside down (hanging drop), in an air-tight compartment. The compartment contains a reservoir with a larger volume of the crystallization condition. Ideally, the protein solution is under-saturated in the beginning. Due to lower concentrations of the solutes in the drop in comparison to the reservoir, water diffuses from the drop into the reservoir. The protein and precipitant concentrations increase in the drop and the solution becomes supersaturated. If the supersaturated solution reaches the nucleation zone, spontaneous nuclei can be formed and initiate crystal growth. Protein molecules from the solution can accumulate in an ordered manner at the nuclei and thereby the concentration of free protein decreases until the protein solution reaches the under-saturated zone. Then, crystals can still grow at the costs of other crystals. Among parameters that can influence crystallization are the initial protein and precipitant concentration, the pH, the presence of salts or organic compounds, and the temperature.

Seeding experiments are alternative approaches to induce nucleation within the crystallization trial. Solid material, e.g. small or crushed crystals or crushed spherulites, can be used as nucleating agents. The seeds are transferred to the crystallization drop, bypassing the nucleation step so that a lower level of supersaturation is required for crystal growth.

Depending on the size of the seeds added to the crystallization drop, the seeding technique is classified into macro- or mircoseeding. In macroseeding approaches, crystals of typically 5-50 µm in size are transferred to the pre-equilibrated protein solution

to continue crystal growth, while in the microseeding approach small nuclei are added to solutions of metastable supersaturation.

In the X-ray diffraction experiment, protein crystals are exposed to high doses of high energetic electromagnetic radiation. Incoherent scattering of the X-ray photons causes the formation of free reactive radicals, which lead to radiation damage of the crystal. To reduce the decay of the crystals during data collection, the crystals are cooled to cryogenic temperatures (100 K) that limit the movement of the free radicals. Prior to flash-cooling, the crystal is transferred into the crystallization solution containing a cryoprotectant agent. Cryoprotection prevents the formation of crystalline ice that would harm the crystal structure and lead to strong diffraction of the formed ice crystals.

Initial crystallization trials were performed in 96-well sitting drop crystallization plates (Intelli plate, Art Robbins Instruments, USA) with commercial screens and a reservoir volume of 100 µl. Drops were set containing 0.3 µl protein and 0.3 µl reservoir volume. A robot (freedom evo, Tecan) was used for pipetting. The plates were incubated at 4 or 20°C.

Crystallization hits were first optimized by hanging drop vapor diffusion experiments in 24-well crystallization plates (VDX plate, Hampton Research). Usually, the pH was varied versus the precipitation concentration. A reservoir volume of 500 µl was used, and drop sizes ranging from 1-3 µl with equal volumes of protein and reservoir solution. The reservoir was overlaid with 150 µl silicon oil to slow vapor diffusion in case of fast growing crystals.

To optimize crystals by microseeding, grown crystals were crushed in 50 µl mother liquor by vortexing for 5 min or for 90 s with a Teflon-bead (Seed-bead kit, Hampton research, USA). Serial tenfold dilutions were prepared with mother liquor. The microseeds were transferred to freshly prepared crystallization drops by either adding 0.2 µl or by dipping a cat-whisker first into the seed-containing solution and then striking through the new drop.

Crystal optimization trials using an additive screen (Hampton research, USA) were performed in 96-well crystallization plates (Greiner Bio-One, Germany). A crystallization condition was selected that previously yielded reproducible crystals. 100 µl of that solution was transferred into each reservoir and mixed with 10 µl of one of the 96 additive screen solutions with a robot (Hydra96, Robbins Scientific). Sitting drops of 0.3 µl protein solution and 0.3 µl reservoir solution were set by a robot (freedom evo, Tecan). For data collection, crystals were transferred to a crystallization solution containing MPD as cryoprotectant, if necessary and were flash-frozen in liquid nitrogen.

3.10.2 Data Collection and Data Processing

Background

X-ray radiation is scattered by the electrons of the molecules in the protein crystal. The scattered waves will cancel each other out by destructive interference, unless the path difference between two waves is an integer multiple of the wavelength. The constructive interference amplifies the intensity and diffraction as discrete and measureable maxima can be observed on a detector at a specific distance.

The high order of a protein crystal, an arrangement of small repeating units (unit cells) translated in three dimensions, is indispensable for the method as the conditions for constructive interference are fulfilled at corresponding positions between the unit cells, which leads to an amplification of the scattering signal. The unit cell that builds up the crystal lattice is defined by the length of the axes a, b and c, as well as by the angles α, β and γ between them. The unit cell can contain one or more entities that often can be transformed into each other by symmetry operations such as translation or rotation. Since proteins are chiral molecules, symmetry elements such as inversion centers or mirror planes that would change the chirality of the molecules are not possible in protein crystals. Symmetry operators that describe the internal symmetry of the unit cell and apply to the entire crystal are crystallographic symmetry operators that divide the unit cell into smaller fractions, termed asymmetric units. The content of the asymmetric unit can have symmetry, but this additional symmetry, termed non-crystallographic symmetry (NCS), only applies to the molecules inside the asymmetric unit. The geometry of the unit cell and the crystallographic symmetry operators define the space group of a crystal.

The virtual lattice that can be generated from the recorded diffraction maxima is related to the crystal lattice by an inverse relationship and is termed reciprocal lattice. The Miller indices h, k and l specify lattice planes in the reciprocal lattice and their direction in the three-dimensional crystal. Each diffraction spot can be constructed as the reflection of the incident beam on a set of parallel planes with equal distance. Sir W. Lawrence Bragg described the conditions under which constructive interference is achieved, causing a reflection (h,k,l) on a detector. A reflection can only occur if the path difference of two waves that hit crystal lattice planes spaced with the distance d under angle θ is an integer multiple of the wavelength (Bragg's law, equation 3.1).

$$n\lambda = 2d\ sin\theta \qquad \textbf{(3.1)}$$

A graphical construction of reciprocal lattice points that fulfill Bragg's law is the Ewald sphere (Figure 3.1). A sphere with radius 1/λ is drawn around a crystal. Only the reciprocal lattice points (h,k,l) that lie on the surface of the sphere can be observed as reflections. The lattice point (0,0,0) is the origin of the reciprocal lattice and defined as the position where the incident beam intersects the Ewald sphere. As only a fraction of reflections can be observed at a given crystal orientation, the crystal in the center of the sphere, and with it the reciprocal lattice, is rotated around its own origin, perpendicular to the X-ray beam, during data collection. Different lattice points will then intersect the Ewald sphere and will be recorded. To collect all reflections of a crystal, images are collected for every 0.1-2° of rotation. The range of degrees that needs to be recorded for a complete data set depends on the symmetry of the crystal.

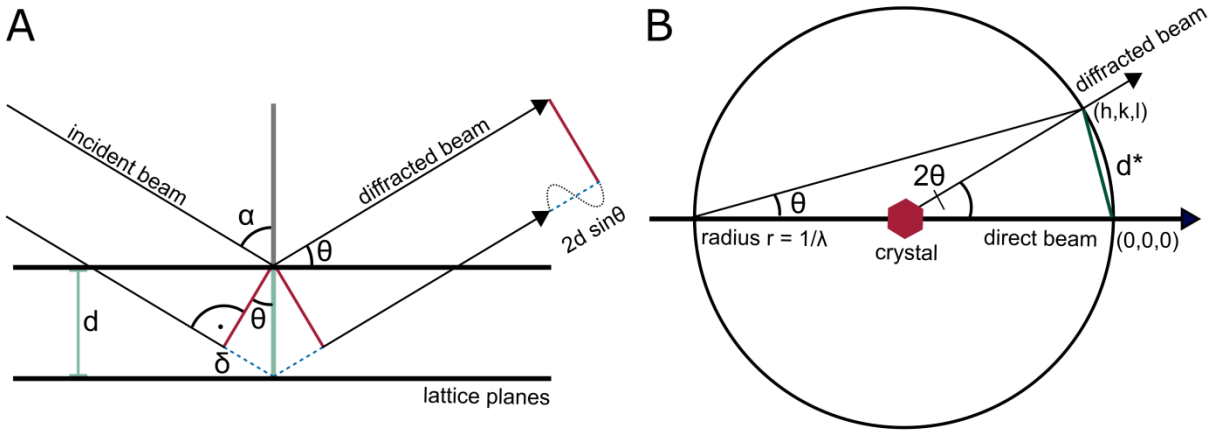

Figure 3.1 Bragg's law and Ewald sphere. (A) Graphical representation of Bragg's law. For constructive interference, the path difference of two waves diffracted at parallel crystal lattice planes must be an integer multiple of the wavelength. d: distance between two lattice planes, θ:angle of incidence. **(B)** Ewald sphere. r: radius of the sphere 1/λ, (h,k,l): coordinates of the reflection in reciprocal space, d*:1/d.

Every diffraction spot on a detector corresponds to one set of lattice planes and can be assigned to the corresponding reciprocal space coordinates (h,k,l) during indexing of the data. The obtained information of the spot positions together with the distance of the detector and the used wavelength allows the calculation of possible unit cell parameters for each lattice type. Depending on the unit cell parameters and how well they fit the geometric requirements of a crystal system, the most likely lattice type is chosen. For indexing only a subset of the images is typically used.

While the position of the diffraction spots on the images is dependent on the geometry of the crystal and the experiment, the intensity and phase are dependent on the content of the unit cell (on the structure of the molecules).

During integration, the intensity of each reflection is determined and the unit cell and data collection parameters are concurrently refined. The same reflection may have been collected at different intensity values during data collection caused by X-ray radiation damage or intensity fluctuations of the incident beam. Scaling attempts to make the data internally consistent and applies scaling factors to minimize the differences between the same reflections. Further, partial reflections that were not fully recorded on a single image are added, and symmetry-related reflections are merged.

The output of scaling contains a list of all unique reflections (h,k,l) with their intensities, information about the best determined values for of the unit cell, and data collection parameters as well as statistics to assess data quality.

The data processing R-factors calculate the consistency of repeated measurements and thereby quantify the overall quality of the intensity data. The linear merging R-factor, $R_{merge,}$ measures the ratio between the sum over the deviations of each redundant reflection from the mean intensity value for that reflection and the sum over the intensities of all redundant reflections (equation 3.2). R_{merge} increases with higher redundancy, meaning that a low-redundant dataset appears better than a high-redundant one, which is counterintuitive as with increasing multiplicity the mean intensity of a reflection should be determined with higher accuracy. The redundancy-independent R-factor R_{meas} was therefore introduced and corrects the rise of the R-factor with redundancy (equation 3.3) [99]. The R-factors typically increase with higher resolution, while the signal to noise ratio, I/σI, decreases as the effect of small irregularities within a crystal increases.

$$R_{merge} = \frac{\sum_{hkl}\sum_{i}^{n}|I_{hkl,i} - \bar{I}_{hkl,i}|}{\sum_{hkl}\sum_{i}^{n} I_{hkl,i}} \quad \textbf{(3.2)}$$

$$R_{meas} = \frac{\sum_{hkl}\sqrt{\frac{n}{n-1}}\sum_{i}^{n}|I_{hkl,i} - \bar{I}_{hkl,i}|}{\sum_{hkl}\sum_{i}^{n} I_{hkl,i}} \quad \textbf{(3.3)}$$

A different data quality indicator, the correlation coefficient $CC_{1/2}$, was introduced recently [100]. To obtain $CC_{1/2}$, the data are divided into two parts, each containing a random half of the measurements of each unique reflection, and the Pearson correlation coefficient between the average intensities of each subset is determined. $CC_{1/2}$ is near 1.0 at low

resolution and drops to 0 at high resolution. The Student's t-test can indicate where statistical significance ends.

To discard weak data, the inclusion of which might degrade the quality of the resulting model, the quality indicators (R_{meas}, $CC_{1/2}$) are widely used to determine the resolution cut-off.

After scaling, the space group is determined. It cannot be derived from the lattice type as it depends on symmetry operators within the unit cell. If reflections have been merged that are related by crystallographic symmetry operators the merging R-factor is low, while merging of reflections that are not truly symmetry related causes high R-factors, even at low resolution.

Plotting the mean intensity against the resolution expressed as $\sin^2\theta/\lambda$, yields a characteristic curve (Wilson plot) where the intensity decreases with higher resolution. Solvent effects cause a minimum at ~ 5 Å, and a maximum at ~ 4-3.5 Å is caused by the length of interatomic distances in proteins. At resolutions higher than 3.5 Å the intensity falls linearly and the slope of a linear regression of this region determines the Wilson B-factor [101]. It represents the decrease of intensity in diffraction due to thermal vibration and static crystal disorder.

Experimental Procedure

The diffraction capabilities of the crystals were tested first at an in house X-ray system equipped with the X-ray generator MicroMax-007HF (Rigaku) and a MAR345 dtb image plate detector at CuKα-radiation (λ=1.5418 Å). Data sets were collected at the PXIII beamline at the Swiss Light Source (Paul Scherrer Institute, Villigen, Switzerland) with a PILATUS (Pixel Apparatus for the SLS) detector and a wavelength of 1 Å.

For phasing of T1L σ1(29-159) via single-wavelength anomalous diffraction (SAD), one 360°-data set at a wavelength of 1 Å and eight 720°-data sets at a wavelength of 2 Å were collected from one iodide-containing crystal. The χ-angle was increased by 5° from one dataset to the other to obtain highly redundant and complete diffraction data. Data sets were indexed, integrated and scaled using XDS [102].

3.10.3 Structure Determination and Refinement

Background

The intensity and the phase of a reflection (h,k,l) are dependent on the electron distribution of the unit cell content. Each scattered X-ray beam that leads to a reflection (h,k,l) can be described as a structure factor F_{hkl} containing its amplitude $|F_{hkl}|$ and phase φ_{hkl}. The structure factor F_{hkl} is a complex number and can be expressed as a vector in the Gaussian plane (equation 3.4) with the length and angle corresponding to the amplitude and phase, respectively.

$$\mathrm{F_{hkl}} = |F_{hkl}| \cdot (\cos\varphi_{hkl} + \mathrm{i}\sin\varphi_{hkl}) = |F_{hkl}| \exp(\mathrm{i}\varphi_{hkl}) \qquad \textbf{(3.4)}$$

The amplitudes and the phases of the scattered beams are linked to the scattering matter of the unit cell by a Fourier transformation, with the sum over all atoms n, the atomic scattering factor f_n of atom n and its position in the dimensions x, y and z.

$$\mathrm{F_{hkl}} = \sum_{n=1}^{N} f_n \cdot \exp[2\pi\mathrm{i}(\mathrm{h}x_n + \mathrm{k}y_n + \mathrm{l}z_n)] \qquad \textbf{(3.5)}$$

Both phase and amplitude of each scattered wave contain information about all atoms in the unit cell. By determining the amplitude and phase for each F_{hkl} and applying the Fourier transformation one can calculate electron density that allows to determine the structure. The structure factor amplitudes can be determined from the diffraction data via the intensity I_{hkl}. The intensity of a reflection is proportional to the square of the structure factor amplitude. However, the phases cannot be measured directly from the diffraction experiment. To overcome the so called phase problem different indirect methods have been developed such as molecular replacement (MR), single or multiple isomorphous replacement (SIR/MIR), SAD or multiple-wavelength anomalous dispersion (MAD). In this thesis, SAD and MR were used for structure determination.

Molecular Replacement

If a structurally similar model to the protein of interest is available, molecular replacement can be successfully performed. To obtain phases, the search model is first rotated and then translated in space to place it in the (new) asymmetric unit so that it fits the target structure.

The Matthews coefficient V_M gives an estimate on how many copies n of the molecule are contained in the asymmetric unit and should be placed [103]. Proteins have a relatively uniform density, and protein crystals contain usually a high solvent content of about ~ 20-70%. Thus, the coefficient V_M is usually in the range of 1.75-4.2 Å^3/Da and is calculated from the volume of the unit cell $V_{unit\ cell}$, the molecular weight of the molecule M_w and the number of asymmetric units in the unit cell n_{ASU} (equation 3.6).

$$V_M = \frac{V_{unit\ cell}}{Mw \cdot n_{ASU} \cdot n} \quad \textbf{(3.6)}$$

The rotation and translation of the search model are independently performed in Patterson space. The Patterson function is the Fourier transform of $|F_{hkl}|^2$ and the calculated map is equivalent to the convolution of the electron density with itself. The Patterson space of N atoms contains all N(N-1) interatomic distance vectors. The vectors are independent from the phases of scattered X-rays, can also be calculated from an existing atomic model and are very similar between closely-related structures.

The Patterson function of the experimental data as well as of the search model are calculated. The rotation of the search model around all three axes results in a peak within the rotation function if the orientation of the Patterson maps correlate. The rotation function considers only intramolecular distance vectors as they are independent from translation.

During the translation search, only intermolecular distances (which can be distinguished from the intramolecular vectors by their longer length) are taken into consideration and the model is translated along the three axes. The translation function features a peak for the correct translation vector.

Initial phases derived from the search model together with the structure factor amplitudes from the diffraction experiment can be used to calculate an initial electron density map (equation 3.7). The electron density ρ at a position in the unit cell xyz is calculated using the unit cell volume V and the structure factors F_{hkl}.

$$\rho_{xyz} = \frac{1}{V} \sum_{hkl} F_{hkl} \cdot \exp[-2\pi i(hx_n + ky_n + lz_n)] \quad \textbf{(3.7)}$$

Single-wavelength Anomalous Diffraction

A different approach to derive phases exploits the phenomenon of anomalous diffraction of heavy atoms that are intrinsically present in the protein or have been added. The atomic scattering factor f_n is dependent on the electron distribution of an atom and contains the normal scattering term f_0 (dependent on the Bragg angle) and the anomalous scattering factors f' (dispersive term) and f'' (absorption term), which are dependent on the wavelength (equation 3.8).

$$f_n(\theta,\lambda) = f_0(\theta) + f'(\lambda) + if''(\lambda) \qquad \textbf{(3.8)}$$

X-ray absorption occurs near an absorption edge when the X-ray energy is sufficiently high to promote an inner electron of the atom. Most elements with a Z > 18 have an (K- or L-) absorption edge that lies in an X-ray energy range that most synchrotrons can provide, or have (at least) an absorption edge above available wavelengths to yield an anomalous signal. Anomalous scattering occurs with a phase shift of 90° in term f'' relative to the normal scattering of the atom. This generates anomalous differences between the two structure factors of a Friedel pair (and for structure factors of a Bijovoet pair) that causes the Friedel law ($|F_{hkl}|=|F_{-h-k-l}|$) to break (Figure 3.2). The anomalous differences can be obtained and used to locate the positions of the anomalous scatterer.

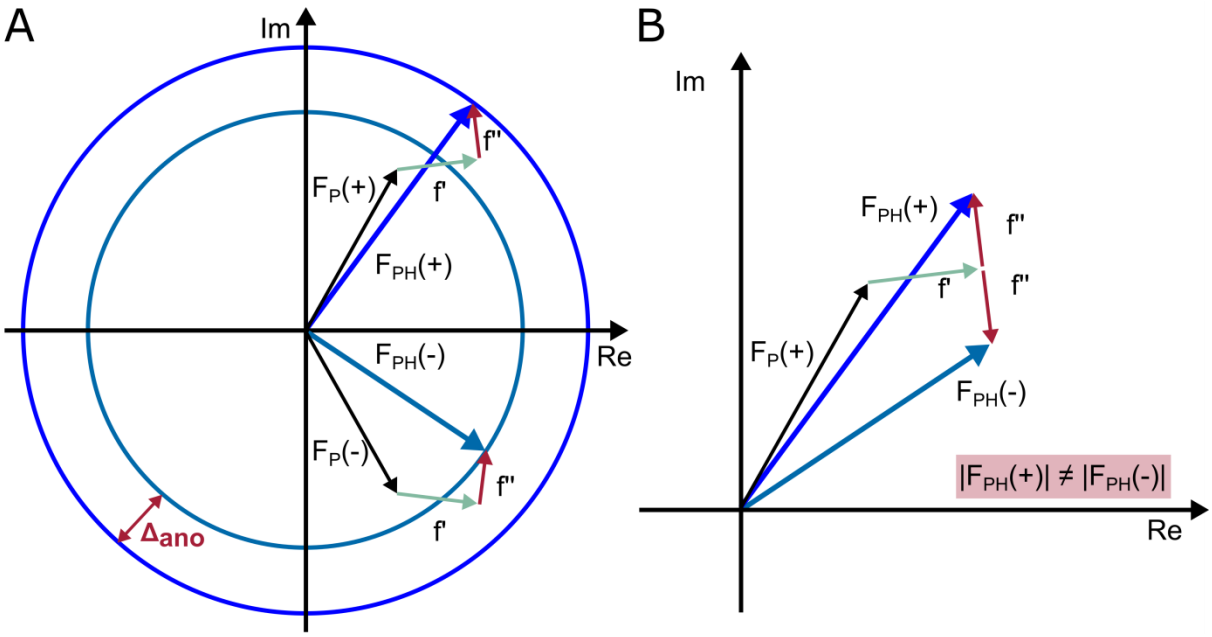

Figure 3.2 Breakdown of Friedel's law. (A) The anomalous scattering effect causes Friedel's law to break down, meaning $|F_{hkl}|\neq|F_{-h-k-l}|$ or $|F_{PH}(+)|\neq|F_{PH}(-)|$.

In a SAD experiment, usually all diffraction data are collected from a single crystal containing an anomalous scatterer, and thus nonisomorphism is not a problem in this phasing strategy. The measurement is performed at one wavelength (which generates the maximum anomalous f'' signal possible) and only provides the anomalous differences ($\Delta_{ano} = F^{\pm} = |F_{PH}(+)| - |F_{PH}(-)|$). These differences are used to estimate the heavy atom contribution to the scattering, and then direct or Patterson methods are used to obtain the positions of the heavy atom substructure. The amplitude and phase of the substructure can be calculated, but α phase ambiguity remains in the phase of the protein structure factor, and resolving this requires the use of density modification.

Structure Refinement

Structural refinement is an iterative process in which the atom coordinates and temperature factors are improved to obtain a better correlation between the built model and the experimental data. The refinement process is monitored by calculating crystallographic R-factors with the observed (F_{obs}) and calculated (F_{calc}) structure factor amplitudes.

$$R = \frac{\sum_{hkl} |F_{obs}(\mathrm{hkl}) - F_{calc}(\mathrm{hkl})|}{\sum_{hkl} F_{obs}(hkl)} \qquad \textbf{(3.9)}$$

For a perfect agreement R would be 0 and for a random structure model it is near 0.59. As this factor can be made arbitrary low by introducing more adjustable variables (overfitting), the unbiased R-factor R_{free} was introduced to assess model and refinement quality [104]. A small subset of reflections (5-10%) is flagged as "free" and is not used during refinement. The larger ("working") set of reflections is then referred to R_{work}. The R_{free} value is an unbiased estimate of the improvement of the structure model and is usually higher than R_{work}.

Experimental Procedure

To obtain phase information via SAD, the program autoSHARP [105] was used in case of T1L σ1(29-159). The program Phaser [106] of the CCP4 package [107] was used for solving the phase problem via molecular replacement. The used search models are listed below:

Construct	Search model	Source
$(GCN4)_3$-T1L σ1(29-159)	- residues 29-76 of $(GCN4)_3$-T1L σ1(29-76)-$(GCN4)_3$	provided by K. Reiss
T3D σ1(25-291)	- residues 170-265 of T3D σ1(170-455)	PDB ID: 3S6X
	- T1L σ1(29-159)*	this work
T3D σ1(1-168)	- residues 27-168 of T3D σ1(25-291)	this work
T1L σ1-5C6Fabs	- residues 308-470 of T1L σ1(265-470)	PDB ID 4GU3
	- Fab of IgG2a(κ) 9BG5	this work
T3D σ1-9BG5Fabs	- T3D σ1(293-455)	PDB ID 2OJ5
	- IgG1(κ) Fab	PDB ID 1FIG

* modified with the CCP4 program chainsaw using a T1L-T3D σ1 sequence alignment

Alternating model building and refinement cycles were performed. Model building was done using Coot, and structural refinement was performed with the programs REFMAC5 [108], autoBuster [109] or phenix [110].

4 Results

4.1 T1L σ1 Fragments

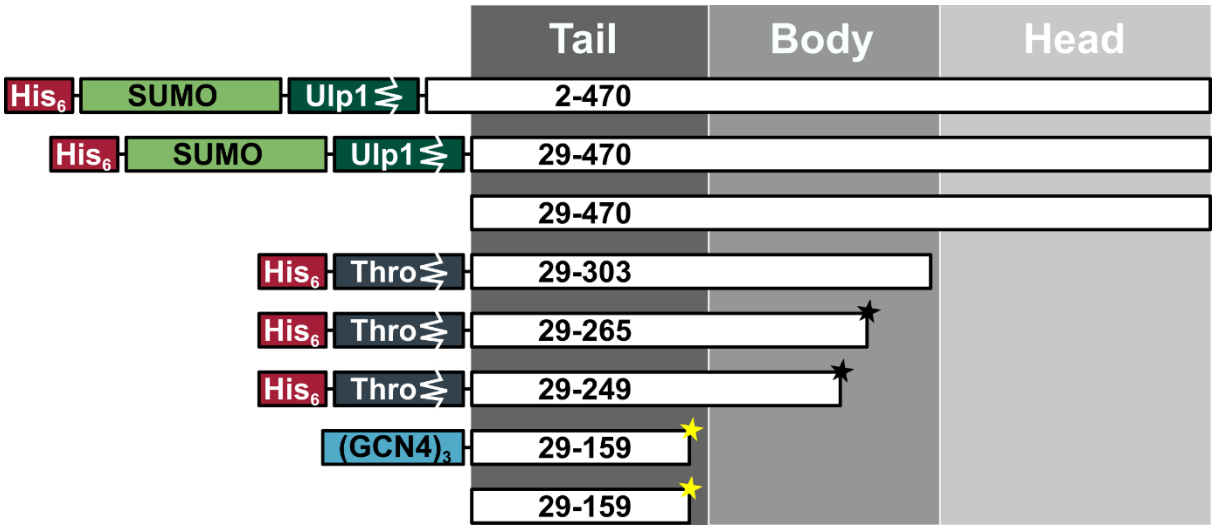

Figure 4.1 Overview of T1L σ1 constructs. White boxes of varied length according to the number of amino acids and domains that are covered by the σ1 fragments. The three constructs comprising the σ1 tail, body, and head domain are discussed in sections 4.1.1 and 4.1.2, the three constructs comprising the tail and parts of the body domain are discussed in section 4.1.3, and the two constructs comprising only the tail domain are discussed in section 4.1.4. His_6-tag is shown as red, SUMO-tag as green, and the $(GCN4)_3$-motif as a blue box. Ulp1 and thrombin (Thro) cleavage sites are indicated. Constructs that led to a crystal structure are marked with a yellow star. Diffraction data is available for constructs marked with a black star, but the structure is currently not solved.

4.1.1 His_6-SUMO-T1L σ1(2-470 and 29-470)

The T1L σ1 constructs comprising amino acids 2-470 and 29-470 were cloned via BsaI and XbaI restriction enzyme sites into the pE-SUMOpro vector. Both proteins were produced at 20°C and 37°C after IPTG induction, indicated by the appearance of bands in an SDS-PAGE gel that correspond to the molecular weights of the proteins (Figure 4.2). Test Ni-affinity chromatography with single-use spin columns revealed that both proteins bind to the column and elute at the highest imidazole concentration used.

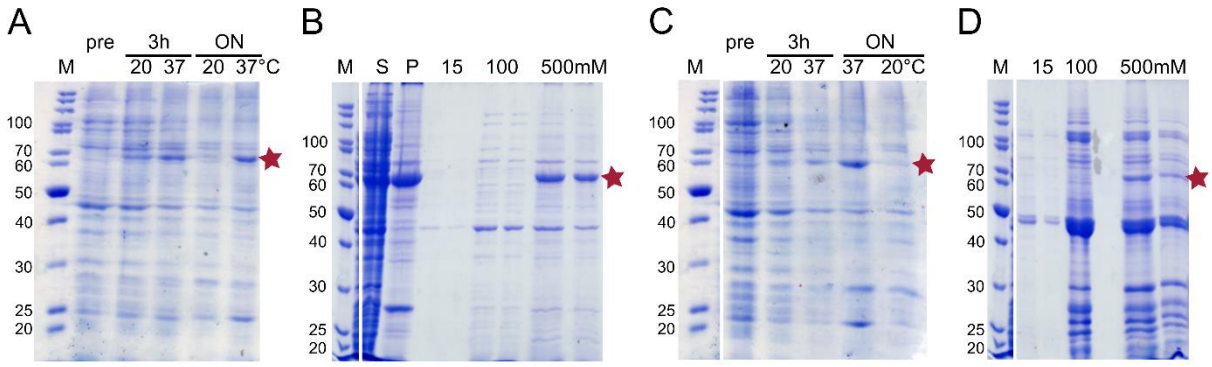

Figure 4.2 Test expression and spin-trap test. (A) His_6-SUMO-T1L σ1(2-470). SDS-PAGE gel of the test expression performed at 20 and 37°C. In comparison to the sample taken pre-induction (pre) with IPTG, a band appears at ~64 kDa that corresponds to the molecular weight of the target protein. **(B)** His_6-SUMO-T1L σ1(2-470). SDS-PAGE gel of the test Ni-affinity chromatography. The soluble (S) and the pellet (P) fraction after lysis show a thick band at ~64 kDa. Elution with 15 and 100 mM imidazole removed some non-specifically bound proteins. The protein of interest and other proteins eluted with 500 mM imidazole. **(C)** His_6-SUMO-T1L σ1(29-470). SDS-PAGE gel of the test expression performed at 20 and 37°C. In comparison to the sample taken pre-induction (pre) with IPTG a band appears at ~61 kDa that corresponds to the molecular weight of the protein. **(D)** His_6-SUMO-T1L σ1(29-470). SDS-PAGE gel of the test Ni-affinity chromatography. Elution with 15 and 100 mM imidazole removed some non-specific bound proteins. A band at ~61 kDa is present at elution with 500 mM imidazole. Most impurities that are present in the eluate with 500 mM imidazole are also present at elution with 100 mM imidazole.

4.1.2 T1L σ1(29-470)

The T1L σ1 construct, comprising amino acids 29-470, was cloned via NcoI and BamHI restriction enzyme sites into plasmid pET16b. The protein is untagged and, as revealed by lysis tests, soluble in pH 8.5 buffered solutions (Figure 4.3). Anion exchange chromatography was used as the first purification step. Impurities bound stronger to the column than did T1L σ1. Therefore, the flow through was collected, and the eluate was discarded. Three consecutive chromatographic separations were performed.

Ammonium sulfate precipitation was used next to remove contaminating proteins. T1L σ1 precipitated at a concentration of ~ 12% ammonium sulfate. The precipitated protein pellet was dialyzed into a buffer containing 25 mM HEPES pH 8.5. The protein of interest partially bound to a cation exchange chromatography column and could be eluted using three different conditions. The first species eluted when the buffer was changed from 25 mM to 40 mM HEPES, the second species at a concentration of ~ 5 mM NaCl (40 mM HEPES), and the third species at ~ 250 mM NaCl (40 mM HEPES). SEC of protein samples obtained from the three different elution conditions resulted in single peaks corresponding to the void volume of the column.

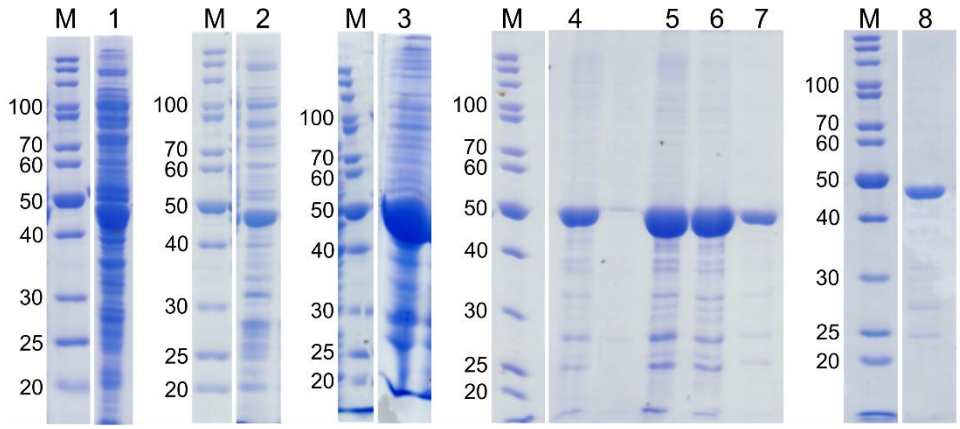

Figure 4.3 Purification of T1L σ1(29-470). SDS-PAGE gels of the different purification steps are shown. Bands at ~ 48 kDa correspond to the molecular weight of the protein. Marker (M), soluble fraction after lysis (1), collected flowthrough after the third application on an AEC column (2), dissolved precipitated protein obtained by addition of 12%-ammonium sulfate (3), flowthrough of the cation exchange chromatography (4) elution through buffer change from 25 to 40 mM HEPES pH 8.5 (5,6) and elution with 5 mM NaCl (7) in buffer A. Protein after SEC (8).

To determine if the protein was properly folded or aggregated, dynamic light scattering (DLS) measurements were performed (Figure 4.4). Several fractions showed a monodispersed peak corresponding to a mean hydrodynamic radius of 52 ± 10 nm.
Electron micrographs that were obtained using a scanning transmission electron microscope (performed by York Stierhof, ZMBP Tübingen, Germany) showed that samples that had been diluted in PBS during sample preparation are completely aggregated, while samples diluted in SEC buffer were more homogenous, with fewer aggregates and filamentous structures.

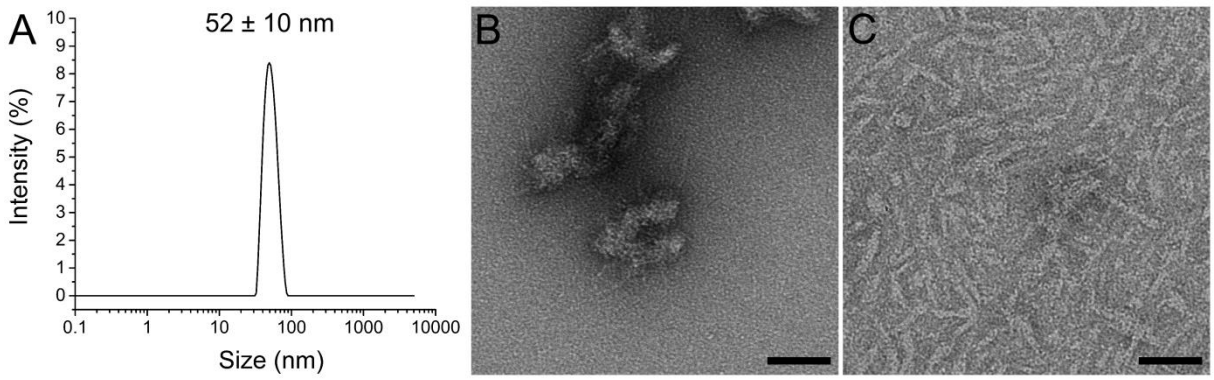

Figure 4.4 DLS measurement and electron micrographs of T1L σ1(29-470) after size exclusion chromatography. (A) DLS measurement revealed a single monodisperse peak by intensity of a mean size of 52 ± 10 nm. This species contributed to the overall mass and intensity to 100%. **(B)** Electron micrograph of purified T1L σ1(29-470) diluted in PBS (pH 7.4) shows an inhomogeneous sample of aggregated protein. The black bar corresponds to 50 nm. **(C)** Electron micrograph of purified T1L σ1(29-470) diluted in SEC buffer (pH 8.6) shows a more homogenous sample. The black bar corresponds to 50 nm.

Crystallization trials were performed, and a few crystallization hits with spherulites, tiny needles, or needle clusters were obtained. These crystals could not be optimized for structure determination.

4.1.3 Coiled Coil – Body Constructs of T1L σ1

The T1L σ1 constructs comprising amino acids 29-303, 29-265, and 29-249 were generated by introducing a stop codon into pET28b::His_6-T1L σ1(29-470) at the corresponding C-terminal positions via site-directed mutagenesis.

All three proteins were produced after induction with 0.2 mM IPTG at 20°C. The proteins were eluted from a Ni-affinity chromatography column with 250 mM imidazole after a washing step with 75 mM imidazole. Both thrombin and trypsin digestion removed the His_6-tag from the T1L σ1 proteins. Cleavage with trypsin was preferentially used for tag-removal in solution. On-column digestion did not result in cleaved protein.

After buffer optimization, minor aggregation peaks on size exclusion chromatograms were observed for T1L σ1 (29-303) and T1L σ1 (29-249) with a SEC buffer at pH 8.6 and for T1L σ1 (29-265) with a SEC buffer at pH 7.6 (Figure 4.5). The concentration of the proteins was adjusted with a precipitation test after SEC.

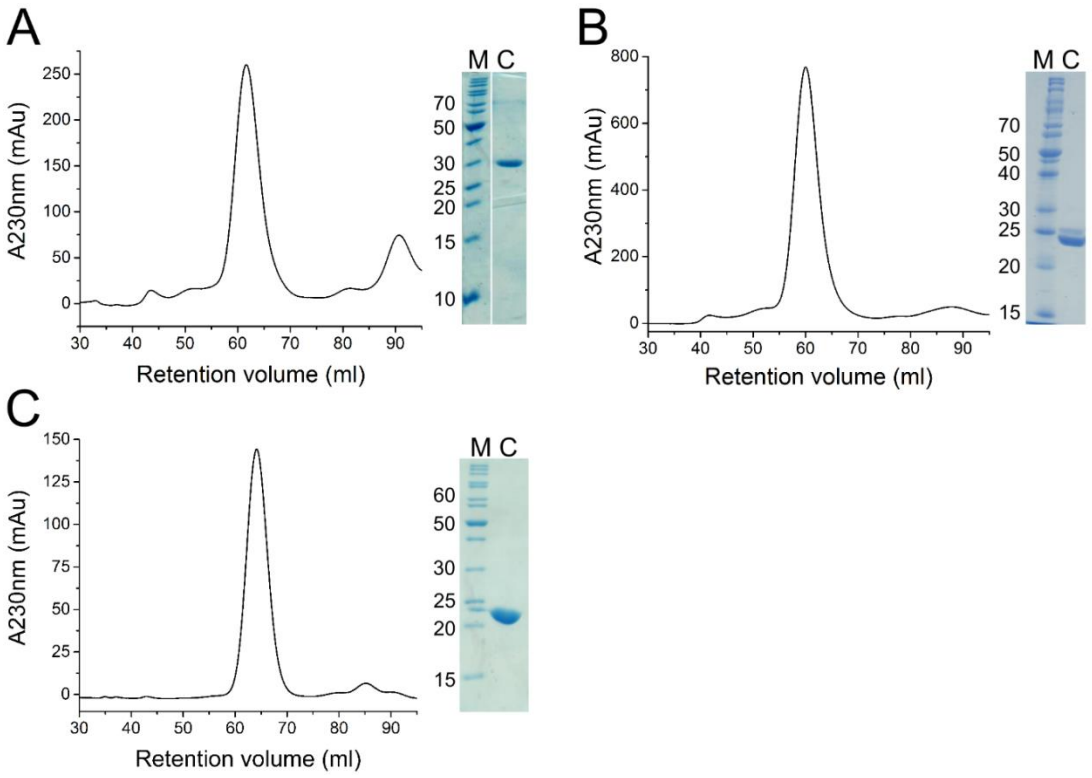

Figure 4.5 Purification of T1L σ1(cc-body) constructs. Size exclusion chromatogram with the absorbance measured at 230 nm of **(A)** T1L σ1(29-303), **(B)** T1L σ1(29-265), and **(C)** T1L σ1(29-249).

SDS-PAGE gels of the concentrated protein samples are included. Bands at ~ 30 kDa **(A)**, ~ 26 kDa **(B)**, ~ 24 kDa **(C)** correspond to the molecular weights of the proteins.

Crystals were obtained for all three proteins by the vapor diffusion method (Figure 4.6). T1L σ1(29-303) yielded thin needles or needle clusters. Fine screening and optimization trials using micro seeds or the additive screen did not improve the crystal shape or the diffraction properties.

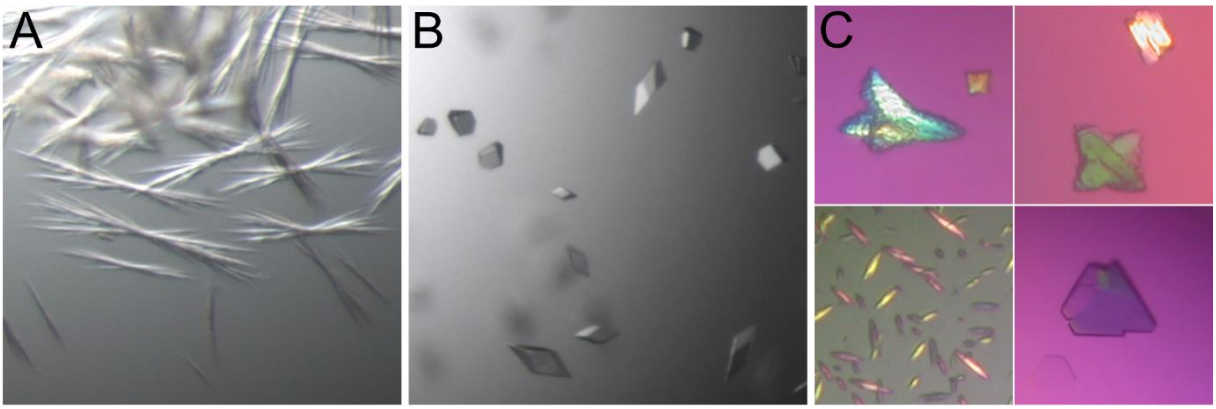

Figure 4.6 Crystallization of T1L σ1(cc-body) constructs. Crystals of **(A)** T1L σ1(29-303) in 0.1 M sodium formate, 12% PEG3350, **(B)** T1L σ1(29-265) in 25% (v/v) ethylene glycol, and **(C)** T1L σ1(29-249) in 20% (w/v) PEG 2000MME, 0.1 M Tris pH 8.5, 0.2 M TMNO (upper left), 2% (v/v) Tascimate pH 8.0, 0.1 M Tris pH 8.5, 16% PEG3350 (upper right), 0.1 M HEPES pH 7.0, 30% (v/v) Jeffamine ED-2001 (lower left), 10% isopropanol, 0.1 M MES pH 6.0, 0.2 M calcium acetate (lower right) are shown.

Initial T1L σ1(29-265) crystals grew in 25% ethylene glycol at 20°C. The crystals dissolved in higher ethylene glycol concentrations, thus mother liquor was used as cryoprotectant, but led to minor ice rings on the detector. The crystals diffracted up to 2.8 Å resolution at the PXIII beamline (SLS, Villigen, Switzerland) (Table 4.1). No pseudo-translation symmetry was detected by Xtriage (Phenix, [110]) or Sfcheck (CCP4). Molecular replacement attempts to solve the phase problem are ongoing.

Table 4.1 Data collection statistics of T1L σ1(29-265)

Data collection	**T1L σ1(29-265)**
Resolution range [Å]	47.9-2.8 (2.87-2.80)
Space group	R32
Unit cell dimensions [Å]	101.0, 101.0, 456.5
Unit cell angles [°]	90 90 120
Completeness [%]	95.1 (96.4)
Total reflections	94204 (6478)
Unique reflections	21626 (1595)
R_{meas} [%]	13.6 (67.5)
$CC_{1/2}$ [%]	99.9 (91.2)
I/σ	7.35 (1.36)

Wilson B [Å^2]	57.6

Values in parentheses are for the highest-resolution shell.

T1L σ1(29-249) crystallized in several different conditions with different sizes and shapes. So far, one of those conditions (10% isopropanol, 0.1 M MES pH 6.0, 0.2 M calcium acetate) was optimized and the crystals diffracted to a resolution of about 2.0 Å at the PXIII beamline (SLS, Villigen, Switzerland). Due to one very long unit cell axis, data were collected with a detector resolution of 3-3.5 Å to ensure the separation of the diffraction spots. The space group could not be determined with confidence, and the data possess a high degree of pseudo-translation symmetry. Molecular replacement (Phaser, CCP4) with the structure or fragments of T1L σ1(29-159) has not lead to a reliable solution thus far.

4.1.4 Coiled Coil Constructs of T1L σ1

$(GCN4)_3$-T1L σ1(29-159) – Purification and Crystallization

The plasmid pIBA-GCN4tri::T1L σ1(29-159) was obtained from Dr. Kerstin Reiss. In this construct, the T1L σ1 sequence is in frame with the heptad repeat pattern of $(GCN4)_3$. A stop codon is present at the end of the σ1 sequence, so that the produced protein solely carries the N-terminal $(GCN4)_3$-motif, while the C-terminal $(GCN4)_3$ and the His_6-tag are absent.

The protein was produced at 37°C after induction with 0.2 µg/ml AHTC for 5 h and was purified after refolding from inclusion bodies. The protein eluted from an anion exchange chromatography column with a concentration of ~ 250 mM NaCl. Size exclusion chromatography was used as a last purification step (Figure 4.7), and the protein was concentrated to 6-6.5 mg/ml for crystallization.

Crystals of $(GCN4)_3$-T1L σ1 were obtained with the hanging drop vapor diffusion method in 10% PEG8000, 0.1 M imidazole pH 8.0, 0.2 M calcium acetate at 20°C (Figure 4.7). Crystals were flash frozen with mother liquor containing 22% MPD as cryoprotectant, and X-ray diffraction data extending to 1.8 Å resolution was collected and used for structure determination. At this resolution, the R-factors of the structure (R_{work}/R_{free}: 23.9/ 27.4%) are relatively high, a consequence of the presence of pseudo-translation symmetry that was estimated to be ~ 18% using Xtriage (Phenix, [110]).

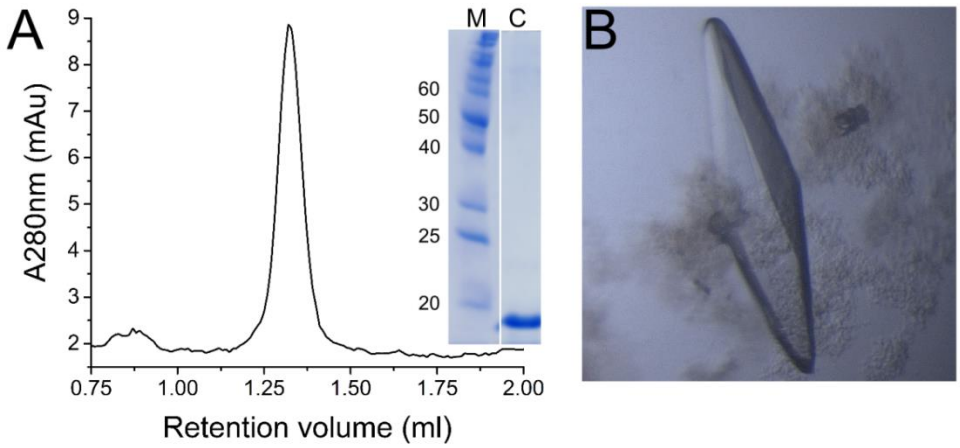

Figure 4.7 Purification and crystallization of $(GCN4)_3$-T1L σ1. (A) Analytical size exclusion chromatogram of $(GCN4)_3$-T1L σ1. The absorbance is shown at 280 nm. The SDS-PAGE gel of the concentrated protein is included. A band at ~ 18 kDa corresponds to the molecular weight of a monomer. **(B)** Crystal of $(GCN4)_3$-T1L σ1 in 10% PEG8000, 0.1 M imidazole pH 8.0, 0.2 M calcium acetate.

$(GCN4)_3$-T1L σ1(29-159) – Crystal Structure

The structure was solved in the space group $P2_1$ with one σ1 trimer in the asymmetric unit (Table 4.2). With the exception of the first N-terminal and the last C-terminal residue in chain A, all amino acids of the protein are defined in the electron density. The protein forms an uninterrupted parallel α-helical coiled coil of ~ 230 Å in length. Within the crystal, the protein is tightly packed with a solvent content of only ~ 34%. Layers of slightly shifted coiled coils that point in one direction are surrounded by layers of coiled coils pointing in the opposite direction. Crystal contacts include several charge-mediated interactions between adjacent α-helical bundles.

Table 4.2 Data collection and refinement statistics of $(GCN4)_3$-T1L σ1

Data collection	**$(GCN4)_3$-T1L σ1**
Resolution range [Å]	43.9-1.82 (1.87-1.82)
Space group	$P2_1$
Unit cell dimensions [Å]	65.3 35.6 89.3
Unit cell angles [°]	90.0 108.4 90.0
Completeness [%]	97.5 (96.3)
Total reflections	234707 (16860)
Unique reflections	34717 (2533)
R_{meas} [%]	8.2 (90.2)
$CC_{1/2}$ [%]	100 (84.3)
I/σ	15.6 (2.6)
Wilson B [$Å^2$]	30.9

Refinement	
R_{work}/ R_{free} [%]	23.9/ 27.4
Atoms	
Protein	3461
Waters	161
Cl^-	2
Imidazole	2
B factors [Å^2]	
Chain A	28.0
Chain B	27.7
Chain C	26.8
Water	30.2
Cl^-	20.8
Imidazole	29.0
r.m.s.d. bond lengths [Å]	0.01
r.m.s.d. bond angles [°]	0.98

Values in parentheses are for the highest-resolution shell.

The protein consists of 22.5 heptad repeats; 4 are formed by the $(GCN4)_3$ and 18.5 by the σ1 segment. The amino acids at positions *a* and *d* of a heptad repeat form the hydrophobic core of the coiled coil. Nine interhelical salt bridges, mostly formed between amino acids at position *g* and *e*, stabilize the coiled coil structure. Seven salt bridges belong to the σ1 segment and are distributed over the entire length of the σ1 molecule. Few hydrophilic amino acids are located at typical hydrophobic positions *a* and *d*. N38 and N94 occupy *d* positions and bind chloride ions inside the core (Figure 4.8). The B-factors of the chloride ions and the surrounding amino acids are similar, indicating full occupancy of the ions (N38: 20-27 Å^2, Cl^-: 24 Å^2, and N94: 17-19 Å^2, Cl^-: 17 Å^2).

A stutter is located close to the C-terminal end of the protein. This formal insertion of four amino acids (here: VTTE; 147-150) into the heptad repeat leads to a local unwinding of the α-helices and the coiled coil. The residue E150 at the *d* position is shifted outside of the core and forms a *da*-layer with V151. The C_β and C_γ atoms of E150 contribute to the hydrophobic interaction with V151, while the carboxyl group forms a charge-mediated interaction with R153, which also forms a salt bridge with D155 from an adjacent subunit.

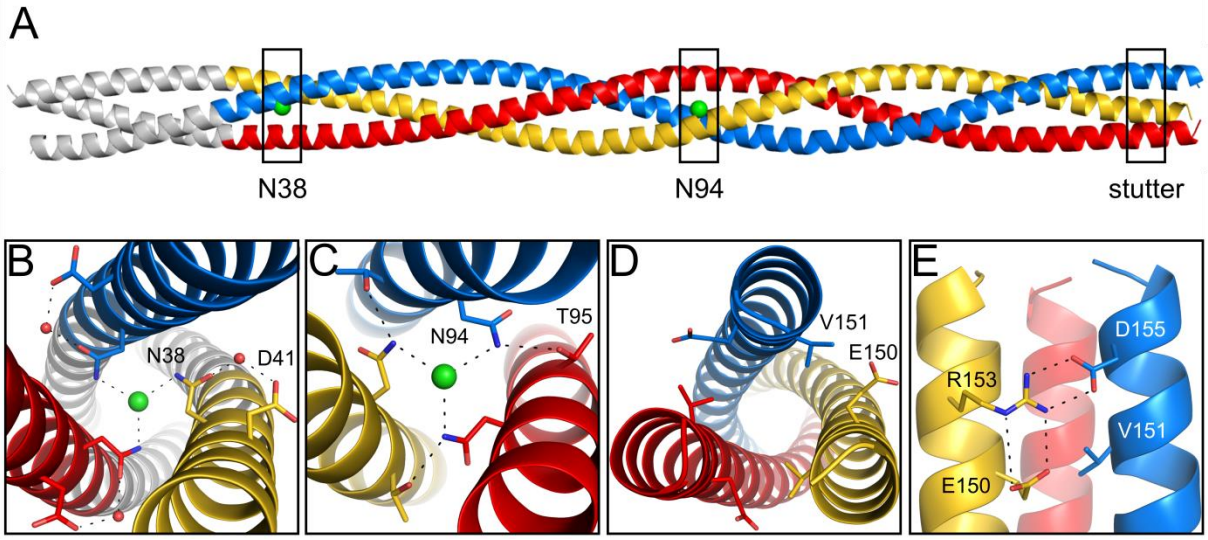

Figure 4.8 Crystal structure of $(GCN4)_3$-T1L σ1(29-159). (A) The protein forms a trimeric parallel α-helical coiled coil that has two chloride ions bound within the core. The part of the structure belonging to $(GCN4)_3$ is colored grey, and the part belonging to σ1 is colored in blue, red, and yellow. Chloride ions are colored green **(B, C)** Close-up views of the bound chloride ions complexed by N38 and N94, respectively. View along the threefold axis of the molecule. **(D)** Close-up of the stutter, viewed along the threefold axis. E150 is shifted outward of the core and forms a *da*-layer with V151. **(E)** E150 also interacts with R153 that additionally forms an interhelical saltbridge with D155.

T1L σ1(29-159) – Purification and Crystallization

To verify that the σ1 tail domain independently forms a stable, trimeric coiled coil, a construct without the trimerization motif $(GCN4)_3$ was designed and cloned into pET16b using the NcoI and BamHI restriction sites. The protein contains residues 29-159 and two additional amino acids (Met and Ala) at the N-terminus due to the cloning procedure. The protein was produced after induction with 0.3 mM IPTG at 25°C overnight and purified via anion exchange chromatography followed by size exclusion chromatography (Figure 4.9). The protein elutes early, at a retention volume that corresponds to a globular protein of ~ 100 kDa. This finding indicates that the protein exhibits a trimeric, elongated structure similar to $(GCN4)_3$-T1L σ1(29-159). Circular dichroism (CD) spectra of the purified protein show that the molecule is folded and α-helical at a broad range of pH values (pH 1-9). Temperature-dependent CD-measurements from 10 to 95°C revealed a melting curve with a sharp transition from folded to random coil at 70°C (Rebecca Ebenhoch, Bachelor Thesis, 2014).

For crystallization, a PEG-precipitation test was performed to adjust the protein concentration. Well diffracting crystals were obtained in 20% PEG8000, 0.1 M CAPS pH 10.5, 0.2 M NaCl at 4°C (Figure 4.9). Molecular replacement attempts with the

complete or partial σ1 segment of the $(GCN4)_3$-T1L σ1(29-159) structure as a search model were not successful.

Experimental phases were obtained using single-wavelength anomalous diffraction (SAD; Table 4.3). For this purpose, the protein was denatured and refolded in an iodide-containing buffer to exchange the bound chloride ions of the coiled coil core. The refolded protein was analyzed by circular dichroism. The CD-spectra was similar to an untreated protein sample. Crystals were obtained in 18% PEG8000, 0.1 M CAPS pH 9.5, 0.2 mM NaI by seeding with crystals from the original crystallization condition at 4°C.

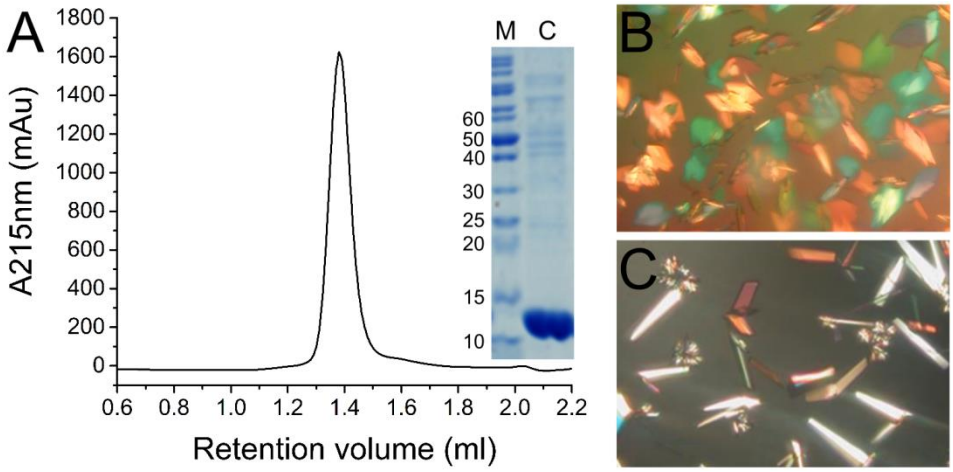

Figure 4.9 Purification and crystallization of T1L σ1(29-159). (A) Analytical size exclusion chromatogram of T1L σ1(29-159). The absorbance is shown at 215 nm. An SDS-PAGE gel showing the concentrated protein is included. A band at ~14 kDa corresponds to the molecular weight of a monomer. **(B)** Crystals of T1L σ1(29-159) in 20% PEG8000, 0.1 M CAPS pH 10.5, 0.2 M NaCl. **(C)** Crystals of refolded T1L σ1(29-159) grown in 18% PEG8000, 0.1 M CAPS pH 9.5, 0.2 M NaI.

T1L σ1(29-159) – Crystal Structure

The crystals belong to space group $P2_1$ and contain one trimeric σ1 molecule in the asymmetric unit. All residues except of the last C-terminal amino acid of σ1 are defined in the electron density.

The protein folds into a parallel, trimeric α-helical coiled coil of ~ 190 Å in length. Similar to $(GCN4)_3$-T1L σ1(29-158), the σ1 structure is stabilized by seven interhelical salt bridges. It is composed of 18.5 heptads and two halogenide ions that are bound by asparagine residues 38 and 94 inside the core of the molecule. However, the main chain atoms of the identical parts of the two structures superimpose with a high r.m.s.d. value of 2.5 Å (Figure 4.10, see Table 5.1 at page 73). Alignments of main chain atoms between individual chains have r.m.s.d. values of 1.54-1.82 Å.

Table 4.3 Data collection and refinement statistics of T1L σ1(29-159)

Data collection	**Native**	**Refolded**	**Refolded**
Wavelength [Å]	0.91841	1.0000	2.0000
Resolution range [Å]	41.7-1.43 (1.52-1.43)	48.7-1.35 (1.39-1.35)	48.7-2.4 (2.46-2.40)
Space group	$P2_1$	$P2_1$	$P2_1$
Unit cell dimensions [Å]	53.4, 37.2, 94.9	52.7, 37.6, 89.7	52.7, 37.6, 89.7
Unit cell angles [°]	90.0, 102.6, 90.0	90.0, 100.5, 90.0	90.0, 100.5, 90.0
Completeness [%]	99.3 (96.1)	100 (100)	100 (100)
Total reflections	445146 (63117)	503646 (33260)	1039304 (18914)
Unique reflections	67304 (10401)	76273 (5563)	25687 (1566)
Redundancy	6.6 (6.1)	6.6 (6.0)	40.5 (12.1)
R_{meas} [%]	12.3 (71.4)	10.9 (87.6)	7 (14.4)
$CC_{1/2}$ [%]	100 (96)	100 (72)	100 (99)
I/σ	11.0 (2.1)	12.0 (1.9)	50.1 (12.9)
Wilson B [$Å^2$]	19.2	16.2	13.5
Anomalous Signal [%]			4.5 (1.4)
Refinement			
R_{work}/ R_{free} [%]	19.3/ 23.0		
Atoms			
Protein	3032		
Waters	688		
Chloride	2		
B factors [$Å^2$]			
Chain A	19.0		
Chain B	19.9		
Chain C	18.1		
Water	33.0		
Chloride	15.0		
r.m.s.d. bond lengths [Å]	0.01		
r.m.s.d. bond angles [°]	0.89		

Values in parentheses are for the highest-resolution shell.

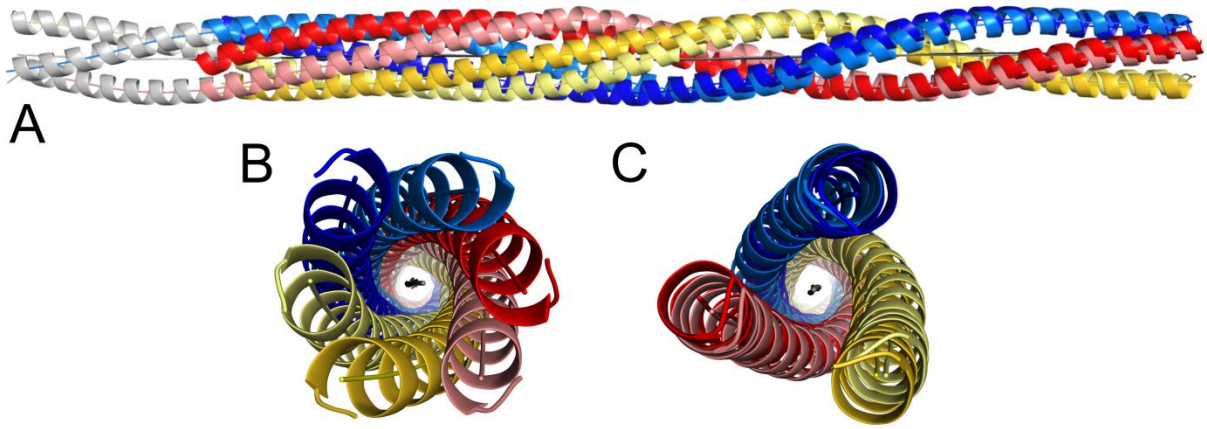

Figure 4.10 Superposition of the T1L σ1(29-159) and $(GCN4)_3$-T1L σ1(29-159) structure. (A) The identical parts (residues 29-158 of σ1) of two structures are aligned via their coiled coil axis generated by the program twister [111]. The GCN4-segment is colored in grey, and σ1 is colored in blue, red, and yellow. Coiled coil axes are shown in grey, and α-helical axes are shown in the color of the according σ1 chains. The two coiled coil molecules differ in their twist. **(B,C)** Close up view along the coiled coil axis. While the three chains of the helical-bundles are properly aligned on the C-terminal part **(C)**, the chains disperse at the N-terminal part of the molecules **(B)**.

The local coiled coil geometry of the two structures was analyzed with the program twister [111] (Figure 4.11). The stutter of T1L σ1 (VTTE; 147-150) located close to the C-terminal end of the solved σ1 tail domain was identified and found to be compensated by a local unwinding of the coiled coil and the α-helices. The unwinding of the coiled coil is detected by a local increase of the coiled coil pitch (the distance of one full turn of the superhelix) that is accompanied by a local increase of the coiled coil phase yield per residue. A minor decrease in the α-helical phase yield per residue indicates the local unwinding of the α-helices.

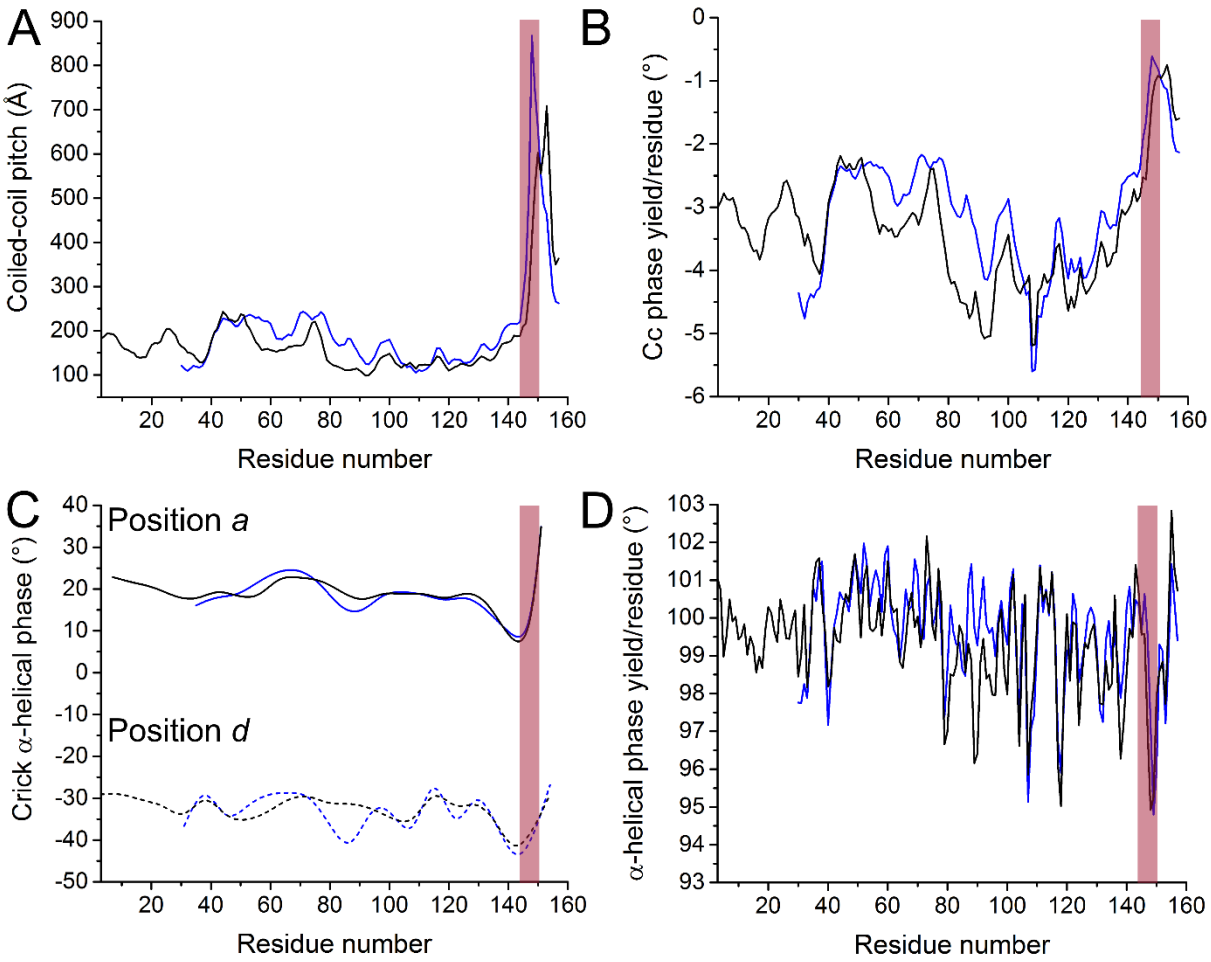

Figure 4.11 Local coiled coil parameters plotted against residue numbers of $(GCN4)_3$-T1L σ1(29-159) and T1L σ1(29-159). $(GCN4)_3$-T1L σ1(29-159) plots are shown in black, and T1L σ1(29-159) plots are shown in blue. The stutter location is indicated with a red bar. **(A)** Coiled coil pitch. The average pitch of $(GCN4)_3$-T1Lσ1 is 157 ± 44 Å and of T1L σ1(29-159) is 174 ± 55 Å. The pitch locally increases at the stutter position. **(B)** Coiled-coil phase yield per residue (the angle between two consecutive residues relative to the vectors connecting the Cα-atoms and the coiled coil axis). Typical values for left-handed coiled coils are around -4°. Right-handed coiled coils have positive values. At the stutter, the coiled-coiled phase yield increases. **(C)** Crick α-helical phase. The Crick angle, which defines the phase of the Cα-atoms relative to the coiled coil axis is plotted for positions *a* and *d*. (In an idealized coiled coil residues in *a* positions have values ~ -30° and *d* positions have values ~ 20°). At the stutter the Crick angles have a minimum. Values are increased C-terminal the stutter. **(D)** α-helical phase yield per residue (the angle between two consecutive residues relative to the vectors connecting the C_α-positions to the α-helical axis) decreases at the stutter position.

4.2 T3D σ1 Fragments

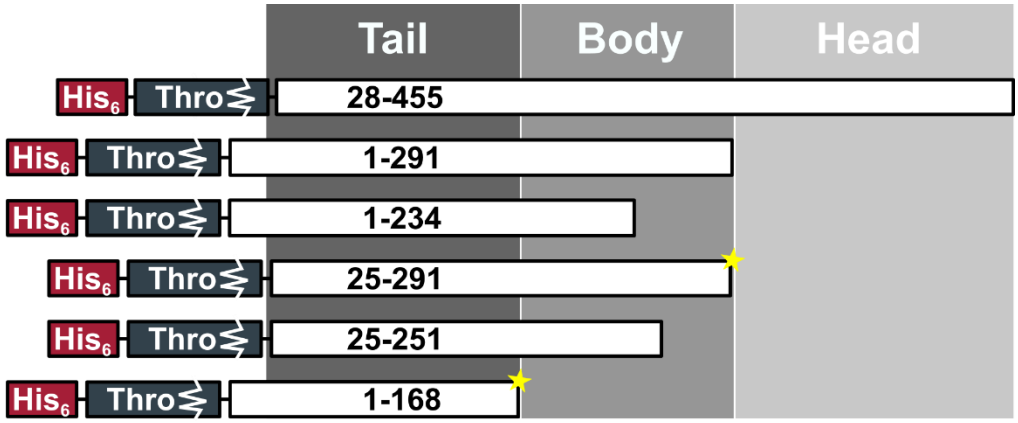

Figure 4.12 Overview of T3D σ1 constructs. The sizes of the σ1 fragments are indicated as white boxes of different length. His_6-tags and the thrombin (Thro) cleavage sites are indicated. Constructs that led to a crystal structure are marked with a star.

4.2.1 T3D σ1(28-455 and 30-455)

The T3D σ1 constructs comprising amino acids 28-455 and 30-455 were cloned via NheI and BamHI restriction sites into pET28b. The His_6-tagged proteins were over-expressed as verified by immunoblotting, but they were insoluble in all buffers tested.

4.2.2 Coiled Coil – Body Constructs of T3D σ1

The T3D σ1 constructs comprising amino acids 1-291, 1-234, 25-291, and 25-251 were cloned via NheI and HindIII restriction sites into pET28b. With the exception of T3D σ1(1-234), all constructs could be over-expressed by induction with 0.3 mM IPTG at 20°C. The His_6-tag could be removed by on-column digestion with thrombin, or the tagged-proteins could be eluted from the Ni-affinity chromatography column with an imidazole concentration of about 150 mM.

T3D σ1 (25-291) – Purification and Crystallization

His_6-tagged T3D σ1(25-291) was separated from aggregated protein by size exclusion chromatography (Figure 4.13). The protein concentration was adjusted for crystallization with a precipitation test.

Small needle clusters were obtained in 40% MPD, 0.1 M Tris pH 8.0 at 4°C. The additive screen (Hampton research) was applied to optimize the crystallization condition, and small needle-like clusters were obtained first in several conditions. After four weeks,

three-dimensional crystals grew in some conditions that contained linker molecules (10 mM taurine; 10 mM betaine hydrochloride; 3% (w/v) 1,6-diaminohexane). SDS-PAGE with samples of dissolved crystals and the protein solution stored at 4°C revealed that the protein was degraded over time. The gel bands were analyzed by MALDI-mass spectrometry (Lisa Kraft, AK Kalbacher, University of Tuebingen). The identified fragments cover the T3D σ1 sequence from residue 38 almost completely until residue R262 (Appendix).

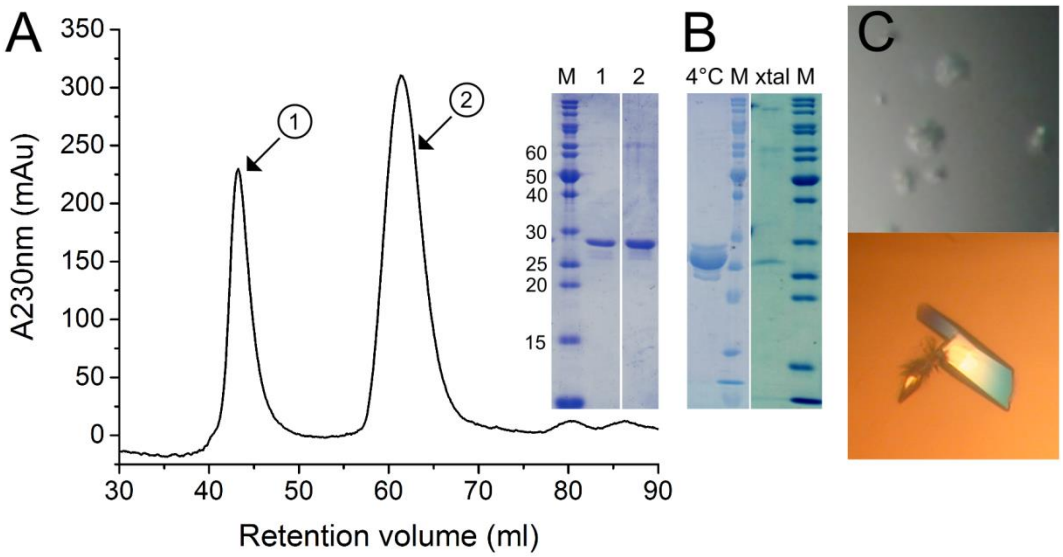

Figure 4.13. Purification and crystallization of T3D σ1(25-291). (A) Size exclusion chromatogram of T3D σ1(25-291). The absorbance is shown at 230 nm. The protein is present in the void volume (1) and in the second peak (2) indicated by the SDS-PAGE gel. **(B)** The protein degraded over time. The protein solution that was used for crystallization and stored at 4°C was loaded on the SDS-PAGE gel ~1 week after purification (4°C). Crystals that have been used for structure determination were dissolved and subjected to SDS-PAGE (xtal). In comparison to the freshly purified protein the majority of the protein runs at a lower molecular weight. **(C)** Initial crystals of T3D σ1(25-291) in 40% MPD, 0.1 M Tris pH 8.0 are shown on the upper picture. Crystal used for structure determination is shown on the lower picture (40% MPD, 0.1 M Tris and 3% (w/v) 1,6-Diaminohexane).

T3D σ1 (25-291) – Crystal Structure

A complete data set to 2.25 Å resolution was collected and used for solving the structure by molecular replacement. The crystals belonged to space group C2 and contained one σ1 trimer in the asymmetric unit.

Table 4.4 Data collection and refinement statistics of T3D σ1(25-291)

Data collection	**T3D σ1(25-291)**
Resolution range [Å]	49.1-2.25 (2.31-2.25)
Space group	C121
Unit cell dimensions [Å]	351.2, 41.6, 63.4
Unit cell angles [°]	90.0, 95.3, 90.0
Completeness [%]	99 (98)
Total reflections	295462 (22021)
Unique reflections	43612 (3206)
R_{meas} [%]	13.3 (91.2)
$CC_{1/2}$ [%]	100 (83)
I/σ	12.1 (2.1)
Wilson B [Å^2]	38.5
Refinement	
R_{work}/ R_{free} [%]	22.3/ 24.7
Atoms	
Protein	4748
Waters	420
B factors [Å^2]	
Chain A	46.1
Chain B	47.5
Chain C	46.5
Water	41.0
r.m.s.d. bond lengths [Å]	0.004
r.m.s.d. bond angles [°]	0.755

Values in parentheses are for the highest-resolution shell.

The protein folds into a parallel α-helical coiled coil and four triple β-spiral repeats, β1-β4 (Figure 4.14). Few residues that belong to the short coiled coil of the T3D σ1 body domain are visible in the electron density (defined residues: chain A 27-243, chain B 27-240, chain C 27-239). The body domain and the N-terminal half of the coiled coil contribute most of the crystal contacts. The middle part of the coiled coil does not interact with adjacent proteins and therefore, has temperature factors between 70-85 Å^2. The main chain atoms of the different chains of the coiled coil superimpose with the appropriate T1L σ1 coiled coil residues with a r.m.s.d. value between 1.4-1.7 Å. The coiled coil domain consists of 20 heptads and is ~ 205 Å long. Six interhelical salt bridges are distributed over the entire length of the coiled coil and stabilize the structure.

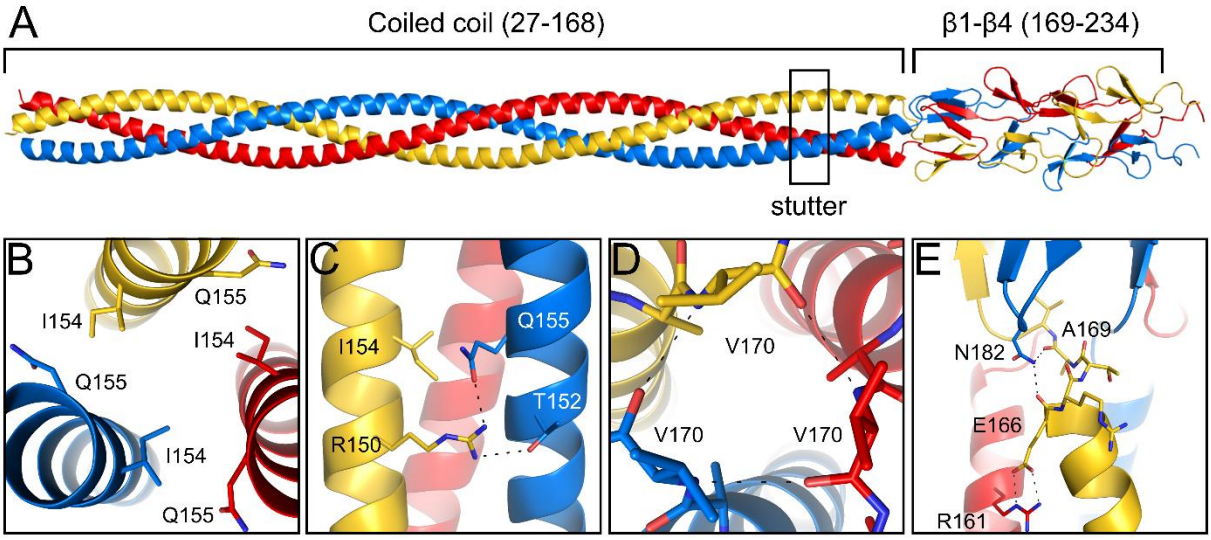

Figure 4.14 Crystal structure of T3D σ1(25-291). The σ1 protein is colored in blue, red, and yellow. **(A)** The protein folds into a trimeric parallel α-helical coiled coil domain (residues 27-168) and a body domain that consists of four triple β-spiral repeats, β1-β4 (residues 169-234). **(B)** Close-up of the stutter, with view along the threefold axis. I154 is shifted outward of the core and forms a *da*-layer with Q155. **(C)** Q155 also interacts with R150 that also contacts T152 of an adjacent α-helix. **(D)** Backbone-backbone interactions between V170 residues at the domain-transition site. View along the threefold axis. **(E)** The two domains are connected by a direct interaction between body domain residue N182 and carbonyl groups of A169 and E166, which are located at the end of the coiled coil. An interhelical salt bridge formed by E166 and R161 stabilizes the end of the coiled coil.

Few hydrophilic amino acids occupy typically hydrophobic positions *a* and *d*. Residues S39 (position *a*) and H42 (position *d*) bind several water molecules inside the core (Figure 4.15). The B-factors of the water molecules are similar to the surrounding amino acids, indicating full occupancy. A second histidine residue, H123, is located at position *a,* but the water bound at the trimer interface has a higher B-factor, and its electron density is weaker in comparison to the other bound water molecules.

A stutter is located close to the C-terminal end of the coiled coil domain. This discontinuity of the heptad repeat of a four amino acid insertion (here: VTSI; 151-154) is compensated by a local unwinding of the α-helices and the coiled coil. The unwinding of the coiled coil is detected by a local increase of the coiled coil pitch and a minor decrease in the α-helical phase yield per residue indicates the local unwinding of the α-helices. Residue I154 at the *d* position of the stutter is shifted outside of the core and forms a *da*-layer with Gln155. The C_β and C_γ atoms of Q155 contribute to the hydrophobic interaction with I154. Q155 additionally interacts with R150, which further contacts T152 from an adjacent subunit.

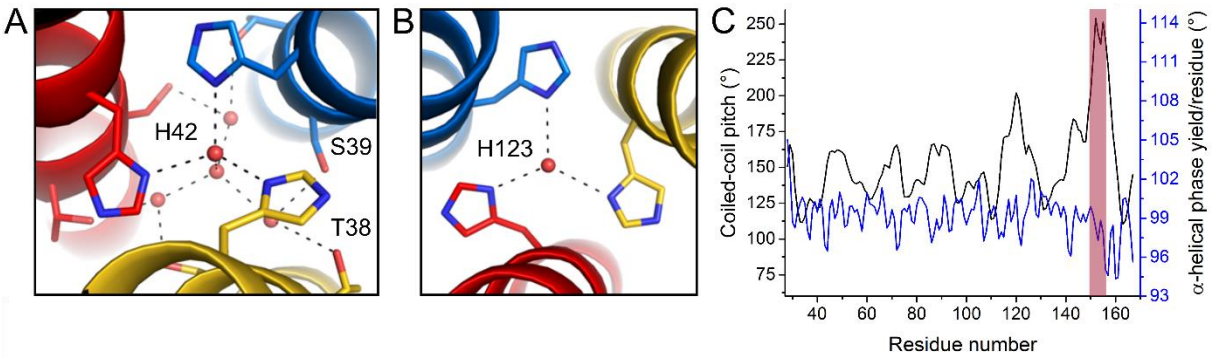

Figure 4.15 Bound water molecules inside the core and local coiled coil parameters plotted against residue numbers of T3D σ1(25-291). The σ1 chains are colored in blue, red and yellow. Water molecules are shown as red spheres. **(A)** S39 at position *a* and H42 at position *d* of the heptad repeat bind water molecules inside the core. **(B)** H123 binds a water molecule at the trimer interface. **(C)** The coiled coil pitch (black line) and the α-helical phase yield (the contribution to the α-helical turn) per residue (blue line) are plotted against the residue number. The stutter location is indicated with a red bar. The average pitch of the T3D σ1 coiled coil domain was calculated with the program twister to 148 ± 23 Å. The pitch locally increases and the α-helical phase yield per residue locally decreases at the stutter position.

The body domain is directly connected to the coiled coil, and no intrinsic flexible region was observed between the two domains. N182 of the body domain interacts with carbonyl groups of A169 and E166, which are located at the C-terminal end of the coiled coil. E166 also forms an interhelical salt bridge with R161 stabilizing the end of the helical bundle. The β-spiral repeats, β1-β4, are similar to a previously solved T3D σ1 structure ([19], PDB ID: 3S6X). The main chain atoms of the corresponding parts superimpose with a r.m.s.d. value of 0.63 Å.

T3D σ1 (1-291) – Purification and Crystallization

The cleaved protein T3D σ1(1-291) was tested for pH-stability. Size exclusion chromatography of the protein in different buffers demonstrated that it is almost insoluble at a pH of 7.6, while it is soluble at higher pH values. Minor aggregation was observed at a pH of 8.6 and, even after several weeks, the protein was not degraded.

4.2.3 Coiled coil Construct

T3D σ1 (1-168) – Purification and Crystallization

The T3D σ1 construct comprising amino acids 1-168 was generated by introducing a stop codon into pET28b::His_6-T3D σ1(1-291) at the position corresponding to Ala169 via site-directed mutagenesis.

The protein was separated from most impurities by binding to a Ni-affinity chromatography column. On-column digestion was followed by size exclusion chromatography (Figure 4.16). The untagged protein contains six additional amino acids (Gly-Ser-His-Met-Ala-Ser) at the N-terminus due to the cloning procedure.

Crystals of T3D σ1(1-168) were obtained with the hanging drop vapor diffusion method in 70% MPD, 0.1 M HEPES pH 7.5 at 20°C. A complete data set extending to 1.6 Å resolution was collected, and the structure was solved via determining phases by molecular replacement. The program Sfcheck (CCP4) [112] calculated ~25% pseudo-translational symmetry.

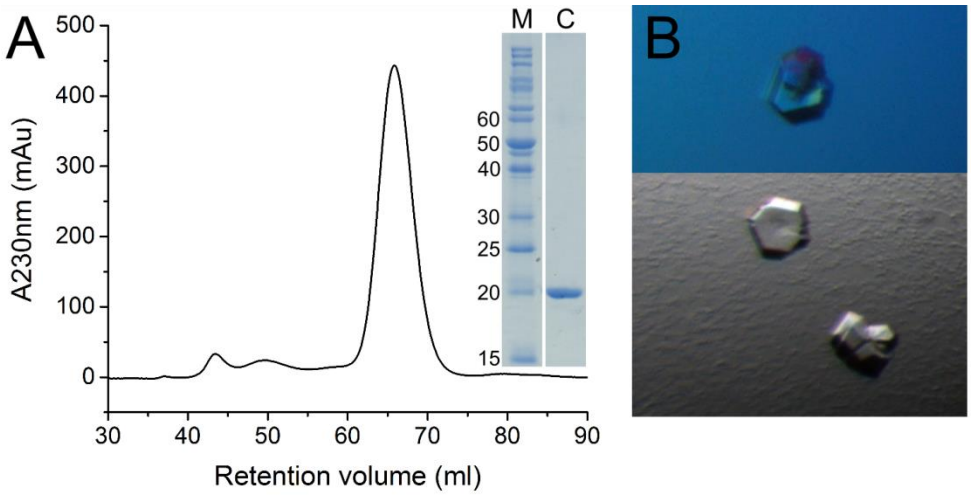

Figure 4.16 Purification and crystallization of T3D σ1(1-168). (A) Size exclusion chromatogram of T3D σ1(1-168). The absorbance is shown at 230 nm. An SDS-PAGE gel showing the concentrated protein is included. A band at ~19 kDa corresponds to the molecular weight of the protein. **(B)** Crystals of T3D σ1(1-168) in 70% MPD, 0.1 M HEPES pH 7.5 at 20°C.

T3D σ1 (1-168) – Crystal Structure

The structure was solved in the space group R32 with one σ1 monomer in the asymmetric unit (Table 4.5). The biological σ1-trimer is formed by the crystallographic symmetry. There is no electron density present for the N-terminus (residues 1-24) and the last six residues of the C-terminus. Residues 25-94 are well defined and possess low B-factors (Figure 4.17). This part of the structure is involved in most crystal contacts, while residues 95-162 contribute little to the crystal packing contacts, have higher B-factors and the electron density is poorly defined. Due to the high percentage of pseudo-translation and the region of poor electron density, the R-factors of the structure (R_{work} 23.6%, R_{free}: 25.4%) are high for a resolution of 1.6 Å.

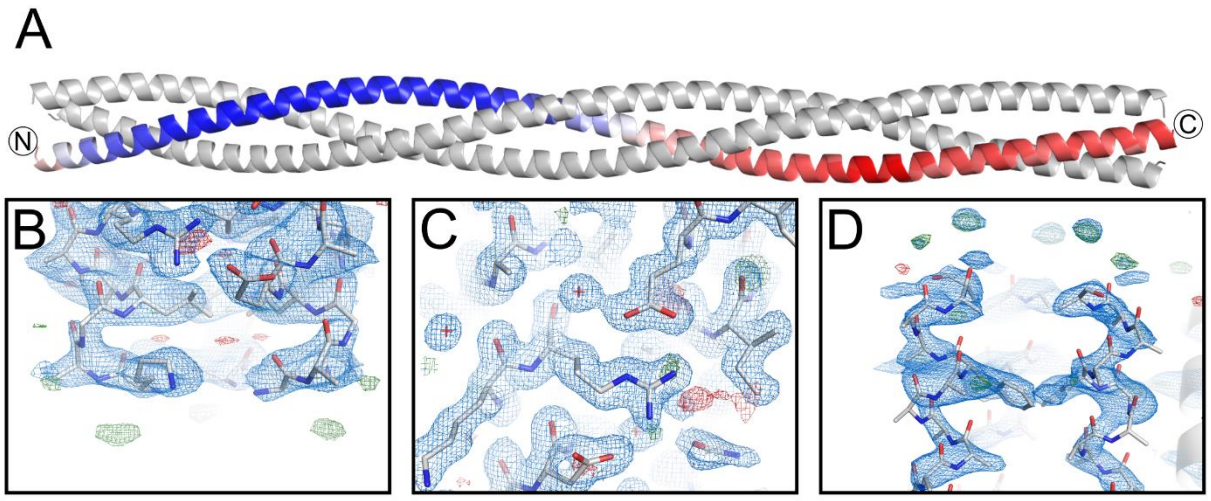

Figure 4.17 Crystal structure of T3D σ1(1-168). (A) The σ1 monomer that forms the asymmetric unit is colored according to B-factors from blue (15 Å^2) to red (120 Å^2). The symmetry-related molecules that complete the σ1 trimer are colored in grey. The N-and C-termini are indicated. **(B)** Close-up view of the N-terminal residues that are defined in the electron density. **(C)** Well defined electron density of residues with low B-factors. **(D)** Poorly defined electron density of the C-terminal residues that have high B-factors. The $2F_o$-F_c electron density map is contoured in blue at 1.0 σ and the F_o-F_c map is contoured in green at 3.0 σ and red at -3.0 σ.

Table 4.5 Data collection and Refinement statistics of T3D σ1(1-168)

Data collection	**T3D σ1(1-168)**
Resolution range [Å]	41.0-1.6 (1.64-1.60)
Space group	R32
Unit cell dimensions [Å]	38.5, 38.5, 737.3
Unit cell angles [°]	90, 90, 120
Completeness [%]	100 (100)
Total reflections	545257 (37568)
Unique reflections	29360 (2077)
R_{meas} [%]	7.7 (135)
$CC_{1/2}$ [%]	100 (78.7)
I/σ	22.9 (2.3)
Wilson B [Å^2]	31.1
Refinement	
R_{work}/ R_{free} [%]	23.0/ 25.1
Atoms	
Protein	1003
Waters/ MPD	69/ 24
B factors [Å^2]	
Chain A	56.6
Water	45.2
MPD	55.9

r.m.s.d. bond lengths [Å]	0.015
r.m.s.d. bond angles [°]	1.209

Values in parentheses are for the highest-resolution shell.

4.3 Interactions between σ1 and Neutralizing Antibodies

4.3.1 Formation and Crystallization of σ1-Fab Complexes

Stable σ1-Fab complexes were formed and subsequently purified and separated from excess Fabs by SEC (Figure 4.18). Crystals of the T1L σ1-5C6 Fab complex were obtained with a concentration of 1-4 mg/ml in 9.5-11.5% (w/v) PEG8000, 0.1 M MES (pH 5.5-6.5), and 0.2 M zinc acetate at 4°C using the hanging-drop vapor diffusion method. Mother liquor containing 12% MPD was used as cryoprotectant. Diffraction data from two crystals were collected, processed, and merged for structure determination by molecular replacement.

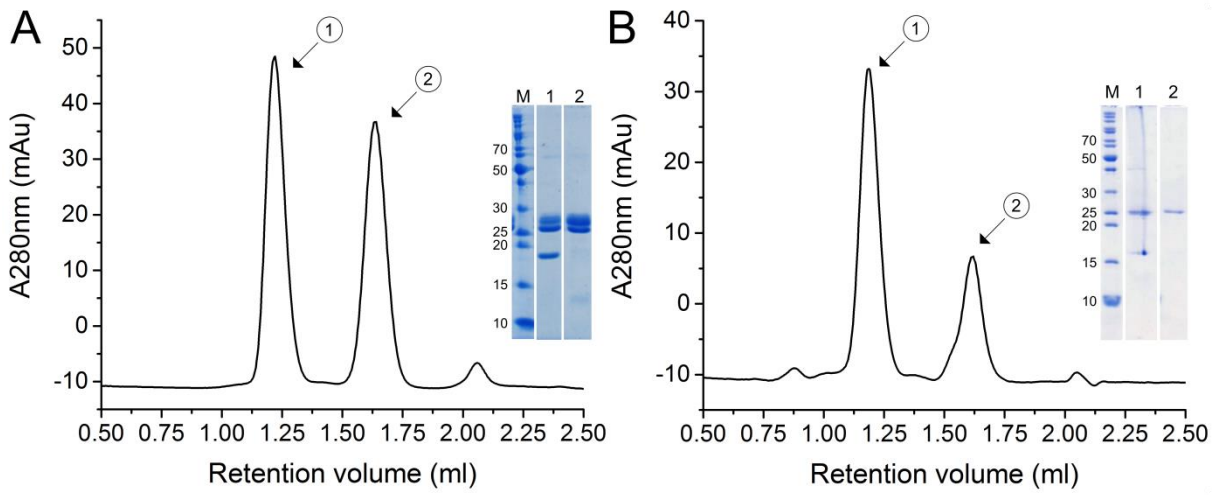

Figure 4.18 Complex formation and purification of σ1-Fab complexes. Size exclusion chromatogram with the absorbance shown at 280 nm. **(A)** The two peaks contain T1L σ1-5C6 Fab complex (peak 1) and excess of Fabs (peak 2). A SDS-PAGE gel is included. Light and heavy chains of 5C6 have molecular weigths of ~24 kDa, and T1L σ1 head has a molecular weight of ~18.5 kDa. **(B)** The T3D σ1-9BG5 Fab complex (peak 1) is separated from excess Fabs (peak 2). A SDS-PAGE gel is included. Light and heavy chains of 9BG5 have molecular weigths of ~24 kDa, and T3D σ1 head has a molecular weight of ~17.7 kDa.

Crystals of the T3D σ1-9BG5 Fab complex were obtained with a concentration of 1-2 mg/ml in 10-12% (w/v) PEG8000, 0.1 M Tris (pH 6.5-7.5), and 0.2 M magnesium

chloride at 4°C using the hanging-drop vapor diffusion method. The reservoir solution was covered with ~150 µl silicone oil to reduce vapor diffusion due to initially fast growing crystals. Mother liquor containing 12% MPD was used as cryoprotectant. The structure was solved by molecular replacement.

4.3.2 Crystal Structure of T1L σ1-5C6 Fabs

The 3.7 Å resolution structure of T1L σ1 head in complex with 5C6 Fabs was solved in space group C2 with one trimeric σ1 head and three Fab molecules in the asymmetric unit (Table 4.6). The variable domains (V_L and V_H) of 5C6 are well ordered, and the interaction area with σ1 is well defined in the electron density map, while the constant domains (C_L and C_H) of 5C6 are poorly visible. The T1L σ1 fragment folds into one β-spiral repeat and the globular head domain. The upper part of the σ1 head is faced by the variable domains V_L and V_H of three Fab molecules (Figure 4.19). Each Fab spans two σ1 subunits. The σ1-Fab contact buries a surface of 727 $Å^2$ from the solvent with light and heavy chain contributions of 171 $Å^2$ and 556 $Å^2$, respectively.

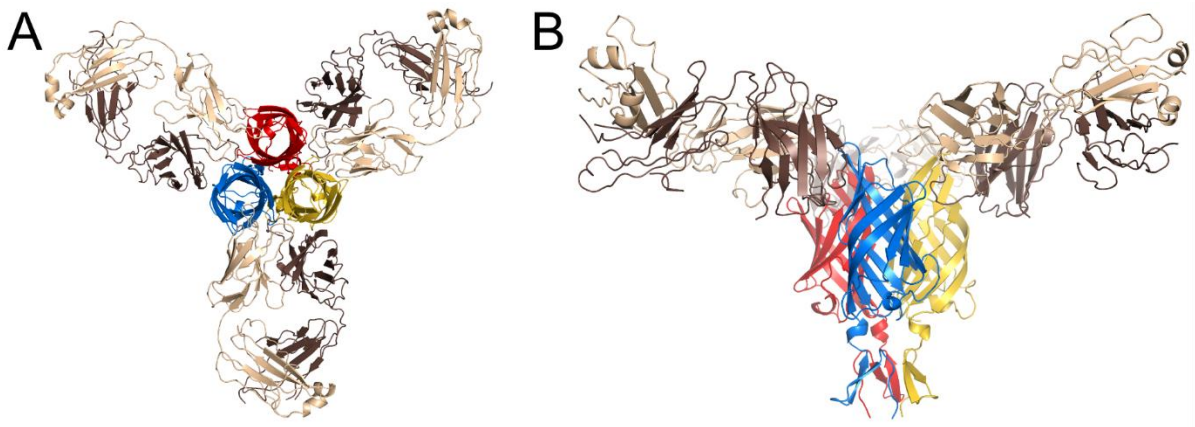

Figure 4.19 Crystal structure of T1L σ1 head in complex with 5C6 Fabs. Subunits of σ1 are colored in blue, red, and yellow. The light and heavy chains of the 5C6 Fab fragment are shown in light and dark brown. **(A)** Top view along the σ1-threefold-axis. The σ1 head domain is surrounded by three Fab molecules. Each Fab fragment spans two σ1 subunits, appearing to stabilize the trimeric state of σ1. **(B)** Side view, showing 5C6 Fabs binding at the upper, C-terminal region of the σ1 head.

The σ1 protein is exclusively engaged by the complementarity-determining regions (CDRs) of 5C6, which are referred to as L1-L3 for CDRs 1-3 of V_L and H1-H3 for CDRs 1-3 of V_H, respectively (Figure 4.20). Three of the six CDRs are involved in binding σ1: L1, H2, and H3. L2 likely forms only a single hydrogen bond with σ1, whereas L3 and H1 do not interact with σ1 at all.

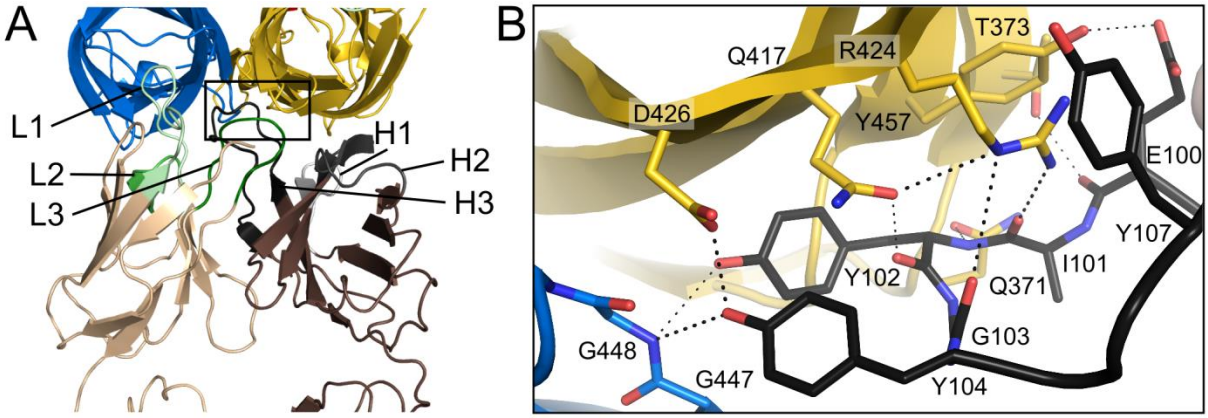

Figure 4.20 Contacts between T1L σ1 head and 5C6 Fabs. Subunits of σ1 are colored in blue, red, and yellow. The light and heavy chains of the 5C6 Fab fragment are shown in light and dark brown. **(A)** Close-up view of 5C6 Fab binding across two σ1 subunits. CDR loops are highlighted in light (L1, H1), medium (L2, H2), and dark (L3, H3) green in case of V_L, and grey in case of V_H. Black box indicates the location of the interactions shown in **(B).** CDR H3 interacts mainly with one σ1 subunit by forming several hydrogen bonds with σ1 residues from four different β-strands. R424^{σ1} is engaged by the carbonyl groups of I101^{H3} and G103^{H3} and is sandwiched by Y107^{H3} and Y457^{σ1}. Both Y102^{H3} and Y104^{H3} interact with σ1 residues from both subunits simultaneously. Y102^{H3} forms hydrogen bonds with Q371^{σ1}, G448^{σ1}, and Q417^{σ1}, and Y104^{H3} forms hydrogen bonds with G448^{σ1} and D426^{σ1}.

H3 contributes substantially to the interaction with σ1. This CDR extensively contacts one σ1 subunit, forming multiple hydrogen bonds with σ1 residues from four β-strands. A key interaction involves R424^{σ1}, which forms hydrogen bonds with the carbonyl groups of I101^{H3} and G103^{H3} as well as the side chain of Q417^{σ1}. Residue R424^{σ1} additionally makes cation-π interactions with Y107^{H3} and Y457^{σ1}. The long H3 CDR also contacts the interface of two σ1 subunits. Y102^{H3} and Y104^{H3} interact with σ1 residues from both subunits simultaneously. Y102^{H3} forms hydrogen bonds with Q371^{σ1}, G448^{σ1}, and Q417^{σ1} using its amine, hydroxyl, and carbonyl groups, respectively. G448^{σ1} and D426^{σ1} are contacted by the Y104^{H3} side chain.

Table 4.6 Data collection and refinement statistics of T1L σ1 – 5C6 Fabs

Data collection	**T1L σ1 – 5C6 Fabs**
Resolution range [Å]	48.99 - 3.70 (3.80 - 3.70)
Space group	C2
Unit cell dimensions [Å]	223.6, 129.1, 87.9
Unit cell angles [°]	90, 101.24, 90
Completeness [%]	99.9 (99.7)
Total reflections	314028 (24377)
Unique reflections	26264 (1965)
R_{meas} [%]	29.5 (161.9)
$CC_{1/2}$ [%]	99.1 (74.8)

I/σ	7.94 (1.71)
Wilson B [Å^2]	90.7
Refinement	
R_{work}/ R_{free} [%]	23.6/ 28.0
Atoms	
Protein	12621
B factors [Å^2]	
Chain A, B, C	53.2, 51.8, 54.7
Chain D, E,F,	119.7, 121.5, 136.9
Chain G, H, I	136.3, 144.7, 136.3
r.m.s.d. bond lengths [Å]	0.01
r.m.s.d. bond angles [°]	1.28

Values in parentheses are for the highest-resolution shell.

4.3.3 Crystal Structure of T3D σ1-9BG5 Fabs

The 3.0 Å resolution structure of the T3D σ1 head in complex with 9BG5 Fabs was solved in space group P1 with two trimeric σ1 proteins and six Fab molecules in the asymmetric unit (Table 4.7).

Similar to the T1L σ1-5C6 structure, three 9BG5 Fab molecules engage the head domain of T3D σ1, and each Fab spans two σ1 subunits (Figure 4.21). However, the location of the 9BG5 mAb epitope is different. 9BG5 binds to the side of the T3D σ1 head domain, while 5C6 engages T1L σ1 closer to the top of the head domain. The σ1-Fab contact buries a surface of 905 Å^2 from solvent with almost equal contributions of the light (436 Å^2) and heavy chains (469 Å^2).

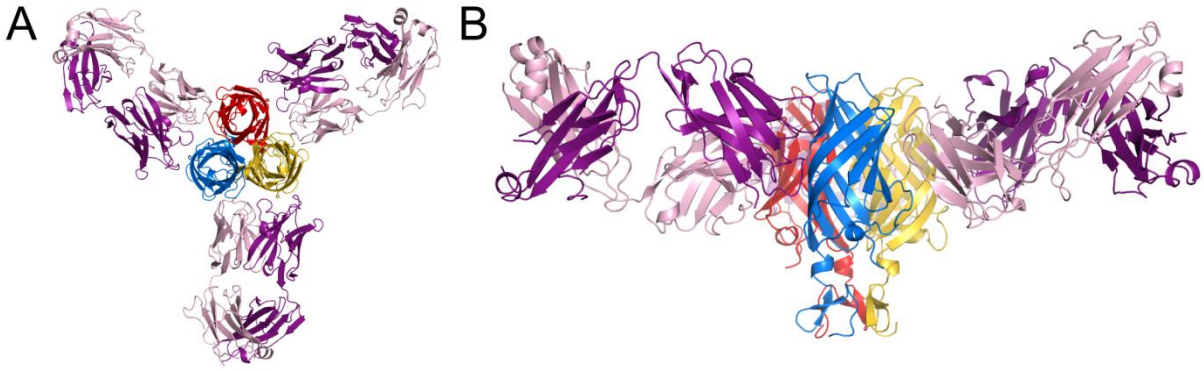

Figure 4.21 Crystal structure of T3D σ1 head in complex with 9BG5 Fabs. Subunits of σ1 are colored in blue, red, and yellow. The light and heavy chains of the 9BG5 Fab fragment are shown in light and dark violet. **(A)** Top view along the σ1-threefold-axis. The σ1 head domain is surrounded by three Fab molecules. Each Fab fragment spans two σ1 subunits, appearing to stabilize the trimeric state of σ1. **(B)** Side view, showing 9BG5 Fabs binding σ1 in the middle of the head domain.

Five of the six CDRs are in contact with the flat epitope (Figure 4.22). L1 forms an extended hydrogen bond network with σ1 involving eight direct interactions. Residue E419$^{\sigma1}$, which forms an intramolecular salt bridge with R427$^{\sigma1}$, is faced by L1 residues S30^{L1}, S31^{L1}, and N32^{L1}. Residue N32^{L1} also interacts with the carbonyl group of V392$^{\sigma1}$ and with the guanidine group of R51^{L2}, which also forms a salt bridge with D340$^{\sigma1}$ located at the interface between two σ1 subunits. CDRs H1, H2, and H3 participate in intermolecular contacts with several hydrophobic interactions, a small number of hydrogen bonds, and one cation-π interaction.

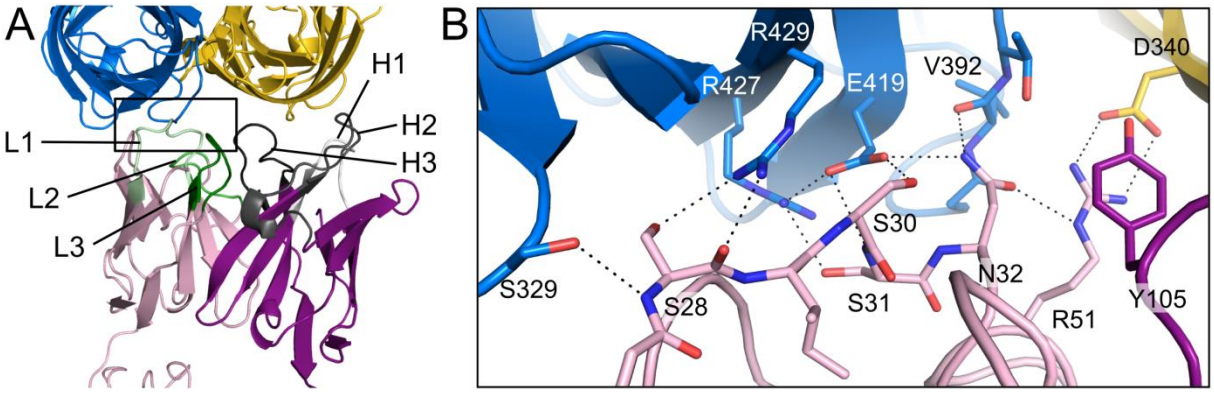

Figure 4.22 Contacts between the T3D σ1 head and 9BG5. Subunits of σ1 are colored in blue and yellow. The light and heavy chains of the 9BG5 Fab fragment are shown in light and dark violet. **(A)** CDR loops are highlighted in light (L1, H1), medium (L2, H2), and dark (L3, H3) green in case of V_L and grey in case of V_H. The black box indicates the location of the interactions shown in **(B).** The CDR L1 loop forms an extensive hydrogen-network with one σ1 subunit. E419$^{\sigma1}$ makes an intramolecular salt bridge with R427$^{\sigma1}$ and is faced by the three Fab residues, S30^{L1}, S31^{L1}, and N32^{L1}. CDR L2 residue R51^{L2} forms an intermolecular salt bridge with D340$^{\sigma1}$ and is stabilized by a cation-π interaction with Y105^{H3}.

Table 4.7 Data collection and refinement statistics of T3D σ1 – 9BG5 Fabs

Data collection	**T3D σ1 – 9BG5 Fabs**
Resolution range [Å]	49.04 - 3.00 (3.08 – 3.00)
Space group	P1
Unit cell dimensions [Å]	103.2, 109.3, 131.7
Unit cell angles [°]	103.1, 113.6, 103.5
Completeness [%]	98.5 (98.4)
Total reflections	338722 (26084)
Unique reflections	94667 (7020)
R_{meas} [%]	11.6 (85.4)
$CC_{1/2}$ [%]	99.5 (64.7)
I/σ	13.08 (1.89)
Wilson B [Å^2]	55.9

Refinement	
R_{work}/ R_{free} [%]	22.3/ 24.7
Atoms	
Protein	24507
B factors [Å^2]	
Chains A, B, C	45.4, 45.9, 45.6
Chains D, E,F,	50.5, 52.4, 55.7
Chains G, H, I	75.3, 77.4, 76.3
Chains J, K, L	94.6, 106.6, 99.2
Chains M, N, O	110.2, 74.1, 80.3
Chains P, Q, R	94.9, 80.7, 98.2
r.m.s.d. bond lengths [Å]	0.004
r.m.s.d. bond angles [°]	0.99

Values in parentheses are for the highest-resolution shell.

4.3.4 Affinity Determination of Fabs for σ1

Surface plasmon resonance (SPR) experiments with immobilized σ1 heads and Fabs as analytes were conducted to obtain affinity and kinetic data for the interaction of σ1 with Fabs (Figure 4.23). Both, 5C6 and 9BG5 Fabs bound their target σ1 with low nanomolar affinity following a 1:1 Langmuir interaction model. The K_D values of the Fab-σ1 interactions are similar, with 2.0 (± 0.1) × 10^{-9} M for T1L σ1-5C6 and 2.5 (± 0.2) × 10^{-9} M for T3D σ1-9BG5, but the binding kinetics differ. The T1L σ1-5C6 Fab complex has significantly lower association and dissociation rates compared to the T3D σ1-9BG5 Fab complex.

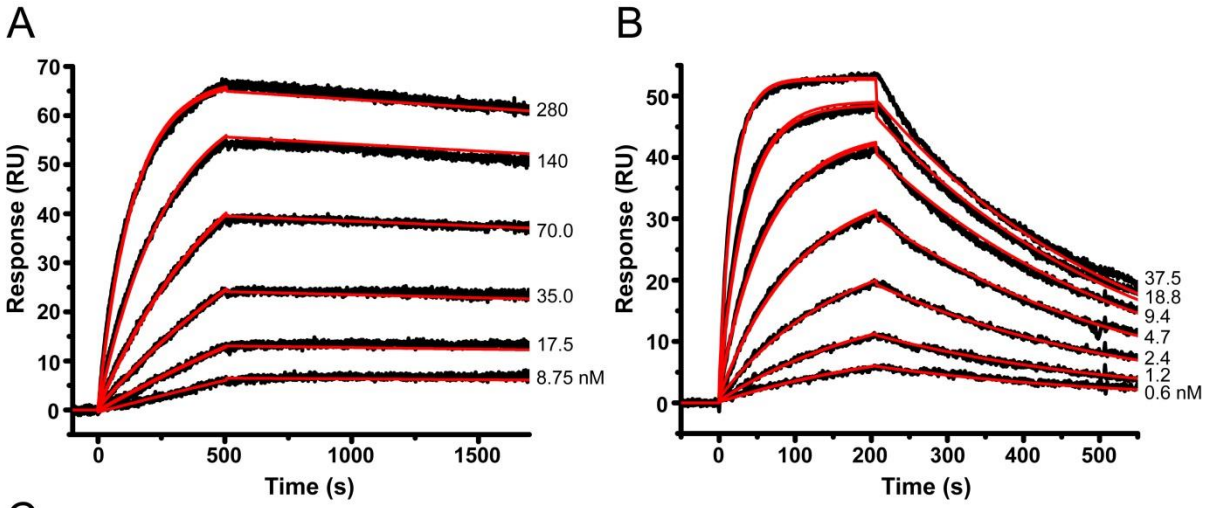

C

	ka ($M^{-1}s^{-1}$)	kd (s^{-1})	K_D (M)	χ^2
T1L σ1 with 5C6 Fabs	2.6 (± 0.2) × 10^4	5.1 (± 0.3) ×10^{-5}	2.0 (± 0.1) × 10^{-9}	0.621
T3D σ1 with 9BG5 Fabs	1.2 (± 0.1) × 10^6	2.9 (± 0.1) ×10^{-3}	2.5 (± 0.2) × 10^{-9}	0.453

Figure 4.23 Kinetics of Fab binding to σ1. Representative SPR-binding studies of the T1L σ1 head with 5C6 Fabs **(A)** and the T3D σ1 head with 9BG5 Fabs **(B)**. The σ1 protein was immobilized on a sensor chip, and twofold dilutions of Fab fragments were injected in duplicate. Fab concentrations ranging from 280 to 8.8 nM for 5C6 **(A)** and from 37.5 to 0.6 nM for 9BG5 **(B)** are indicated at the right of each sensorgram. The data sets were globally fitted (red lines) to a 1:1 Langmuir binding model. The corresponding χ^2 values are indicated in the table below. **(C)** The K_D values and, association (ka) and dissociation (kd) constants and their standard deviations were determined using three independent measurements.

4.3.5 Affinity Determination of hJAM-A for σ1

SPR experiments with immobilized σ1 heads and the human JAM-A ectodomain as analyte were conducted to determine affinities of T1L and T3D σ1 for JAM-A (Figure 4.24). The JAM-A molecule bound to both T1L and T3D σ1 with high nanomolar affinities with average K_D values of 2.0 (± 0.1) × 10^{-7} M for T1L σ1 and 5.3 (± 0.5) × 10^{-7} M for T3D σ1. Due to high on- and off-rates of JAM-A binding to σ1, kinetic parameters of the interaction could not be determined.

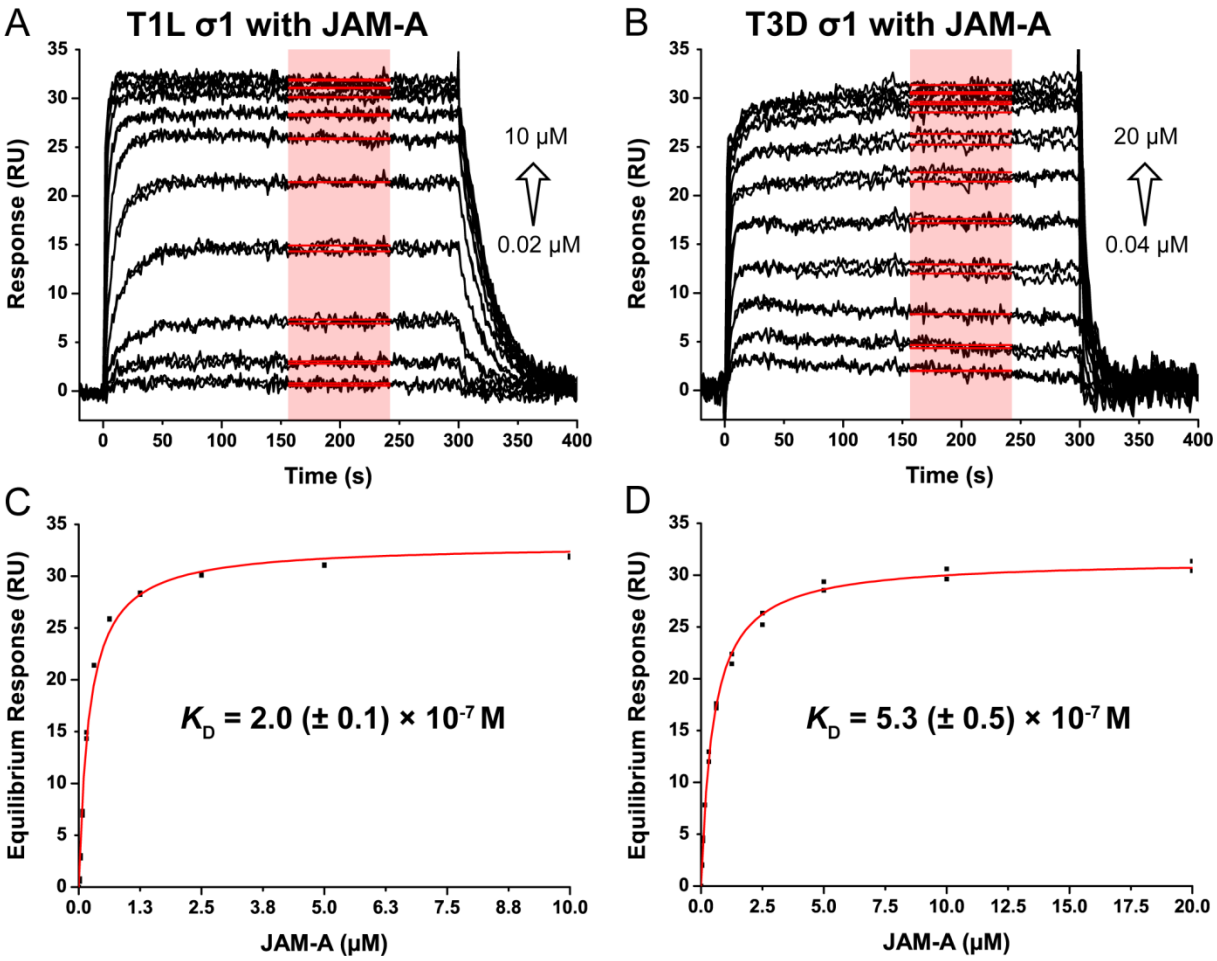

Figure 4.24 SPR studies of JAM-A binding to σ1. Representative sensorgrams of 10 different JAM-A concentrations **(A**: 0.02 to 10 µM, **B:** 0.04 to 20 µM) injected in duplicate over immobilized T1L σ1 **(A)** and T3D σ1 **(B)**, respectively, at 25°C. Red boxes indicate the range used for calculation of equilibrium response values. Binding curve of JAM-A to T1L σ1 **(C)** and T3D σ1 **(D)**. The equilibrium response values are plotted against the injected JAM-A concentrations. *K*D values are indicated. Copyright © American Society for Microbiology, JVI, 89, 2015, 6136-6140, doi:10.1128/JVI.00433-15.

4.3.6 JAM-A Binding to σ1-mAb complexes

To investigate whether JAM-A can engage σ1 saturated with neutralizing antibodies, I conducted SPR-measurements with the σ1 head domain immobilized on a biosensor chip (Figure 4.25).

The response of 5C6 Fabs (~160 RU) and the JAM-A ectodomain (~71 RU) to σ1 was tested first. 5C6 antibodies were injected twice and Fabs were applied to the surface immediately afterwards to determine whether all accessible binding sites of σ1 were engaged by the mAbs. Injection of the JAM-A ectodomain followed and the response level increased (~67 RU), indicating binding of the soluble protein to a T1L σ1-5C6 mAb complex. After surface regeneration, the response level of JAM-A or 5C6 Fabs was

tested again and showed that a similar amount of JAM-A can bind to σ1 alone and to a σ1-mAb complex.

In the case of T3D σ1, 9BG5 mAb injection was directly followed by an injection of 9BG5 Fabs to determine whether all accessible σ1 epitopes were bound by the mAbs. A second injection of 9BG5 mAbs to surface saturation was followed by injection of the JAM-A ectodomain. The response level increased (~ 30 RU), suggesting binding of the soluble JAM-A protein to a T3D σ1-9BG5 mAb complex. Response levels of 9BG5 Fabs and JAM-A (27 RU) to σ1 alone were evaluated after surface regeneration and showed that similar amounts of JAM-A can bind to σ1 alone and to the σ1-mAb complex.

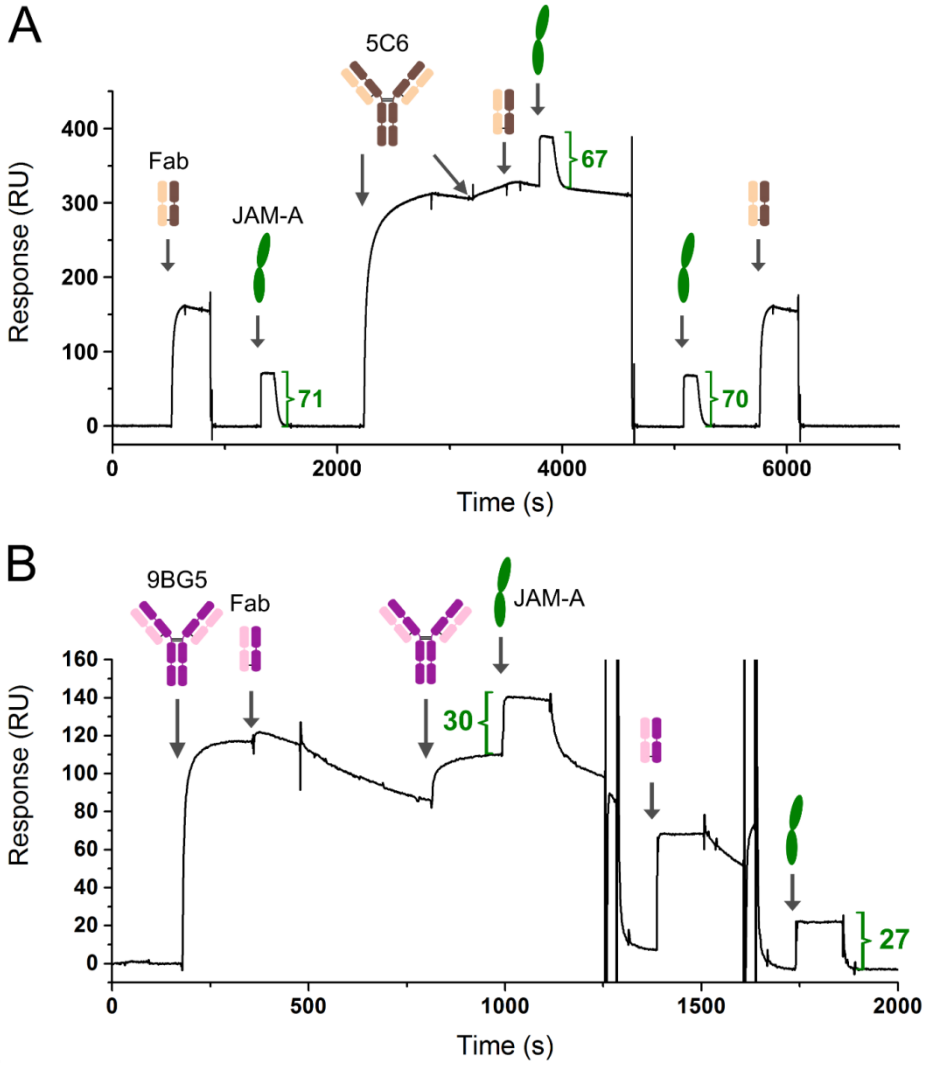

Figure 4.25 Binding of the soluble ectodomain of reovirus receptor JAM-A to σ1 complexed with mAbs. Shown are reference SPR sensorgrams. **(A)** JAM-A binding to immobilized T1L σ1 complexed with 5C6 mAbs was observed. Control experiments pre- and post-complex formation with JAM-A and 5C6 Fabs were performed and showed that similar amounts of JAM-A bound to σ1 alone and to a σ1-mAb complex. **(B)** JAM-A binding to immobilized T3D σ1 complexed with 9BG5 mAbs was observed. Control experiments after regeneration of the σ1 surface with 9BG5 Fabs and JAM-A

were performed and showed that similar amounts of JAM-A bound to σ1 alone and to a σ1-mAb complex.

5 Discussion

5.1 The σ1-Tail Domain

5.1.1 Anchoring of σ1 in the Virus

The trimeric reovirus attachment protein σ1 is anchored at the five-fold axis of the virion by interacting with the pentameric λ2 protein. The first N-terminal ~ 25 amino acids of σ1 are thought to contact λ2, and as the sequence possesses a heptad repeat pattern, this part of the protein is predicted to form a small coiled coil that is appended to the rest of the tail domain by a short linker region [60,113].

EM reconstructions of reovirus virions and ISVPs revealed small density features corresponding to σ1 protruding from the center of the λ2 turrets [28]. Comparison of reconstructions of particles that have σ1 bound and particles that lack σ1 showed density features just above and beneath the top of the λ2 turret, indicating that the σ1 anchor is incorporated within the pentameric λ2 protein [114,115]. The density feature of σ1 within the λ2-cavity forms a knob like structure.

A deeper understanding of the structural features underlying the symmetry-mismatch, the unusual interaction between the pentameric λ2 and the trimeric σ1 proteins, would shed light on assembly and disassembly processes of the virus. To investigate whether the N-terminus of σ1 has a defined structure in the absence of λ2, a crystal structure of a T3D σ1 construct comprising residues 1-168 was solved. The σ1 trimer is formed by crystallographic three-fold symmetry, but there is no electron density visible for the residues of interest (amino acids 1-24). This finding indicates that this part of the protein is either too flexible or unstructured to be resolved in the electron density. It is therefore impossible to say whether the N-terminus of σ1 is structured or not.

It is possible that the six non-native amino acids at the N-terminus of σ1, a remnant from cloning, influence the σ1 structure. Therefore, and also to compare the findings with T1L σ1, a new construct, SUMO-T1L σ1(2-178), was cloned and is currently under investigation. This construct has the advantage that, after tag-cleavage with the protease UlpI, no additional non-native amino acids remain appended to the σ1 protein.

It is unlikely that the coiled coil region of the tail domain (amino acids 25 onwards) found in the T3D σ1(1-168) structure would correspond to the knob-like density feature within the λ2-cavity as the opening of λ2 spans only ~ 15 Å, while the coiled coil has a diameter of ~ 25 Å. It remains possible that the N-terminal region of σ1 requires an interaction with

λ2 to become folded and that the small predicted coiled coil corresponds to the knob-like density observed by EM analysis, while the flexible linker penetrates the λ2 channel.

The current model predicts that σ1 cannot escape λ2 in virions and ISVPs, as the channel at the center of λ2 is too narrow. During ISVP-to-core transition, λ2 undergoes a conformational change that increases the width of the channel allowing release of σ1 that poorly binds to cores [28]. The recoating of cores with μ1/σ3 causes λ2 to rearrange into its closed conformation. Except for the appearance of the knob-like density, recoating with additional σ1 does not induce further major changes in the capsid. Therefore, it is hypothesized that σ1 assembles before or in concert with μ1/σ3 [115]. An experiment, such as adding μ1/σ3-recoated core particles to σ1 containing cell lysate and testing for σ1 insertion would be informative.

The λ2 protein forms solely monomers when it is expressed alone and requires the scaffold of the core to form pentamers. To strengthen the model that σ1 is incorporated into λ2 pentamers, and to further investigate the symmetry mismatch, one could recoat core particles with μ1/σ3 and shorter σ1 proteins containing photo-reactive amino acids at the N-terminus for site-specific cross-linking. Photo-reactive unnatural amino acids such as photo-Met or photo-Leu could be incorporated into σ1 either during recombinant protein production or via peptide synthesis [116,117]. Other photo-reactive amino acids such as *p*-benzoyl-L-phenylalanine, which can be incorporated into biomolecules by genetic code expansion methods, might be too bulky for this experiment. Furthermore, the heterologous production of the σ1 tail yields high protein amounts and enables recombinant modifications, e.g., the specific introduction of cysteine residues for labeling with Alexa fluorophores for FRET-based approaches, that might be useful to determine whether the N-terminus of σ1 has a defined structure. NMR spectra of T1L σ1(2-178) and NMR spectra of T3D σ1(1-168) compared with T3D σ1(25-168), which both have the same six non-native amino acids, would be a different and more elegant way to determine whether the σ1 N-terminus is structured.

Reovirus σ1 and adenovirus fiber share functional and structural properties [63]. Both proteins mediate cell-attachment, possess a fibrous domain composed of triple β-spiral repeats, have a globular head domain, and are associated with the virus at the icosahedral vertices. However, most data suggest that the two trimeric proteins have different approaches to encounter the ‘3-5’ symmetry-mismatch. The virus-anchoring region of adenovirus fiber is larger than the expected region of σ1 and has in comparison no predicted secondary structure but a highly conserved region among the adenovirus serotypes. Compared to σ1, adenovirus fiber is thought to interact at the outer surface of

the pentameric vertex-protein using monomeric “cables” for binding between two subunits. Several EM analyses of adenoviruses and crystal structures of the pentameric protein complexed with fiber peptides support this model [64,118]. However, one crystal structure of a chimeric virus exists that reveals electron density proposed to belong to the fiber within the central cavity of the pentameric protein [119]. This interaction was suggested to represent an intermediate state during virus cell entry or assembly [118,119].

5.1.2 The σ1 Coiled Coil

Prior to this work, crystal structures of only two small regions of the T1L σ1 tail (residues 29-78 and 120-160) that are both N- and C-terminally flanked by $(GCN4)_3$ were known (Reiss, Dissertation, 2013). To investigate whether the σ1 tail can independently form a stable trimeric coiled coil or whether its trimeric structure is enforced by the trimerization units, longer T1L σ1 constructs with or without a single N-terminal $(GCN4)_3$-motif were purified and crystallized.

The proteins elute from SEC-columns at retention volumes corresponding to globular proteins of higher molecular weight, reflecting a large hydrodynamic radius due to the rigidity of the elongated molecules. The T1L σ1(29-158) protein is stable across broad pH- and temperature ranges, as determined by circular dichroism measurements, indicating that the $(GCN4)_3$-motif is not required for multimerization of the protein. Both crystal structures revealed trimeric helical bundles with two chloride ions bound in the center of the coiled coil.

Superpositions of the σ1 structure lacking $(GCN4)_3$ with the σ1 structures containing $(GCN4)_3$ yield high r.m.s.d. values (Table 5.1). The extent of the deviation is higher for the longer constructs. This finding indicates that the trimerization unit constrains the σ1 structure, causing deviations of the winding that add up along the α-helix and casts doubt on the usefulness of the fusion-tag in this particular case. However, differences in crystal packing and crystal contacts also might influence the winding.

In comparison, the tail domain residues that are defined well in the electron density (residues 29-95, chain A) of the two T3D σ1 crystal structures, T3D σ1(1-168) and T3D σ1(25-291), that do not contain a $(GCN4)_3$-motif and differ in the space group and crystal contacts, align with an r.m.s.d. value of 0.26 Å (main chain) or 0.54 Å (all atoms).

Table 5.1 Superposition of the untagged σ1 protein with $(GCN4)_3$-carrying fragments of T1L σ1 tail domain structures. Coordinates of similar σ1-residues were superimposed by LSQ (chain A only) or SSM superpose (chain ABC).

T1L σ1(29-159)	Main chain (chain ABC)	Main chain (chain A)	All atoms (chain A)
$(GCN4)_3$-T1L σ1(120-160)-$(GCN4)_3$	1.37 Å	0.65 Å	1.24 Å
$(GCN4)_3$-T1L σ1(29-78)-$(GCN4)_3$	-	0.90 Å	1.52 Å
$(GCN4)_3$-T1L σ1(29-158)	2.50 Å	1.78 Å	2.15 Å

Interhelical salt bridges between positions *g* and *e+1* contribute approximately 1.5 kJ/mol to the coiled coil stability, and the charge patterns at those positions influence the preference for homo- or heterotypic or parallel or antiparallel pairing as well as the oligomerization state of an α-helical bundle [120,121].

The coiled coils of T1L σ1(29-158) and T3D σ1(25-291) are stabilized by several interhelical salt bridges along the σ1 tail domain (Figure 5.1, Appendix helical wheel). For the T3D σ1 structure, all predicted charge-mediated interactions between adjacent α-helices are present, while for the T1L σ1 structures, two such interactions are not part of the construct, one formed between E27 and K32 at the N-terminus, and one formed between R171 and E176 at the C-terminus of the tail.

Few interhelical salt bridges involve residues at positions other than *g* and *e+1*, such as the interaction between R153 and D155 of T1L σ1 or between E159 and R161 of T3D σ1. These interactions are likely made possible by the locally altered geometry caused by the stutter. The interaction between R120 and D122 of T3D σ1 that occupy *e* and *g* positions of the same heptad is likely linked to the presence of H123 at the following core position. The histidine side chain is bulky and hydrophilic and leads to a local increase of the coiled coil pitch, making a salt bridge between R120 and D122 possible.

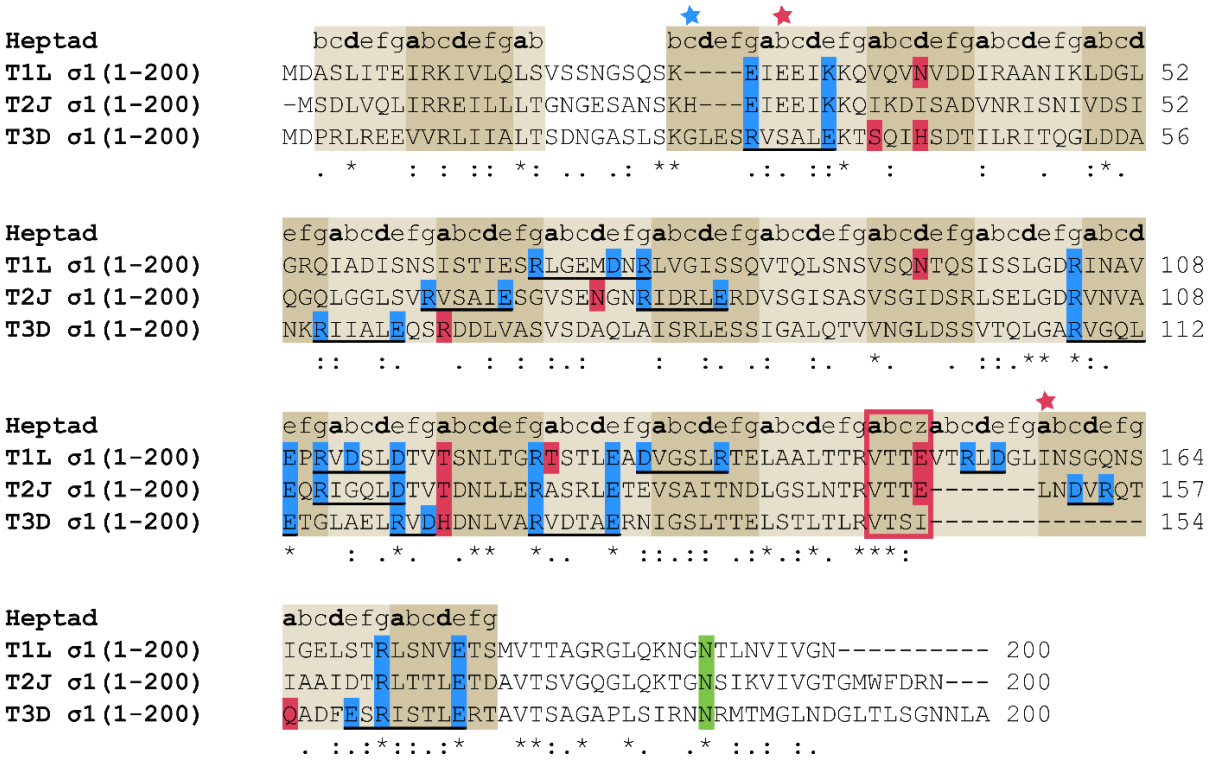

Figure 5.1 Amino acid sequence alignment of residues 1-200 of T1L, T2J, and T3D σ1. The heptad repeats $(abcdefg)_n$ of the tail domain are indicated and highlighted in alternating light and dark brown shading. Typically hydrophobic positions *a* and *d* are bold. Red asterisks mark the start and end of T1L σ1(29-158), and a blue asterisk marks the N-terminal start of T3D σ1(25-291). Charged residues that form interhelical salt bridges of adjacent α-helices are highlighted in blue, and the acid base pairs are connected by underlines. The stutter is framed with a red box. Hydrophilic residues that occupy positions *a* and *d* are highlighted in red. A conserved Asn residue of the body domain is highlighted in green.

The hydrophobic core provides the largest contribution to the overall stability of an α-helical bundle [120]. In most coiled coils, a small percentage of polar core residues are present that add oligomerization and orientation specificity at the expense of stability. Here, T1L σ1 harbors two threonines at *a* positions and two asparagines at *d* positions, while T3D σ1 has a serine, two histidines, and an arginine at *a* and *d* positions. The main electron density for the arginine (R67) is shifted to the outside of the core and forms a hydrogen bond with S66 of an adjacent α-helix (Figure 5.2). Little density is present in the core of the 2.25 Å resolution structure of T3D σ1(25-291), while the unbiased F_o-F_c electron density map of the 1.6 Å resolution structure of T3D σ1(1-168) indicates alternative conformations for R67, so that one arginine in one of the three chains at a time is present in the core (Figure 5.2).

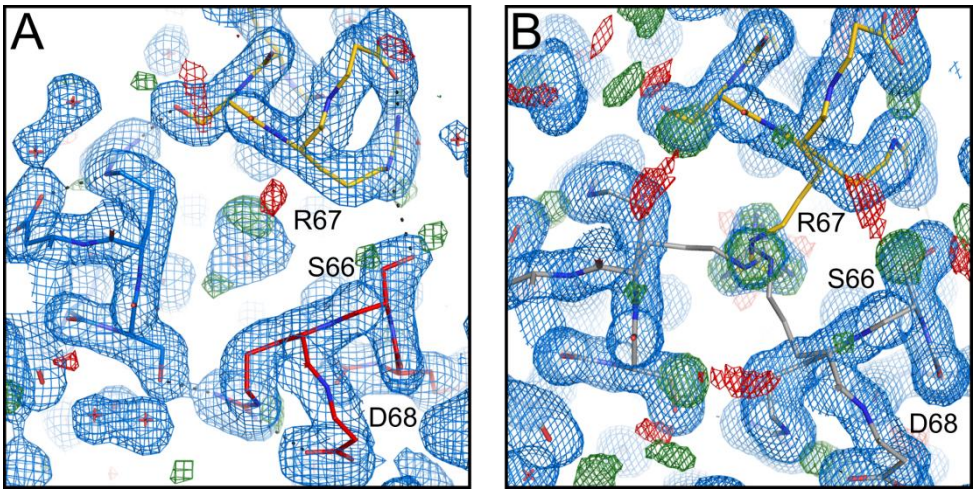

Figure 5.2 Residue R67 of T3D σ1 occupies a typically hydrophobic *a* position. Close up view along the three-fold axis. The σ1 chains are colored in blue, red, and yellow in the 2.25 Å resolution structure of T3D σ1(25-291) **(A)** and yellow and grey (symmetry mates) in the 1.6 Å resolution structure of T3D σ1(1-168) **(B)**. The $2F_o$-F_c electron density map is contoured in blue at 1.0 σ, and the F_o-F_c map is contoured in green at 3.0 σ and in red at -3.0 σ. The residue R67 is shifted out of the core and towards the surface of the coiled coil, where it interacts with S66 of an adjacent α-helix. Unbiased electron density inside the core indicates an alternative conformation of R67 that is modeled in (B) and shows that one R67 residues at a time can be present inside the core.

Acidic and basic amino acids that occupy core positions play important roles in the pH-dependent structural rearrangements of known coiled coil-containing proteins, such as influenza hemagglutinin or macrophage scavenger receptor [122,123]. Peptides composed of 4-5 heptad repeats with amino acid substitutions of Glu or His at core positions were investigated for pH-induced conformational changes [124,125]. At certain pH values, these residues are charged causing interhelical electrostatic repulsion at the core that destabilizes the coiled coil and leads to a random structure.

Of the three reovirus serotypes, only T3D σ1 possess basic histidines at core positions that point inside. CD measurements of the tail domain could indicate a pH-dependent influence on the coiled coil structure. However, as the histidines are separated from each other by eleven heptad repeats it is likely that a destabilization at low pH will be compensated by the surrounding helices. The other two serotypes do not have charged residues at similar locations and, thus, it seems unlikely that the histidines play a crucial role in the assumed conformational rearrangement of σ1.

Histidines within a helical bundle can function as ligands for various ions [126,127]. Only water molecules are bound within the T3D σ1 protein structure. It is possible that a different crystallization condition or metal ion soaking of the obtained crystals would reveal a structure with bound ions.

T1L σ1 harbors two and T2J σ1 harbors one asparagine at *d* positions. The asparagines of T1L σ1 coordinate halogenide ions in the hydrophobic core, a characteristic property that has been observed in other trimeric coiled coils [128]. Asparagines at the core positions that have been substituted with hydrophobic amino acids in other coiled coil structures led to a loss of structural specificity. The asparagines present in T1L σ1 and T2J σ1 also might act as additional trimerization determinants necessary for proper assembly of the α-helical bundle. Residue H42 of T3D σ1 is located at a position similar to N38 of T1L σ1, and it also might influence the trimeric aligning of the σ1 subunits.

Uninterrupted heptad repeats are predominantly found in short coiled coil structures, e.g., in transcription factors, while heptad breaks (stutter, stammer) are encountered in many longer coiled coil domains [68]. These discontinuities can be tolerated by a local distortion of the geometry that is generally confined to two α-helical turns on both sides of the heptad break [69,120]. The local geometry change is assumed to either terminate the structural motif or contribute to the flexibility of longer coiled coil structures. Heptad breaks can modify the assembly of a protein and its interaction properties, as was shown in an analysis of a stutterless vimentin [129]. Stutter positions also are highly conserved in many viral fusion proteins, suggesting a functional role in proteins that often adopt different conformations.

In the σ1 proteins of all three serotypes, the stutter position close to the C-terminal end of the coiled coil is conserved. Following the stutter, T1L σ1 has two heptad repeat insertions and T2J σ1 has one heptad repeat insertion relative to T3D σ1. The stutter sequences lead to a local unwinding of the coiled coil and the α-helices in the T1L σ1 and T3D σ1 structures. This unwinding causes the formation of a *da*-layer, and a hydrophilic interaction between the conserved threonine at position *b* of the stutter and the conserved arginine (position *g-1*) of an adjacent α-helix.

To further define the role of the observed features of the T1L σ1 and T3D σ1 tail domains, mutant σ1 proteins were engineered. In T1L σ1, the core asparagines were replaced with hydrophobic amino acids, and in T3D σ1, stutterless tail domains were engineered through either an insertion of three additional amino acids or a deletion of the four stutter residues. Mutant viruses were recovered using the reverse genetics approach, and their viral attachment and cell entry properties are currently being analyzed to define the effect of the engineered mutations in a physiological setting. This analysis also may reveal whether the ions in the core or the conserved stutter serve crucial roles in σ1 function.

5.2 The σ1 Tail-Body Junction

EM images of the σ1 protein isolated from virions by mild heating show three regions of greater flexibility, one close to the N-terminus, one at the midpoint of the molecule that correlates with the junction of the tail and the body domain, and one close to the head domain [61]. These flexible parts could facilitate a structural rearrangement of σ1 during viral disassembly or assembly.

The region just below the head was indeed shown to be flexible by previous crystallographic analyses of σ1 [63]. To investigate the remaining two regions of predicted flexibility, T1L and T3D σ1 proteins comprising these regions were purified and crystallized. As discussed above, the N-terminal part of the T3D σ1(1-168) structure is not resolved in the electron density, likely because of its highly flexible nature or conformational heterogeneity.

The structure of T3D σ1(25-291) comprises the tail and a portion of the body domain and reveals a seamless transition of the two domains. Backbone-backbone interactions between valines V170 of the three chains at the transition site and direct interactions between N182 of the body and carbonyl groups of E166 and A169 at the end of the coiled coil stabilize the junction of the two domains. Thus, the structure does not readily explain the flexibility at the midpoint of σ1 observed in the EM images.

The valine and threonine at the domain junction, as well as the asparagine that interacts with the coiled coil, are also conserved in the body domains of T1L and T2J σ1 (Figure 5.1, page 74). An interhelical salt bridge that stabilizes the C-terminal end of the T3D σ1 coiled coil is also predicted in the sequence of the other two serotypes. Therefore, it is likely that the transition of the tail to the body domain of T1L and T2J σ1 is similar to the T3D σ1 structure.

In T1L σ1, a methionine is located at the end of the coiled coil (analogous to A169 of T3D σ1), and the presence of this larger residue might lead to a larger coiled coil diameter at the transition site compared with T3D σ1. X-ray diffraction data were obtained for crystals of a T1L σ1 construct comprising the coiled coil and a portion of the body domain, and the data are currently being processed. The crystal structure of this protein will likely elucidate features of the tail-body junction in T1L σ1 and clarify whether its structure is indeed similar to T3D σ1.

The structural information obtained for T3D σ1(25-291) can be combined with the known T3D σ1 structure consisting of the body and the head domain (PDB ID: 3S6X). The main chains of the body domain present in both structures align with a low r.m.s.d value of

0.34 Å (all atoms: 0.63 Å) and result in a high-resolution model of σ1 that fits well with the elongated EM reconstruction of full-length T2J σ1 (Figure 5.3).

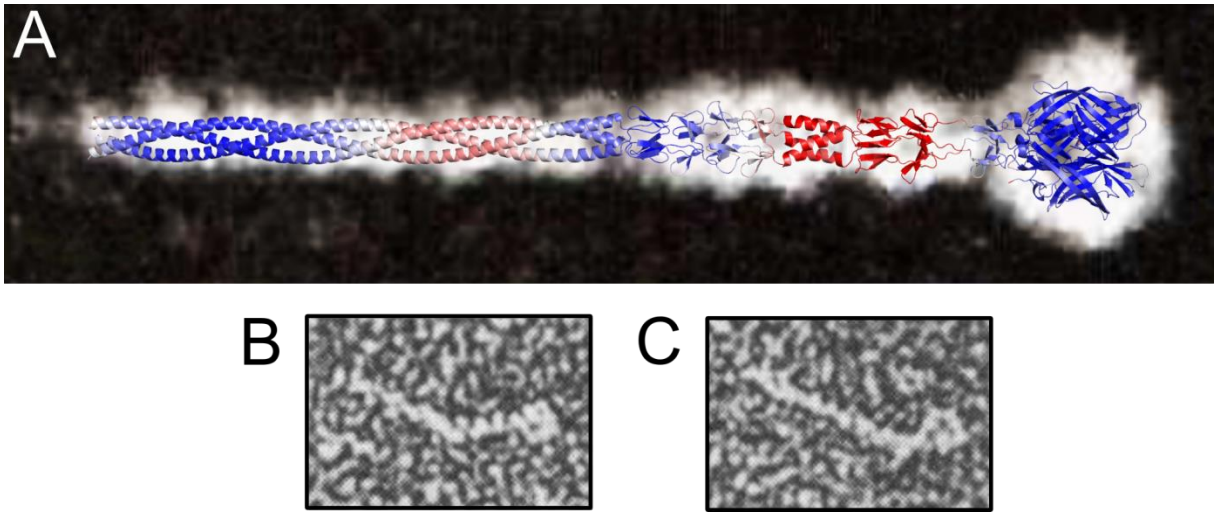

Figure 5.3 Model of T3D σ1 superimposed on a computer-processed electron micrograph of T2J σ1. (A) The T3D σ1 model is assembled by combining the residues 27-243 of the T3D σ1(25-291) structure with residues 244-455 of PDB ID: 3S6X (after alignment of the identical parts of the body domain). Both structures used for the model have a resolution of 2.25 Å. The model is colored according to B-factors from blue (20 $Å^2$) to red (120 $Å^2$). The T3D σ1 model is superimposed onto a computer-processed electron micrograph of T2J σ1 adapted from [61]. **(B, C)** Electron micrographs of T2J σ1 molecules isolated from virions show kinks at two different region of the molecule [61]. Figure used with permission.

The head and body domains of σ1 are connected by a linker region that allows movement between the two domains and explains the flexibility of the molecule near the head domain [17,19,63]. Within the T3D σ1(25-291) structure, no such intrinsic flexible region was observed that could account for the flexibility in the middle of the σ1 protein. Instead, it is possible that conformationally distinct, stable states of σ1 exist in which the tail and body have different but defined orientations.

In the study of Fraser *et al.* [61], just a minor fraction (2-4%) of the σ1 particles showed kinks near the midpoint of the molecule. This rare observation could be an artifact, a result of the harsh sample preparation that included heating of the virus to 52°C for 30 min (to release σ1) and negative staining using uranyl formate that might affect the protein structure. The comparison with EM micrographs of recombinant σ1 could give some more hints about the flexibility of the molecule. Therefore, the T1L and T3D σ1 constructs of different lengths that comprise the coiled coil tail and parts of the body domain, as well as T1L σ1(29-470) that is composed of the tail, body, and head domains, might be useful. The initial purification test of SUMO-T1L σ1(2-470) looked promising,

and it is probably worthwhile to investigate this construct further. In comparison to the untagged T1L σ1(29-470) protein, the construct possesses additional N-terminal amino acids, and the purification could be simpler and less time-consuming.

The contribution of direct body-tail domain interactions to the stability of σ1 and the effect of the interhelical salt bridge at the end of the coiled coil could be investigated with mutant σ1 proteins in the proposed EM study. Proteins that are more flexible at the midpoint of the molecule might increase the percentage of kinked or bent structures within the sample.

To investigate whether the observed tight and stable transition of the two domains has an influence on the function of σ1, mutant T3 reovirions with alterations in the tail, such as a N182A point mutation, have been recovered and will be tested for attachment, internalization, disassembly, and membrane penetration.

While the B-factors for residues at the tail-body junction are low in the T3D σ1(25-291) structure, the residues that belong to the small coiled coil that directly follows β-spiral repeat β4 have negligable electron density and high B-factors. The T3D σ1(170-455) structure of PDB ID 3S6X has similar low B-factors for the N-terminal part of the body domain (β1-β4) and high B-factors for the small coiled coil and the following β-spiral repeats β5-β7 (Figure 5.3). Higher temperature factors indicate a higher degree of thermal mobility within a molecule or regions that are involved in fewer crystal contacts.

The susceptibility of T3D σ1 to protease cleavage within the coiled coil of the body domain and the finding that the point-mutation T249I, which has a stabilizing effect on the coiled coil, renders the protein resistant to proteolytic cleavage is a further indication for some flexibility in this region.

Due to the low resolution and signal-to-noise ratio of the EM micrographs in the Fraser *et al.* study [61] and the low percentage of particles kinked in the middle of the fiber, determination of the region of higher flexibility is somewhat imprecise. New EM images of σ1 with a better resolution could better define locations of flexibility.

The evidence that σ1 undergoes an extensive structural rearrangement is based on prior EM studies [28,29], and further experiments are required to support this hypothesis. Assuming that σ1 has a defined and compact conformation on virions, complexes with σ1 specific antibodies, such as 9BG5 or 5C6, would trap σ1 and reveal a defined pattern of the mAbs on the virus surface on EM images. If it is indeed the case that σ1 has a linear, elongated structure when present on ISVPs but is non-linear and hidden on the virus surface due to possible interactions with σ3 or σ3/μ1, complexes with σ1-specific mAbs would reveal a non-uniform pattern of mAb-spiked particles.

5.3 σ1 Interactions with Neutralizing Antibodies

5.3.1 Strategies for Viral Escape from Antibody Neutralization

Previous analysis of reovirus variants that resist neutralization of 5C6 or 9BG5 have identified two residues in the T1 and T3 σ1 head domains critical for antibody recognition [92,98]. The crystal structures of complexes between T1L σ1 with 5C6 Fabs and T3D σ1 with 9BG5 Fabs presented here have elucidated the complete antibody-binding sites and provide insights into the strategies by which the reovirus variants escape neutralization.

T1 reovirus variants that are resistant to 5C6 display point mutations Q417K or G447S. Residue $Q417^{\sigma1}$ is engaged by the carbonyl group of 5C6 residue $Y102^{H3}$. The mutation Q417K likely would sterically hinder $Y102^{H3}$ and $Y104^{H3}$ interactions with σ1, and the introduced positive charge next to $R424^{\sigma1}$ might locally alter the σ1 structure due to electrostatic repulsion. $G447^{\sigma1}$ is not directly involved in interactions with 5C6. The effect of mutant G447S on neutralization likely results from a diminished residue flexibility. The larger side chain probably alters the local protein structure and prevents binding of CDR H3 to σ1.

Mutant viruses of T3 that escape 9BG5-neutralization display the single mutation D340V or E419K and are less neurovirulent in mice than the wildtype virus, suggesting that a step in the viral life cycle is altered by these mutations. The mutation D340V introduces an aliphatic amino acid that results in the loss of the charge-mediated interaction with $R51^{L2}$ of 9BG5. Residue $E419^{\sigma1}$ forms several hydrogen bonds with 9BG5. The mutation E419K inverts the residue charge and likely weakens the interaction with 9BG5 due to direct disruption of contacts with 9BG5 residues $S30^{L1}$, $S31^{L1}$, and $N32^{L1}$.

5.3.2 Effects of 5C6 and 9BG5 on σ1-Binding to Glycan Receptors

Reoviruses are thought to use an adhesion-strengthening mechanism for cell-attachment in which low-affinity binding of σ1 to cell-surface glycans is followed by high-affinity binding to JAM-A. The glycan binding site of T1L σ1 is located in the head domain and is in direct proximity to the 5C6 epitope (Figure 5.4). Residues $Q371^{\sigma1}$ and $T373^{\sigma1}$ are part of the GM2 glycan binding site as well as the 5C6 epitope of T1L σ1. The location of CDR H1 reduces the available space at the carbohydrate binding site and could therefore directly block low-affinity engagement of the glycan receptor (Figure 5.4C).

Hemagglutination (HA) inhibition assays showing that 5C6 mAbs and Fabs efficiently block T1L virions and ISVPs to agglutinate human erythrocytes substantiate this finding.

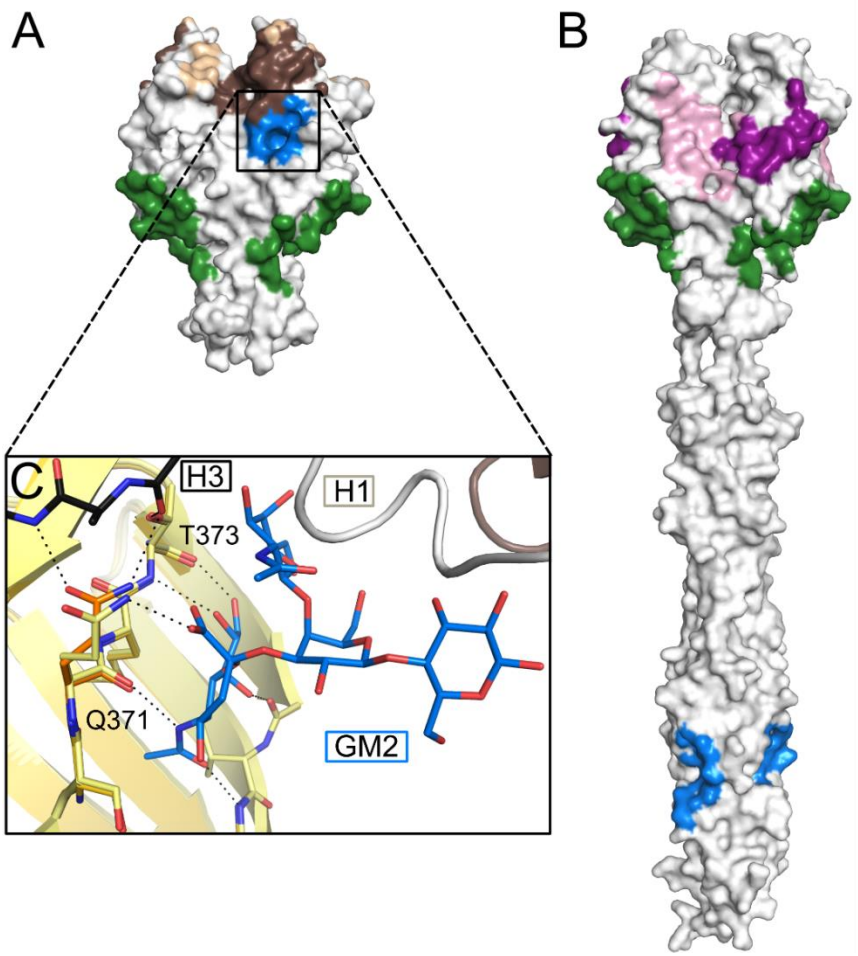

Figure 5.4 Receptor and antibody binding sites on T1L and T3D σ1. Surface representation of σ1 structures. Residues that contact receptors and the mAb within a distance cutoff of 5 Å are colored. The JAM-A binding sites are shown in green, glycan binding sites are blue, the 5C6 epitope is colored in light (light chain) and dark (heavy chain) brown, and the 9BG5 epitope is colored in light (light chain) and dark (heavy chain) violet. **(A)** T1L σ1 head. **(B)** T3D σ1 body and head. **(C)** Close up view showing that the 5C6 epitope overlaps with the glycan binding site of T1L σ1. The residues $Q371^{\sigma1}$ and $T373^{\sigma1}$ interact with GM2 (blue) as well as with CDR H3 (black) of 5C6. The CDR H1 (light grey) occludes the glycan receptor binding site and would hinder GM2-binding due to the reduced space of the receptor binding site.

The carbohydrate binding site of T3D σ1 is located at the N-terminal part of the body domain, while the 9BG5 epitope is located in the head domain (Figure 5.4B). Therefore, it would not be anticipated that 9BG5 binding would directly interfere with sialic acid engagement.

In HA inhibition assays, 9BG5 mAbs and Fabs efficiently block HA by $T3SA^+$ virions, but neither 9BG5 mAbs nor Fabs inhibit HA by $T3SA^+$ ISVPs. This finding supports the

hypothesis that σ1 adopts a more compact conformation on virions than on ISVPs. On a compact virus-bound arrangement, the 9BG5 epitope on the σ1 head could be in close spatial proximity to the carbohydrate-binding site on the σ1 body domain and would thus be able to interfere with glycan receptor engagement. During virion-to-ISVP conversion, σ1 likely adopts the elongated conformation observed in the crystal structure [19], where the 9BG5 epitope is sufficiently distant to the glycan-binding site (~120 Å) such that an IgG molecule probably could not sterically hinder binding of σ1 to the glycan receptor.

5.3.3 Effects of 5C6 and 9BG5 on σ1-Binding to JAM-A

The binding site of the serotype-independent receptor JAM-A is conserved in T1 and T3 reoviruses and located at the lower part of the σ1 head domain (Figure 5.4, page 81). Both the 5C6 epitope that is located close to the top of the σ1 head and the 9BG5 epitope in the middle of the σ1 head span two σ1 subunits and are distinct from the JAM-A receptor-binding site.

SPR studies using immobilized σ1 are consistent with this finding and demonstrated that the soluble JAM-A ectodomain can additionally bind to σ1 complexed with 5C6 or 9BG5. This finding indicates that the two mAbs do not neutralize reovirus infection by direct blockade of the JAM-A receptor-binding site.

Reovirus binding to JAM-A expressed on CHO cells is inhibited by the cognate mAbs and Fabs. If σ1 can bind 5C6 or 9BG5 and JAM-A simultaneously, then by what mechanism is the neutralization of reovirus infection by 5C6 and 9BG5 accomplished? The membrane-associated JAM-A protein extends from the cell by about 80-90 Å, and the binding site for σ1 is located on the most membrane-distal Ig-like domain. JAM-A is engaged by σ1 residues on the lower part of the σ1 head, adjacent to the body domain. Modeling indicates that reovirus binding to JAM-A on the cell surface would bring the top of the σ1 head domain into close proximity with the cell membrane (Figure 5.5A).

Up to three mAbs can bind to one σ1 trimer, and taking geometric considerations into account, one antibody can engage one binding site of one σ1 molecule with one Fab but would not be able to engage the same trimer by binding another epitope with the second Fab. A σ1-bound mAb could probably not bind with its second Fab to a different σ1 protein on the surface of the same virion due to the large distance between the icosahedral five-fold axes. Due to the minor presence of σ1 on the virus particle, binding to a σ1 protein of another reovirus virion (with the second Fab) seems also unlikely to be important for neutralization.

When 5C6 or 9BG5 antibodies bind to σ1, the virus almost certainly could not engage JAM-A, as the membrane-anchored receptor could not reach its binding site on the σ1-surface. The affinity of both 5C6 and 9BG5 Fabs for their cognate σ1 proteins is around 100-fold stronger than the affinity of JAM-A for σ1. Thus, it is unlikely that JAM-A competes for binding to σ1 and suggests that the mechanism of antibody interference with reovirus binding to JAM-A is based on indirect steric hindrance with the cell membrane (Figure 5.5B).

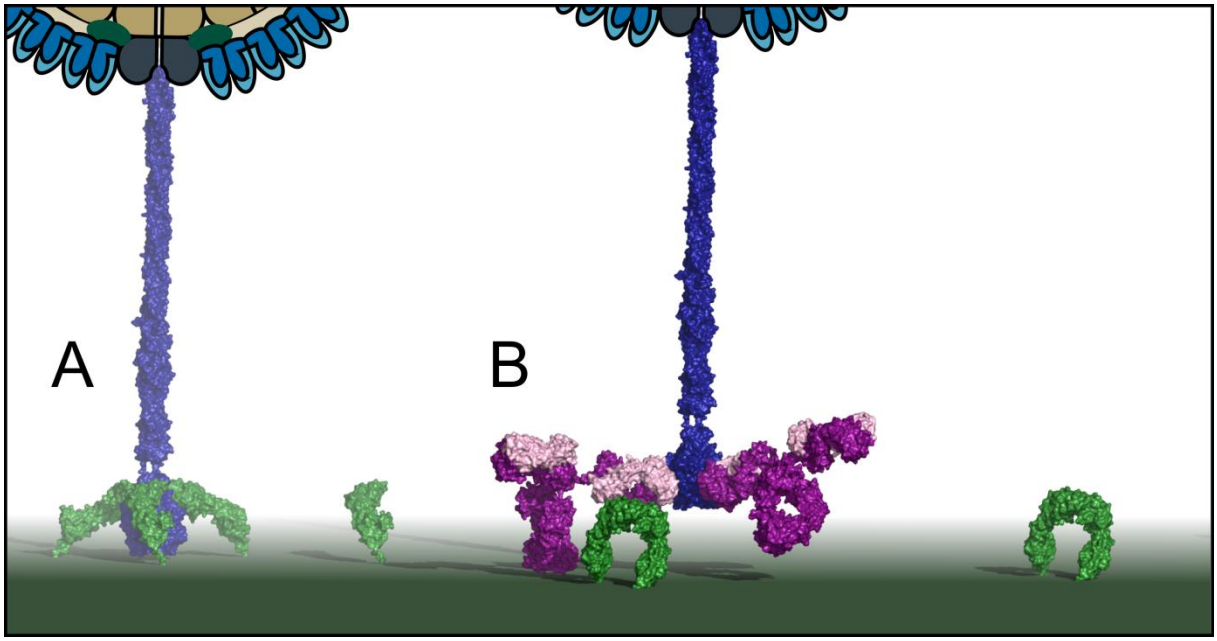

Figure 5.5 Model of the proposed neutralization mechanism of 5C6 and 9BG5 blocking σ1-binding to membrane-associated JAM-A by steric hindrance with the cell-surface. The full-length model of T3D σ1 (PDB ID: 3S6X connected with T3D σ1(25-291)) is colored in blue, the membrane-bound ectodomain of JAM-A (PDB ID: 1NBQ with an additional five amino acids added at the C-terminus using coot) is colored in green, and antibodies (PDB ID: 1IGT, aligned with 9BG5 Fabs via the antigen binding fragments) are colored in light and dark purple. The cell surface is indicated by a plane colored in grey. **(A)** Binding of σ1 to JAM-A on the cell-surface brings the top of the σ1 head in close proximity with the cell-membrane. **(B)** 9BG5-bound σ1 close to the cell surface (for clarity only two mAbs are shown). The bulky antibodies would clash with the cell-surface, impede JAM-A binding.

5.3.4 Neutralization Recognition of other Virus Fiber Proteins

While the mechanism of reovirus neutralization may be mainly explained by interference with receptor binding at the cell surface, it is conceivable that 5C6 and 9BG5 also impair later steps in the infectious cycle. The 5C6 and 9BG5 binding sites are well placed to hinder a possible structural change in σ1 that may be important for reovirus cell-uptake. Both epitopes bridge σ1-subunits and thus are conformationally dependent. Such a binding mode is also shared by neutralizing antibodies directed against stalk-like attachment proteins of other viruses.

The hemagglutinin of influenza virus is a trimeric molecule that consists of a globular head, which mediates binding to cell-surface glycan-receptors, and a stem region, which mediates fusion of the viral envelope with the cellular membrane. Broadly neutralizing mAbs that are directed against the highly conserved stem region of hemagglutinin bind across the two subunits (HA1 and HA2) of a protomer and lock the protein in the pre-fusion conformation. Thus, the mAbs inhibit a conformational change of the protein that is required for membrane fusion [130].

A similar neutralization strategy is observed for rotaviruses, which also belong to the *Reoviridae* family. The rotavirus attachment protein, VP4, is a spike-like molecule that consists of two fragments, VP5* and VP8*, which are generated by proteolytic cleavage [131]. The body of the spike is formed by VP5*, which contains the hydrophobic membrane penetration domain. The distal globular head domain is formed by VP8*, which is involved in carbohydrate-receptor engagement. The core of VP5* has a fold that is similar to that of the head domain of reovirus σ1 [132].

VP4 undergoes a conformational change from a local dimer to a trimer during cell entry. The neutralizing mAb 2G4 binds the dimeric form of VP4 in the cleft between the heads and prevents the irreversible reorganization of the protein to the trimeric state [133]. The binding site of 2G4 was mapped by an escape mutation located in the membrane penetration domain of VP5* [134], but the complete epitope is unknown, and a detailed understanding of the neutralization mechanism is therefore not yet possible. 2G4 also can bind to the trimeric VP4, but it remains possible that the mAb interacts with residues of VP8* and prevents the conformational change by spanning subunits.

Common to these examples is a neutralizing mechanism in which the mAbs bind across subunits of a multimeric viral attachment protein and thereby stabilize a particular conformation that prevents a structural rearrangement of the protein. The anti-reovirus mAbs 5C6 and 9BG5 share the same, subunit-bridging strategy for binding attachment

protein σ1, suggesting a likely role for a σ1 conformational change during cell entry. In future studies, neutralizing and non-neutralizing mAbs that target σ1 on virions or ISVPs may serve as useful tools to probe the hypothesized, conformational rearrangement.

6 Appendix

6.1 Construct Overview

Construct	$Mw_{monomer}$ [kDa]	ε_{280nm} [$M^{-1}cm^{-1}$]	pI	
SUMO-T1L (2-470)	64 (tagged)	60390	5.3	pE-SUMOpro amp
	51 (untagged)	58900	5.1	
SUMO-T1L (29-470)	61 (tagged)	60390	5.3	pE-SUMOpro amp
	48 (untagged)	58900	5.0	
His_6-T1L σ1(29-470)	51	58900	5.8	pET28b kana
T1L σ1(29-470)	48	58900	5.0	pET16b
His_6-T1L σ1(29-303)	32 (tagged)	9970	5.8	pET28b kana
	30(untagged)	9970	5.0	
His_6-T1L σ1(29-265)	28 (tagged)	8480	6.0	pET28b kana
	26 (untagged)	8480	5.0	
His_6-T1L σ1(29-249)	26 (tagged)	8480	6.0	pET28b kana
	24 (untagged)	8480	5.0	
$(GCN4)_3$-T1L σ1(29-159)	18	1490	4.9	pIBA-GCN4tri-His
T1L σ1(29-159)	14	-	4.7	pET16b
His_6-T3D σ1(28/30-455)	49 (tagged)	39420	5.8	pET28b
His_6-T3D σ1(1-234)	28 (tagged)	-	6.1	pET28b
	26 (untagged)		5.3	
His_6-T3D σ1(1-291)	34 (tagged)	1490	6.1	pET28b
	32 (untagged)	1490	5.3	
His_6-T3D σ1(25-251)	27 (tagged)	-	6.3	pET28b
	25 (untagged)		5.4	
His_6-T3D σ1(25-291)	31 (tagged)	1490	6.3	pET28b
	29 (untagged)	1490	5.5	
His_6-T3D σ1(1-168)	21 (tagged)	-	5.8	pET28b
	19 (untagged)		4.9	

6.2 MALDI-MS: T3D σ1(25-291)

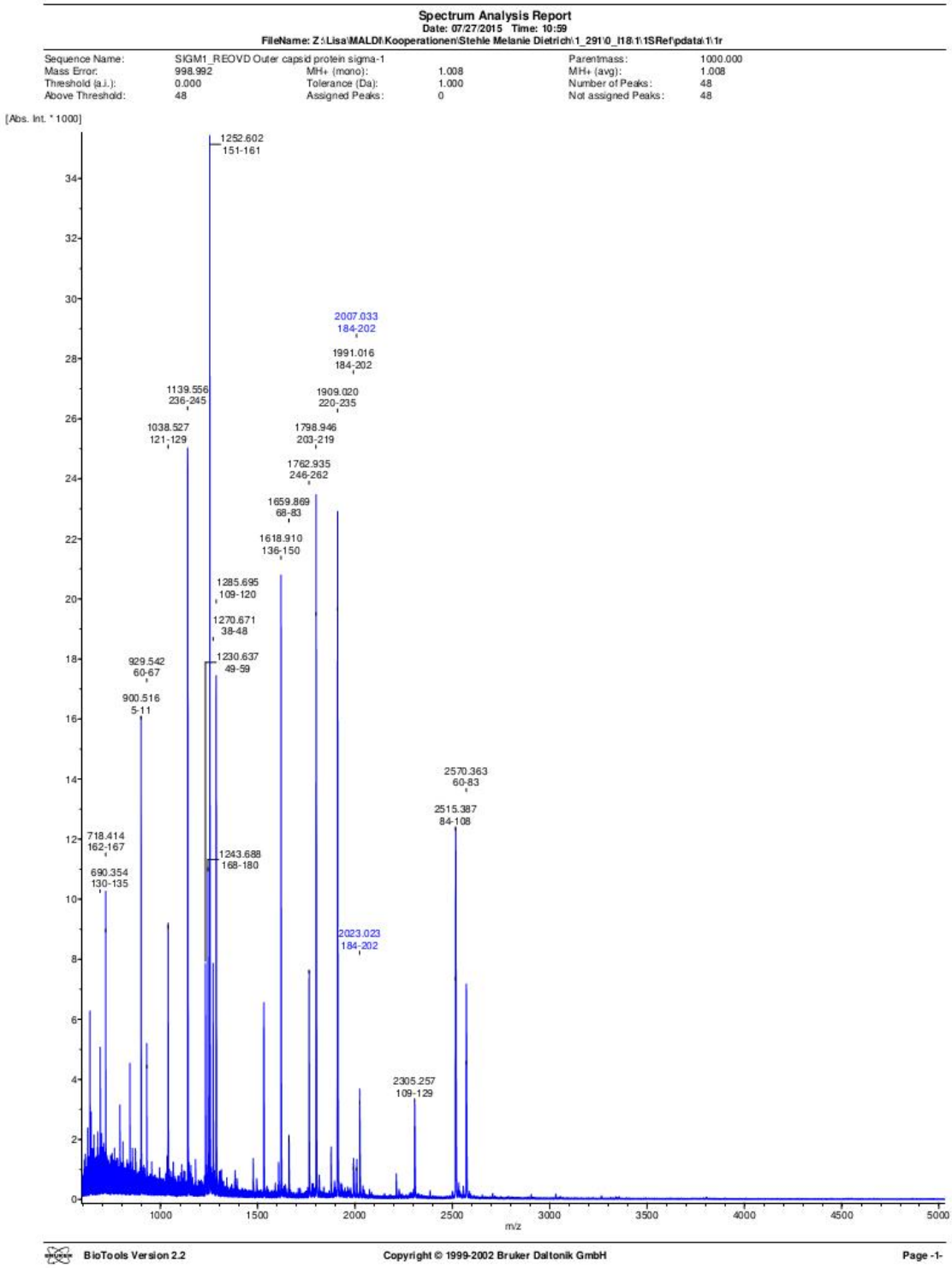

Spectrum Analysis Report

Date: 07/27/2015 Time: 10:59

FileName: Z:\Lisa\MALDI\Kooperationen\Stehle Melanie Dietrich\1_291\0_I18\1\1SRef\pdata\1\1r

Sequence data:

SIGM1_REOVD Outer capsid protein sigma-1

Intensity Coverage:	87.0 % (231921 cnts)	Sequence Coverage MS:	50.3%
Sequence Coverage MS/MS:	0.0%	pI (isoelectric point):	5.0

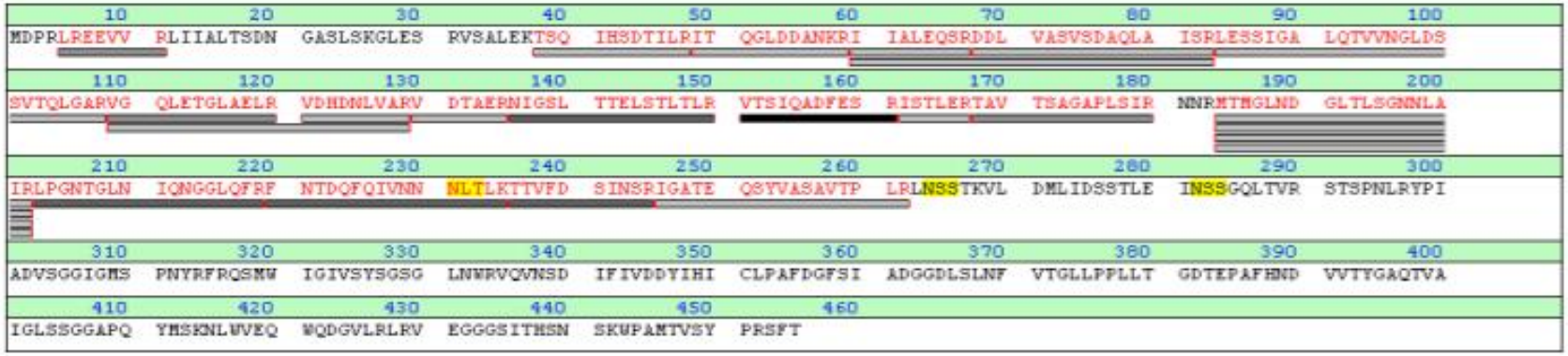

Display Parameter:

Sequence Name:	SIGM1_REOVD Outer capsid protein sigma-1			Parentmass:	1000.000
Mass Error:	998.992	MH+ (mono):	1.008	MH+ (avg):	1.008
Threshold (a.i.):	0.000	Tolerance (Da):	1.000	Number of Peaks:	48
Above Threshold:	48	Assigned Peaks:	0	Not assigned Peaks:	48

Peaklist:

Peak	Mass	Intensity	Peak	Mass	Intensity	Peak	Mass	Intensity
1	625.312	1359.103	2	637.341	5225.835	3	643.057	2075.359
4	659.298	832.581	5	690.354	3963.785	6	718.414	8670.525
7	791.410	2185.086	8	807.407	889.777	9	842.508	3391.521
10	856.510	844.088	11	870.513	881.466	12	900.516	15154.349
13	929.542	4254.823	14	1033.534	724.165	15	1038.527	8788.226
16	1065.518	752.720	17	1139.556	25116.236	18	1146.557	653.850
19	1155.540	591.504	20	1179.605	852.573	21	1230.637	7734.788
22	1243.688	10665.299	23	1252.602	35847.288	24	1270.671	7452.796
25	1285.695	17355.340	26	1313.699	580.197	27	1383.705	692.310
28	1475.760	1089.774	29	1493.763	479.671	30	1530.860	6322.085
31	1606.847	1033.475	32	1618.910	20902.522	33	1659.869	1863.783
34	1762.935	7345.081	35	1798.946	18963.094	36	1815.986	358.368
37	1876.035	1457.076	38	1894.032	343.603	39	1909.020	19123.161
40	1991.016	950.291	41	1993.968	455.154	42	2007.033	932.125
43	2023.023	3080.029	44	2211.111	547.705	45	2305.257	2262.211
46	2515.387	7112.028	47	2554.792	121.400	48	2570.363	4383.543

Mass Differences (da):

N-Term.	Ion	C-Term.	Ion

Matched Sequences:

SIGM1_REOVD Outer capsid protein sigma-1

MDPRLREEVVRLIIALTSDNGASLSKGLESRVSALEKTSQIHSDTILRITQGLDDANKRIIALEQSRDDLVASVSDAQLAISRLESSIGALQTVVNGLDSSVTQLGARVGQLETGLAELRVDHDNLVARVDTAERNIGSLTTE
LSTLTLRVTSIQADFESRISTLERTAVTSAGAPLSIRNNRMTMGLNDGLTLSGNNLAIRLPGNTGLNIQNGGLQFRFNTDQFQIVNNNLTLKTTVFDSINSRIGATEQSYVASAVTPLRLNSSTKVLDMLIDSSTLEINSSGQ
LTVRSTSPNLRYPIADVSGGIGMSPNYRFRQSMWIGIVSYSGSGLNWRVQVNSDIFIVDDYIHICLPAFDGFSIADGGDLSLNFVTGLLPPLLTGDTEPAFHNDVVTYGAQTVAIGLSSGGAPQYMSKNLWVEQWQDGVLRLR
VEGGGSITHSNSKWPAMTVSYPRSFT

Digest Results
Tolerance = 200.000000 ppm, Trypsin/P
Modifications: \NT 1 H Hydrogen, \CT 455 HO Free acid, \MT M O Oxidation (M), \MT C -H+CH2CONH2 Carbamidomethyl (C),

	Mass Mr	Dev.	Range	P	Sequence
*	689.334	0.012	130 - 135	0	VDTAER
*	717.402	0.005	162 - 167	0	ISTLER
*	899.519	-0.011	5 - 11	1	LREEVVR
*	928.534	0.001	60 - 67	0	IIALEQSR
*	1037.525	-0.006	121 - 129	0	VDHDNLVAR
*	1138.562	-0.013	236 - 245	0	TTVFDSINSR
*	1229.636	-0.007	49 - 59	1	ITQGLDDANKR
*	1242.693	-0.012	168 - 180	0	TAVTSAGAPLSIR
*	1251.610	-0.015	151 - 161	0	VTSIQADFESR
*	1269.668	-0.004	38 - 48	0	TSQIHSDTILR
*	1284.704	-0.016	109 - 120	0	VGQLETGLAELR
*	1617.894	0.009	136 - 150	0	NIGSLTTELSTLTLR
*	1658.848	0.014	68 - 83	0	DDLVASVSDAQLAISR
*	1761.926	0.002	246 - 262	0	IGATEQSYVASAVTPLR
*	1797.949	-0.010	203 - 219	0	LPGNTGLNIQNGGLQFR
*	1907.974	0.039	220 - 235	0	FNTDQFQIVNNNLTLK
*	1989.998	0.012	184 - 202	0	MTMGLNDGLTLSGNNLAIR
*	2005.992	0.033	184 - 202	0	MTMGLNDGLTLSGNNLAIR 184: Oxidation (M)
*	2005.992	0.033	184 - 202	0	MTMGLNDGLTLSGNNLAIR 186: Oxidation (M)
*	2021.987	0.028	184 - 202	0	MTMGLNDGLTLSGNNLAIR 184: Oxidation (M) 186: Oxidation (M)
*	2304.219	0.031	109 - 129	1	VGQLETGLAELRVDHDNLVAR
*	2514.329	0.051	84 - 108	0	LESSIGALQTVVNGLDSSVTQLGAR
*	2569.371	-0.016	60 - 83	1	IIALEQSRDDLVASVSDAQLAISR

6.3 Helical Wheel Projections of T1L and T3D σ1 Tail Domain

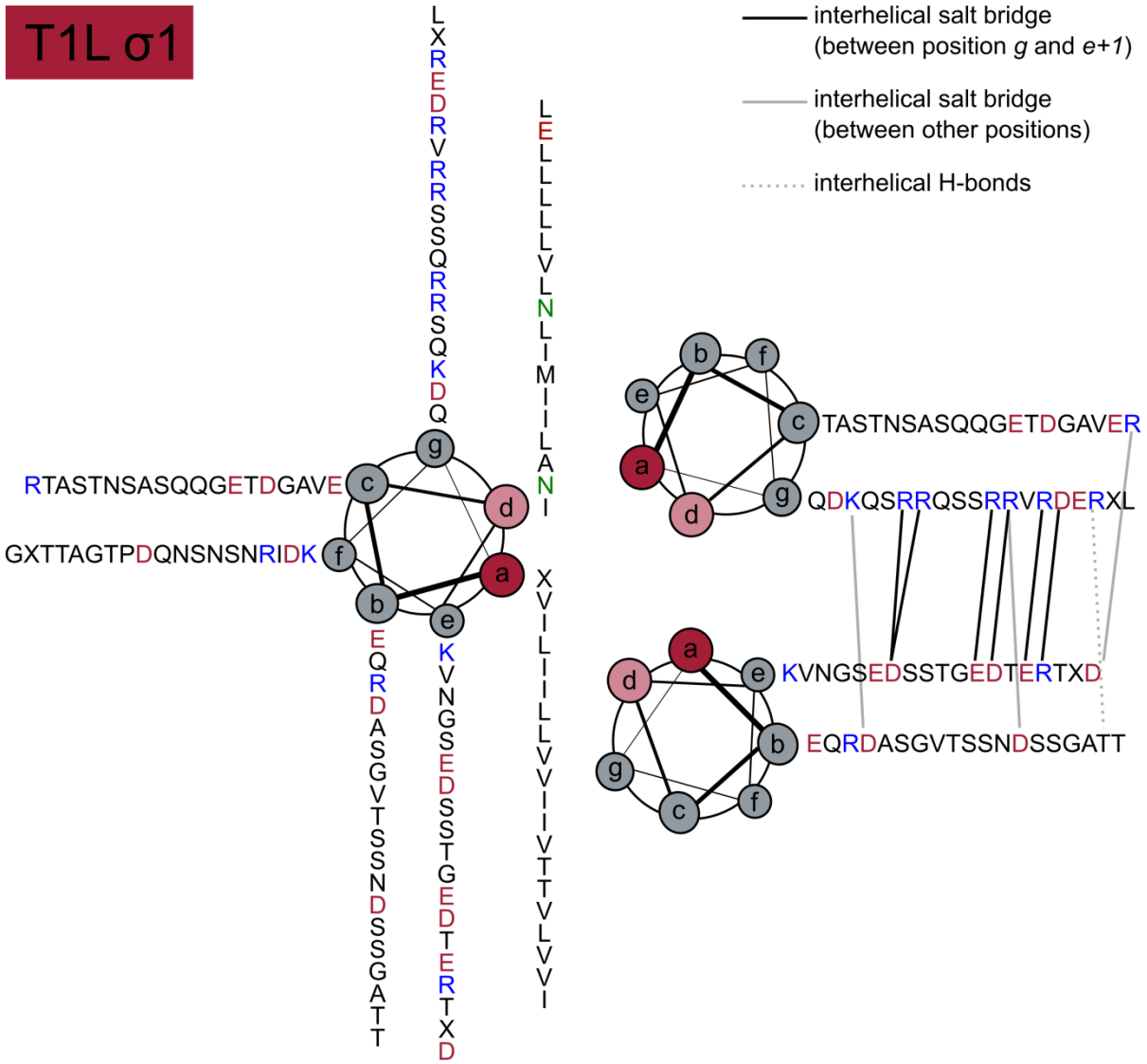

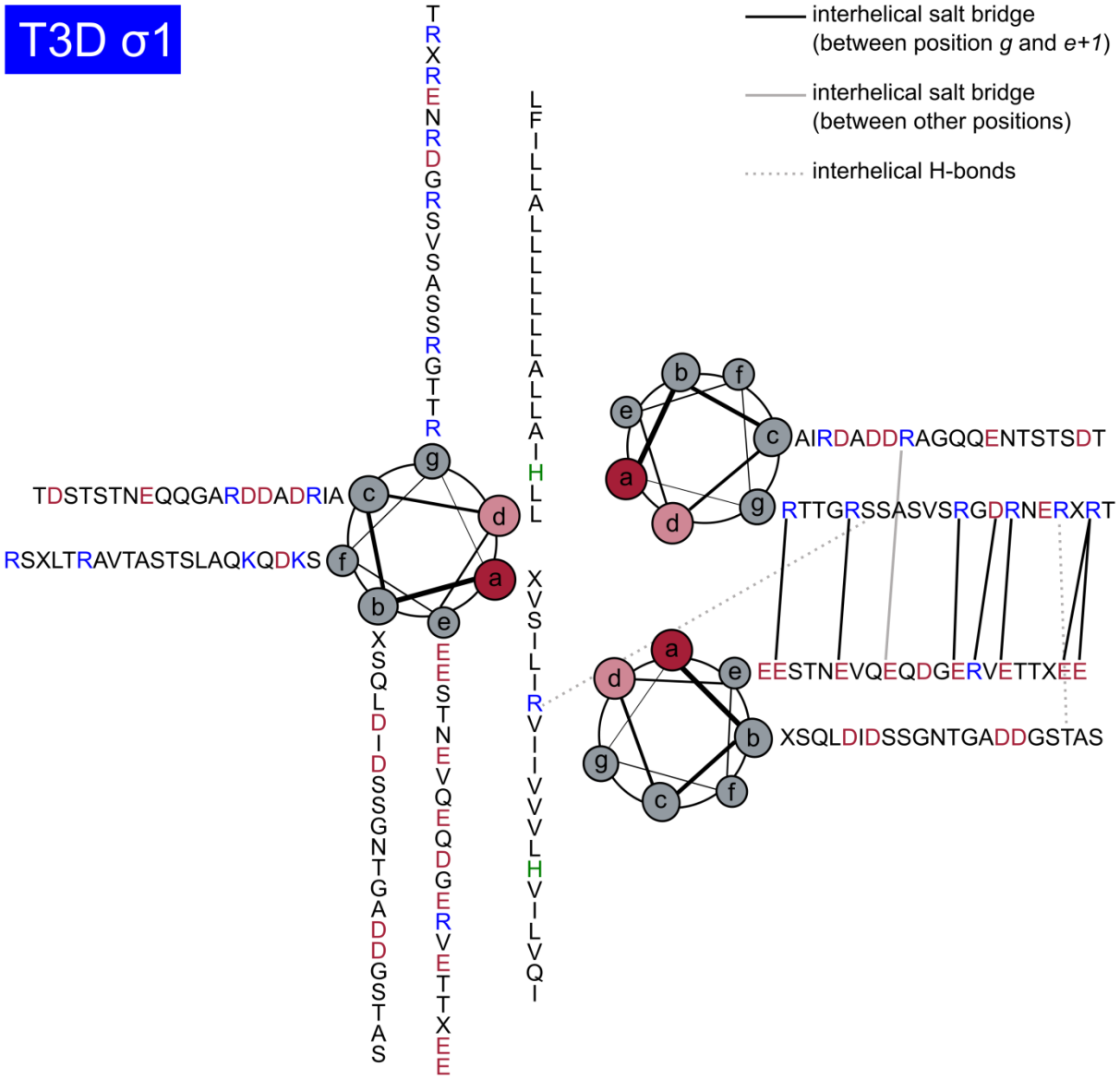
T3D σ1
interhelical salt bridge
(between position g and e+1)
interhelical salt bridge
(between other positions)
interhelical H-bonds
TRXRENRDGRSVSASSSRGTTR
LFILLALLLLLLLLALLAIHLL
TDSTSTNEQQGARDDADRIA
RSXLTRAVTASTSLAQKQDKS
XSQLDIDSSSGNTGADDGSTAS
EESTNEVQEQDGERVETTXEE
XVSILIRVIIVVVLHVILVQI
AIRDADDRAGQQENTSTSDT
RTTGRSSASVSRGDRNERXRT
EESTNEVQEQDGERVETTXEE
XSQLDIDSSGNTGADDGSTAS

7 References

1. Attoui H, Jaafar FM, Belhouchet M, Biagini P, Cantaloube JF, et al. (2005) Expansion of family Reoviridae to include nine-segmented dsRNA viruses: Isolation and characterization of a new virus designated aedes pseudoscutellaris reovirus assigned to a proposed genus (Dinovernavirus). Virology 343: 212-223.
2. Urbano P, Urbano FG (1994) The Reoviridae Family. Comparative Immunology Microbiology and Infectious Diseases 17: 151-161.
3. Sabin AB (1959) Reoviruses. A new group of respiratory and enteric viruses formerly classified as ECHO type 10 is described. Science 130: 1387-1389.
4. Bines JE, Kirkwood CD (2015) Conquering rotavirus: From discovery to global vaccine implementation. Journal of Paediatrics and Child Health 51: 34-39.
5. Banajeh SM, Abu-Asba BA (2015) The epidemiology of all-cause and rotavirus acute gastroenteritis and the characteristics of rotavirus circulating strains before and after rotavirus vaccine introduction in Yemen: analysis of hospital-based surveillance data. BMC Infect Dis 15: 418.
6. MacLachlan NJ, Guthrie AJ (2010) Re-emergence of bluetongue, African horse sickness, and other Orbivirus diseases. Veterinary Research 41.
7. Rosen L (1960) Serologic grouping of reoviruses by hemagglutination-inhibition. Am J Hyg 71: 242-249.
8. Tyler KL, Mcphee DA, Fields BN (1986) Distinct Pathways of Viral Spread in the Host Determined by Reovirus-S1 Gene Segment. Science 233: 770-774.
9. Weiner HL, Drayna D, Averill DR, Fields BN (1977) Molecular-Basis of Reovirus Virulence - Role of S1 Gene. Proceedings of the National Academy of Sciences of the United States of America 74: 5744-5748.
10. Forrest JC, Dermody TS (2003) Reovirus receptors and pathogenesis. Journal of Virology 77: 9109-9115.
11. Mohamed A, Johnston RN, Shmulevitz M (2015) Potential for Improving Potency and Specificity of Reovirus Oncolysis with Next-Generation Reovirus Variants. Viruses-Basel 7: 6251-6278.
12. Reinisch KM, Nibert M, Harrison SC (2000) Structure of the reovirus core at 3.6 angstrom resolution. Nature 404: 960-967.
13. Zhang X, Walker SB, Chipman PR, Nibert ML, Baker TS (2003) Reovirus polymerase lambda 3 localized by cryo-electron microscopy of virions at a resolution of 7.6 angstrom. Nature Structural Biology 10: 1011-1018.
14. Kim J, Parker JSL, Murray KE, Nibert ML (2004) Nucleoside and RNA triphosphatase activities of orthoreovirus transcriptase cofactor mu 2. Journal of Biological Chemistry 279: 4394-4403.
15. Barton ES, Forrest JC, Connolly JL, Chappell JD, Liu Y, et al. (2001) Junction adhesion molecule is a receptor for reovirus. Cell 104: 441-451.
16. Konopka-Anstadt JL, Mainou BA, Sutherland DM, Sekine Y, Strittmatter SM, et al. (2014) The Nogo Receptor NgR1 Mediates Infection by Mammalian Reovirus. Cell Host & Microbe 15: 681-691.
17. Reiss K, Stencel JE, Liu Y, Blaum BS, Reiter DM, et al. (2012) The GM2 Glycan Serves as a Functional Coreceptor for Serotype 1 Reovirus. Plos Pathogens 8.
18. Gentsch JR, Pacitti AF (1987) Differential Interaction of Reovirus Type-3 with Sialylated Receptor Components on Animal-Cells. Virology 161: 245-248.

19. Reiter DM, Frierson JM, Halvorson EE, Kobayashi T, Dermody TS, et al. (2011) Crystal Structure of Reovirus Attachment Protein sigma 1 in Complex with Sialylated Oligosaccharides. Plos Pathogens 7.
20. Barton ES, Connolly JL, Forrest JC, Chappell JD, Dermody TS (2001) Utilization of sialic acid as a coreceptor enhances reovirus attachment by multistep adhesion strengthening. Journal of Biological Chemistry 276: 2200-2211.
21. Maginnis MS, Forrest JC, Kopecky-Bromberg SA, Dickeson SK, Santoro SA, et al. (2006) beta 1 integrin mediates internalization of mammalian reovirus. Journal of Virology 80: 2760-2770.
22. Maginnis MS, Mainou BA, Derdowski A, Johnson EM, Zent R, et al. (2008) NPXY motifs in the beta 1 integrin cytoplasmic tail are required for functional reovirus entry. Journal of Virology 82: 3181-3191.
23. Mainou BA, Dermody TS (2012) Transport to Late Endosomes Is Required for Efficient Reovirus Infection. Journal of Virology 86: 8346-8358.
24. Sturzenbecker LJ, Nibert M, Furlong D, Fields BN (1987) Intracellular Digestion of Reovirus Particles Requires a Low Ph and Is an Essential Step in the Viral Infectious Cycle. Journal of Virology 61: 2351-2361.
25. Doyle JD, Danthi P, Kendall EA, Ooms LS, Wetzel JD, et al. (2012) Molecular Determinants of Proteolytic Disassembly of the Reovirus Outer Capsid. Journal of Biological Chemistry 287: 8029-8038.
26. Mainou BA, Dermody TS (2012) In Search of Cathepsins: How Reovirus Enters Host Cells. DNA and Cell Biology 31: 1646-1649.
27. Johnson EM, Doyle JD, Wetzel JD, McClung RP, Katunuma N, et al. (2009) Genetic and Pharmacologic Alteration of Cathepsin Expression Influences Reovirus Pathogenesis. Journal of Virology 83: 9630-9640.
28. Dryden KA, Wang GJ, Yeager M, Nibert ML, Coombs KM, et al. (1993) Early Steps in Reovirus Infection Are Associated with Dramatic Changes in Supramolecular Structure and Protein Conformation - Analysis of Virions and Subviral Particles by Cryoelectron Microscopy and Image-Reconstruction. Journal of Cell Biology 122: 1023-1041.
29. Furlong DB, Nibert ML, Fields BN (1988) Sigma-1 Protein of Mammalian Reoviruses Extends from the Surfaces of Viral Particles. Journal of Virology 62: 246-256.
30. Bodkin DK, Nibert ML, Fields BN (1989) Proteolytic Digestion of Reovirus in the Intestinal Lumens of Neonatal Mice. Journal of Virology 63: 4676-4681.
31. Bass DM, Bodkin D, Dambrauskas R, Trier JS, Fields BN, et al. (1990) Intraluminal Proteolytic Activation Plays an Important Role in Replication of Type-1 Reovirus in the Intestines of Neonatal Mice. Journal of Virology 64: 1830-1833.
32. Schulz WL, Haj AK, Schiff LA (2012) Reovirus Uses Multiple Endocytic Pathways for Cell Entry. Journal of Virology 86: 12665-12675.
33. Boulant S, Stanifer M, Kural C, Cureton DK, Massol R, et al. (2013) Similar uptake but different trafficking and escape routes of reovirus virions and infectious subvirion particles imaged in polarized Madin-Darby canine kidney cells. Molecular Biology of the Cell 24: 1196-1207.
34. Luciajandris P, Hooper JW, Fields BN (1993) Reovirus M2 Gene Is Associated with Chromium Release from Mouse L-Cells. Journal of Virology 67: 5339-5345.

35. Hooper JW, Fields BN (1996) Role of the mu 1 protein in reovirus stability and capacity to cause chromium release from host cells. Journal of Virology 70: 459-467.
36. Chandran K, Farsetta DL, Nibert ML (2002) Strategy for nonenveloped virus entry: a hydrophobic conformer of the reovirus membrane penetration protein mu 1 mediates membrane disruption. Journal of Virology 76: 9920-9933.
37. Chandran K, Parker JSL, Ehrlich M, Kirchhausen T, Nibert ML (2003) The delta region of outer-capsid protein mu 1 undergoes conformational change and release from reovirus particles during cell entry. Journal of Virology 77: 13361-13375.
38. Odegard AL, Chandran K, Zhang X, Parker JSL, Baker TS, et al. (2004) Putative autocleavage of outer capsid protein mu 1, allowing release of myristoylated peptide mu 1N during particle uncoating, is critical for cell entry by reovirus. Journal of Virology 78: 8732-8745.
39. McDonald SM, Nelson MI, Turner PE, Patton JT (2016) Reassortment in segmented RNA viruses: mechanisms and outcomes. Nat Rev Microbiol 14: 448-460.
40. Oberhaus SM, Smith RL, Clayton GH, Dermody TS, Tyler KL (1997) Reovirus infection and tissue injury in the mouse central nervous system are associated with apoptosis. Journal of Virology 71: 2100-2106.
41. Garant KA, Shmulevitz M, Pan L, Daigle RM, Ahn DG, et al. (2016) Oncolytic reovirus induces intracellular redistribution of Ras to promote apoptosis and progeny virus release. Oncogene 35: 771-782.
42. Hashiro G, Loh PC, Yau JT (1977) Preferential Cytotoxicity of Reovirus for Certain Transformed-Cell Lines. Archives of Virology 54: 307-315.
43. Duncan MR, Stanish SM, Cox DC (1978) Differential Sensitivity of Normal and Transformed Human Cells to Reovirus Infection. Journal of Virology 28: 444-449.
44. Norman KL, Hirasawa K, Yang AD, Shields MA, Lee PW (2004) Reovirus oncolysis: the Ras/RalGEF/p38 pathway dictates host cell permissiveness to reovirus infection. Proc Natl Acad Sci U S A 101: 11099-11104.
45. Marcato P, Shmulevitz M, Pan D, Stoltz D, Lee PW (2007) Ras transformation mediates reovirus oncolysis by enhancing virus uncoating, particle infectivity, and apoptosis-dependent release. Mol Ther 15: 1522-1530.
46. Twigger K, Roulstone V, Kyula J, Karapanagiotou EM, Syrigos KN, et al. (2012) Reovirus exerts potent oncolytic effects in head and neck cancer cell lines that are independent of signalling in the EGFR pathway. Bmc Cancer 12.
47. Cui HX, Lin Y, Yue LL, Zhao XM, Liu JC (2011) Differential expression of the alpha 2,3-sialic acid residues in breast cancer is associated with metastatic potential. Oncology Reports 25: 1365-1371.
48. Raval G, Biswas S, Rayman P, Biswas K, Sa G, et al. (2007) TNF-alpha induction of GM2 expression on renal cell carcinomas promotes T cell dysfunction. Journal of Immunology 178: 6642-6652.
49. Errington F, White CL, Twigger KR, Rose A, Scott K, et al. (2008) Inflammatory tumour cell killing by oncolytic reovirus for the treatment of melanoma. Gene Therapy 15: 1257-1270.
50. Thirukkumaran CM, Shi ZQ, Luider J, Kopciuk K, Gao H, et al. (2013) Reovirus modulates autophagy during oncolysis of multiple myeloma. Autophagy 9: 413-414.

51. Ikeda Y, Nishimura G, Yanoma S, Kubota A, Furukawa M, et al. (2004) Reovirus oncolysis in human head and neck squamous carcinoma cells. Auris Nasus Larynx 31: 407-412.
52. Boehme KW, Ikizler M, Kobayashi T, Dermody TS (2011) Reverse genetics for mammalian reovirus. Methods 55: 109-113.
53. Weiner HL, Powers ML, Fields BN (1980) Absolute Linkage of Virulence and Central Nervous-System Cell Tropism of Reoviruses to Viral Hemagglutinin. Journal of Infectious Diseases 141: 609-616.
54. Morrison LA, Sidman RL, Fields BN (1991) Direct Spread of Reovirus from the Intestinal Lumen to the Central-Nervous-System through Vagal Autonomic Nerve-Fibers. Proceedings of the National Academy of Sciences of the United States of America 88: 3852-3856.
55. Walters MN, Leak PJ, Joske RA, Stanley NF, Perret DH (1965) Murine Infection with Reovirus. 3. Pathology of Infection with Types 1 and 2. Br J Exp Pathol 46: 200-212.
56. Flamand A, Gagner JP, Morrison LA, Fields BN (1991) Penetration of the Nervous Systems of Suckling Mice by Mammalian Reoviruses. Journal of Virology 65: 123-131.
57. Morin MJ, Warner A, Fields BN (1996) Reovirus infection in rat lungs as a model to study the pathogenesis of viral pneumonia. Journal of Virology 70: 541-548.
58. Kauffman RS, Wolf JL, Finberg R, Trier JS, Fields BN (1983) The Sigma-1 Protein Determines the Extent of Spread of Reovirus from the Gastrointestinal-Tract of Mice. Virology 124: 403-410.
59. Cashdollar LW, Chmelo RA, Wiener JR, Joklik WK (1985) Sequences of the S1 Genes of the 3 Serotypes of Reovirus. Proceedings of the National Academy of Sciences of the United States of America 82: 24-28.
60. Nibert ML, Dermody TS, Fields BN (1990) Structure of the Reovirus Cell-Attachment Protein - a Model for the Domain Organization of Sigma-1. Journal of Virology 64: 2976-2989.
61. Fraser RDB, Furlong DB, Trus BL, Nibert ML, Fields BN, et al. (1990) Molecular-Structure of the Cell-Attachment Protein of Reovirus - Correlation of Computer-Processed Electron-Micrographs with Sequence-Based Predictions. Journal of Virology 64: 2990-3000.
62. Bokiej M, Ogden KM, Ikizler M, Reiter DM, Stehle T, et al. (2012) Optimum Length and Flexibility of Reovirus Attachment Protein sigma 1 Are Required for Efficient Viral Infection. Journal of Virology 86: 10270-10280.
63. Chappell JD, Prota AE, Dermody TS, Stehle T (2002) Crystal structure of reovirus attachment protein sigma1 reveals evolutionary relationship to adenovirus fiber. EMBO J 21: 1-11.
64. Liu HR, Wu LL, Zhou ZH (2011) Model of the Trimeric Fiber and Its Interactions with the Pentameric Penton Base of Human Adenovirus by Cryo-electron Microscopy. Journal of Molecular Biology 406: 764-774.
65. Chen XJS, Stehle T, Harrison SC (1998) Interaction of polyomavirus internal protein VP2 with the major capsid protein VP1 and implications for participation of VP2 in viral entry. Embo Journal 17: 3233-3240.
66. Hendrix RW (1978) Symmetry mismatch and DNA packaging in large bacteriophages. Proc Natl Acad Sci U S A 75: 4779-4783.
67. Stehle T, Dermody TS (2003) Structural evidence for common functions and ancestry of the reovirus and adenovirus attachment proteins. Reviews in Medical Virology 13: 123-132.

68. Lupas AN, Gruber M (2005) The structure of alpha-helical coiled coils. Fibrous Proteins: Coiled-Coils, Collagen and Elastomers 70: 37-+.
69. Strelkov SV, Burkhard P (2002) Analysis of alpha-helical coiled coils with the program TWISTER reveals a structural mechanism for stutter compensation. Journal of Structural Biology 137: 54-64.
70. van Raaij MJ, Mitraki A, Lavigne G, Cusack S (1999) A triple beta-spiral in the adenovirus fibre shaft reveals a new structural motif for a fibrous protein. Nature 401: 935-938.
71. Calvo PG, Fox GC, Parrado XLH, Llamas-Saiz AL, Costas C, et al. (2005) Structure of the carboxy-terminal receptor-binding domain of avian reovirus fibre SigmaC. Journal of Molecular Biology 354: 137-149.
72. Merckel MC, Huiskonen JT, Bamford DH, Goldman A, Tuma R (2005) The structure of the bacteriophage PRD1 spike sheds light on the evolution of viral capsid architecture. Molecular Cell 18: 161-170.
73. Nibert ML, Chappell JD, Dermody TS (1995) Infectious Subvirion Particles of Reovirus Type-3 Dearing Exhibit a Loss in Infectivity and Contain a Cleaved Sigma-1 Protein. Journal of Virology 69: 5057-5067.
74. Chappell JD, Barton ES, Smith TH, Baer GS, Duong DT, et al. (1998) Cleavage susceptibility of reovirus attachment protein sigma 1 during proteolytic disassembly of virions is determined by a sequence polymorphism in the sigma 1 neck. Journal of Virology 72: 8205-8213.
75. Schelling P, Guglielmi KM, Kirchner E, Paetzold B, Dermody TS, et al. (2007) The reovirus sigma 1 aspartic acid sandwich - A trimerization motif poised for conformational change. Journal of Biological Chemistry 282: 11582-11589.
76. Garrido-Urbani S, Bradfield PF, Imhof BA (2014) Tight junction dynamics: the role of junctional adhesion molecules (JAMs). Cell and Tissue Research 355: 701-715.
77. Kostrewa D, Brockhaus M, D'Arcy A, Dale GE, Nelboeck P, et al. (2001) X-ray structure of junctional adhesion molecule: structural basis for homophilic adhesion via a novel dimerization motif. Embo Journal 20: 4391-4398.
78. Prota AE, Campbell JA, Schelling P, Forrest JC, Watson MJ, et al. (2003) Crystal structure of human junctional adhesion molecule 1: Implications for reovirus binding. Proceedings of the National Academy of Sciences of the United States of America 100: 5366-5371.
79. Kirchner E, Guglielmi KM, Strauss HM, Dermody TS, Stehle T (2008) Structure of Reovirus sigma 1 in Complex with Its Receptor Junctional Adhesion Molecule-A. Plos Pathogens 4.
80. Vedula SRK, Lim TS, Kirchner E, Guglielmi KM, Dermody TS, et al. (2008) A comparative molecular force spectroscopy study of homophilic JAM-A interactions and JAM-A interactions with reovirus attachment protein sigma 1. Journal of Molecular Recognition 21: 210-216.
81. Antar AAR, Konopka JL, Campbell JA, Henry RA, Perdigoto AL, et al. (2009) Junctional Adhesion Molecule-A Is Required for Hematogenous Dissemination of Reovirus. Cell Host & Microbe 5: 59-71.
82. Stettner E, Dietrich MH, Reiss K, Dermody TS, Stehle T (2015) Structure of Serotype 1 Reovirus Attachment Protein sigma 1 in Complex with Junctional Adhesion Molecule A Reveals a Conserved Serotype-Independent Binding Epitope. Journal of Virology 89: 6136-6140.
83. Schauer R (2009) Sialic acids as regulators of molecular and cellular interactions. Curr Opin Struct Biol 19: 507-514.

84. Varki A, Schauer R (2009) Sialic Acids. In: Varki A, Cummings RD, Esko JD, Freeze HH, Stanley P et al., editors. Essentials of Glycobiology. 2nd ed. Cold Spring Harbor (NY).
85. Dormitzer PR, Sun ZY, Blixt O, Paulson JC, Wagner G, et al. (2002) Specificity and affinity of sialic acid binding by the rhesus rotavirus VP8* core. J Virol 76: 10512-10517.
86. Chappell JD, Duong JL, Wright BW, Dermody TS (2000) Identification of carbohydrate-binding domains in the attachment proteins of type 1 and type 3 reoviruses. J Virol 74: 8472-8479.
87. Gomatos PJ, Tamm I (1962) Reactive sites of reovirus type 3 and their interaction with receptor substances. Virology 17: 455-461.
88. Frierson JM, Pruijssers AJ, Konopka JL, Reiter DM, Abel TW, et al. (2012) Utilization of Sialylated Glycans as Coreceptors Enhances the Neurovirulence of Serotype 3 Reovirus. Journal of Virology 86: 13164-13173.
89. Weiner HL, Fields BN (1977) Neutralization of Reovirus - Gene Responsible for Neutralization Antigen. Journal of Experimental Medicine 146: 1305-1310.
90. Burstin SJ, Spriggs DR, Fields BN (1982) Evidence for Functional Domains on the Reovirus Type-3 Hemagglutinin. Virology 117: 146-155.
91. Tyler KL, Mann MA, Fields BN, Virgin HW (1993) Protective Anti-Reovirus Monoclonal-Antibodies and Their Effects on Viral Pathogenesis. Journal of Virology 67: 3446-3453.
92. Helander A, Miller CL, Myers KS, Neutra MR, Nibert ML (2004) Protective immunoglobulin A and G antibodies bind to overlapping intersubunit epitopes in the head domain of type 1 reovirus adhesin sigma 1. Journal of Virology 78: 10695-10705.
93. Hutchings AB, Helander A, Silvey KJ, Chandran K, Lucas WT, et al. (2004) Secretory immunoglobulin A antibodies against the sigma 1 outer capsid protein of reovirus type 1 Lang prevent infection of mouse Peyer's patches. Journal of Virology 78: 947-957.
94. Virgin HW, Basselduby R, Fields BN, Tyler KL (1988) Antibody Protects against Lethal Infection with the Neurally Spreading Reovirus Type-3 (Dearing). Journal of Virology 62: 4594-4604.
95. Verdin EM, King GL, Maratosflier E (1989) Characterization of a Common High-Affinity Receptor for Reovirus Serotype-1 and Serotype-3 on Endothelial-Cells. Journal of Virology 63: 1318-1325.
96. Virgin HW, Mann MA, Fields BN, Tyler KL (1991) Monoclonal-Antibodies to Reovirus Reveal Structure-Function-Relationships between Capsid Proteins and Genetics of Susceptibility to Antibody Action. Journal of Virology 65: 6772-6781.
97. Nason EL, Wetzel JD, Mukherjee SK, Barton ES, Prasad BVV, et al. (2001) A monoclonal antibody specific for reovirus outer-capsid protein sigma 3 inhibits sigma 1-mediated hemagglutination by steric hindrance. Journal of Virology 75: 6625-6634.
98. Basselduby R, Spriggs DR, Tyler KL, Fields BN (1986) Identification of Attenuating Mutations on the Reovirus Type-3 S1 Double-Stranded-Rna Segment with a Rapid Sequencing Technique. Journal of Virology 60: 64-67.
99. Diederichs K, Karplus PA (1997) Improved R-factors for diffraction data analysis in macromolecular crystallography. Nature Structural Biology 4: 269-275.
100. Karplus PA, Diederichs K (2012) Linking Crystallographic Model and Data Quality. Science 336: 1030-1033.

101. A.J.C. W (1949) The probability distribution of X-ray intensities Acta Crystallogr D Biol Crystallogr 2: 318-321.
102. Kabsch W (2010) Xds. Acta Crystallographica Section D-Biological Crystallography 66: 125-132.
103. Weichenberger CX, Rupp B (2014) Ten years of probabilistic estimates of biocrystal solvent content: new insights via nonparametric kernel density estimate. Acta Crystallogr D Biol Crystallogr 70: 1579-1588.
104. Brunger AT (1992) Free R value: a novel statistical quantity for assessing the accuracy of crystal structures. Nature 355: 472-475.
105. Vonrhein C, Blanc E, Roversi P, Bricogne G (2007) Automated structure solution with autoSHARP. Methods Mol Biol 364: 215-230.
106. Mccoy AJ, Grosse-Kunstleve RW, Adams PD, Winn MD, Storoni LC, et al. (2007) Phaser crystallographic software. Journal of Applied Crystallography 40: 658-674.
107. Bailey S (1994) The Ccp4 Suite - Programs for Protein Crystallography. Acta Crystallographica Section D-Biological Crystallography 50: 760-763.
108. Murshudov GN, Skubak P, Lebedev AA, Pannu NS, Steiner RA, et al. (2011) REFMAC5 for the refinement of macromolecular crystal structures. Acta Crystallographica Section D-Biological Crystallography 67: 355-367.
109. Smart OS, Womack TO, Flensburg C, Keller P, Paciorek W, et al. (2012) Exploiting structure similarity in refinement: automated NCS and target-structure restraints in BUSTER. Acta Crystallographica Section D-Biological Crystallography 68: 368-380.
110. Adams PD, Grosse-Kunstleve RW, Hung LW, Ioerger TR, McCoy AJ, et al. (2002) PHENIX: building new software for automated crystallographic structure determination. Acta Crystallographica Section D-Biological Crystallography 58: 1948-1954.
111. Strelkov SV, Burkhard P (2002) Analysis of alpha-helical coiled coils with the program TWISTER reveals a structural mechanism for stutter compensation. J Struct Biol 137: 54-64.
112. Vaguine AA, Richelle J, Wodak SJ (1999) SFCHECK: a unified set of procedures for evaluating the quality of macromolecular structure-factor data and their agreement with the atomic model. Acta Crystallographica Section D-Biological Crystallography 55: 191-205.
113. Leone G, Mah DC, Lee PW (1991) The incorporation of reovirus cell attachment protein sigma 1 into virions requires the N-terminal hydrophobic tail and the adjacent heptad repeat region. Virology 182: 346-350.
114. Chandran K, Walker SB, Chen Y, Contreras CM, Schiff LA, et al. (1999) In vitro recoating of reovirus cores with baculovirus-expressed outer-capsid proteins mu1 and sigma3. J Virol 73: 3941-3950.
115. Chandran K, Zhang X, Olson NH, Walker SB, Chappell JD, et al. (2001) Complete in vitro assembly of the reovirus outer capsid produces highly infectious particles suitable for genetic studies of the receptor-binding protein. J Virol 75: 5335-5342.
116. Suchanek M, Radzikowska A, Thiele C (2005) Photo-leucine and photo-methionine allow identification of protein-protein interactions in living cells. Nat Methods 2: 261-267.
117. Vila-Perello M, Pratt MR, Tulin F, Muir TW (2007) Covalent capture of phospho-dependent protein oligomerization by site-specific incorporation of a diazirine photo-cross-linker. J Am Chem Soc 129: 8068-8069.

118. Cao CC, Dong XY, Wu XB, Wen BY, Ji G, et al. (2012) Conserved Fiber-Penton Base Interaction Revealed by Nearly Atomic Resolution Cryo-Electron Microscopy of the Structure of Adenovirus Provides Insight into Receptor Interaction. Journal of Virology 86: 12322-12329.
119. Reddy VS, Natchiar SK, Stewart PL, Nemerow GR (2010) Crystal Structure of Human Adenovirus at 3.5 angstrom Resolution. Science 329: 1071-1075.
120. Mason JM, Arndt KM (2004) Coiled coil domains: Stability, specificity, and biological implications. Chembiochem 5: 170-176.
121. Zhou NE, Kay CM, Hodges RS (1994) The Net Energetic Contribution of Interhelical Electrostatic Attractions to Coiled-Coil Stability. Protein Engineering 7: 1365-1372.
122. Zhou Y, Wu C, Zhao LF, Huang N (2014) Exploring the early stages of the pH-induced conformational change of influenza hemagglutinin. Proteins-Structure Function and Bioinformatics 82: 2412-2428.
123. Suzuki K, Doi T, Imanishi T, Kodama T, Tanaka T (1997) The conformation of the alpha-helical coiled coil domain of macrophage scavenger receptor is pH dependent. Biochemistry 36: 15140-15146.
124. Wada K, Mizuno T, Oku J, Tanaka T (2003) pH-induced conformational change in an alpha-helical coiled-coil is controlled by his residues in the hydrophobic core. Protein and Peptide Letters 10: 27-33.
125. Suzuki K, Yamada T, Tanaka T (1999) Role of the buried glutamate in the alpha-helical coiled coil domain of the macrophage scavenger receptor. Biochemistry 38: 1751-1756.
126. Tanaka T, Mizuno T, Fukui S, Hiroaki H, Oku J, et al. (2004) Two-metal ion, Ni(II) and Cu(II), binding alpha-helical coiled coil peptide. Journal of the American Chemical Society 126: 14023-14028.
127. Conners R, Hill DJ, Borodina E, Agnew C, Daniell SJ, et al. (2008) The Moraxella adhesin UspA1 binds to its human CEACAM1 receptor by a deformable trimeric coiled-coil. Embo Journal 27: 1779-1789.
128. Hartmann MD, Ridderbusch O, Zeth K, Albrecht R, Testa O, et al. (2009) A coiled-coil motif that sequesters ions to the hydrophobic core. Proceedings of the National Academy of Sciences of the United States of America 106: 16950-16955.
129. Herrmann H, Haner M, Brettel M, Ku NO, Aebi U (1999) Characterization of distinct early assembly units of different intermediate filament proteins. Journal of Molecular Biology 286: 1403-1420.
130. Laursen NS, Wilson IA (2013) Broadly neutralizing antibodies against influenza viruses. Antiviral Research 98: 476-483.
131. Tihova M, Dryden KA, Bellamy AR, Greenberg HB, Yeager M (2001) Localization of membrane permeabilization and receptor binding sites on the VP4 hemagglutinin of rotavirus: Implications for cell entry. Journal of Molecular Biology 314: 985-992.
132. Yoder JD, Dormitzer PR (2006) Alternative intermolecular contacts underlie the rotavirus VP5* two- to three-fold rearrangement. Embo Journal 25: 1559-1568.
133. Pesavento JB, Crawford SE, Roberts E, Estes MK, Prasad BVV (2005) pH-induced conformational change of the rotavirus VP4 spike: Implications for cell entry and antibody neutralization. Journal of Virology 79: 8572-8580.
134. Mackow ER, Barnett JW, Chan H, Greenberg HB (1989) The Rhesus Rotavirus Outer Capsid Protein Vp4 Functions as a Hemagglutinin and Is Antigenically

Conserved When Expressed by a Baculovirus Recombinant. Journal of Virology 63: 1661-1668.

8 Acknowledgements

Vielen lieben Dank an…

…Thilo Stehle für die gute Betreuung meiner Promotion, die enorme Freiheit und beständige Förderung eigene Ideen zu entwickeln und zu verfolgen, sowie für die vielen Möglichkeiten mein Projekt auch außerhalb Tübingens voranzutreiben und zu präsentieren.

…Terry Dermody for his enthusiasm and the encouraging and helpful discussions. You have been a great inspiration during the past few years! Thanks also for the great time that I could spend in beautiful Nashville.

...Alex für die riesige Unterstützung bei der Laborarbeit und den Einsatz σ1 zu bändigen.

...the Reovirus team in the US, especially Kristen and Danica. It was so much fun working with you. I really enjoyed meeting and chatting with you and hope that we will stay in touch!

...Kerstin, besonders für die große Hilfe am Anfang meiner Promotion, die Einweisung ins Biacore und die lustige bis „romantische“ Zeit auf diversen Konferenzen.

...Micha für die vielen wertvollen Diskussionen und Ratschläge, die beständig währende Kritik und die vielen Jahre guter Freundschaft.

…Silke Wiesner und Tassula Proikas-Cezanne, die meine Arbeit mit Interesse verfolgt und mich bei meinen TAC-Meetings mit gutem Rat begleitet haben.

...Gregor für den Einsatz im Rahmen des σ1-mAb Projekts.

...Rebebe für das tapfere Durchhalten im 4°C Raum, die beste Schwarzwälder Kirschtorte und die Erweiterung meines Wortschatzes in Bezug auf „Käse“.

...meine Laufkompagnons, Georg und Micbuc, für den Antrieb und die vielen schönen Stunden an der frischen Luft.

…die Girls-Gang für die lustigen Ausflüge und “Frauenabende”.

…die gesamte Arbeitsgruppe, besonders Luisa, Bärbel und Georg für Hilfestellungen und Projektdiskussionen, die gute Atmosphäre und die vielen guten Erinnerungen.

…meine Familie, die mich immer und in jeglicher Hinsicht unterstützt hat.